CHALMERS
UNIVERSITY OF TECHNOLOGY

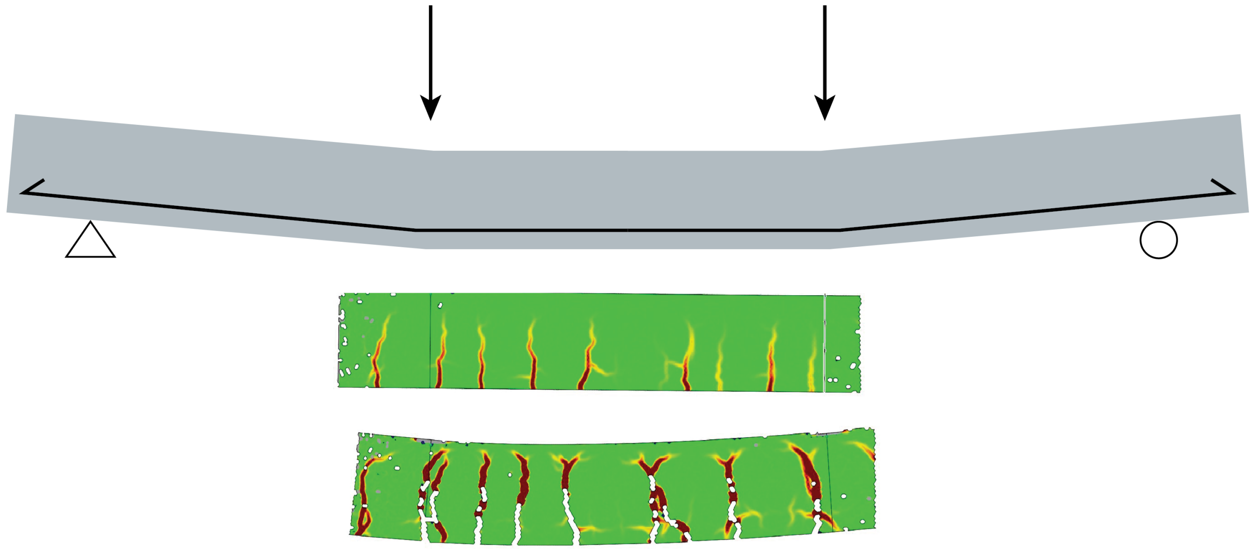

Average reinforcement strain in reinforced concrete structures loaded until failure

An experimental study on the effect of reduced interaction and reinforcement ratio on plastic deformation capacity

Master's thesis in Structural Engineering and Building Technology

ARGHAVAN NOZAD
MOA STEINER

DEPARTMENT OF ARCHITECTURE AND CIVIL ENGINEERING
CHALMERS UNIVERSITY OF TECHNOLOGY
Gothenburg, Sweden 2021
www.chalmers.se

Master's thesis 2021

Average reinforcement strain in reinforced concrete structures loaded until failure

An experimental study on the effect of reduced interaction and reinforcement ratio on plastic deformation capacity

ARGHAVAN NOZAD
MOA STEINER

CHALMERS
UNIVERSITY OF TECHNOLOGY

Department of Architecture and Civil Engineering
Division of Structural Engineering
Concrete Structures
Chalmers University of Technology
Gothenburg, Sweden 2021

Average reinforcement strain in reinforced concrete structures loaded until failure
An experimental study on the effect of reduced interaction and reinforcement ratio on plastic deformation capacity
ARGHAVAN NOZAD, MOA STEINER

Master's Thesis ACEX30
Department of Architecture and Civil Engineering
Division of Structural Engineering
Concrete Structures
Chalmers University of Technology
SE-412 96 Gothenburg
Telephone +46 31 772 1000

Cover: Schematic illustration of a deformed beam subjected to four-point bending and the crack formation and propagation.

Typeset in LaTeX
Gothenburg, Sweden 2021

Average reinforcement strain in reinforced concrete structures loaded until failure
An experimental study on the effect of reduced interaction and reinforcement ratio on plastic deformation capacity
ARGHAVAN NOZAD
MOA STEINER
Department of Architecture and Civil Engineering
Division of Structural Engineering
Conrete structures
Chalmers University of Technology

Abstract

Reinforced concrete and its behavior have a significant role in structural engineering. Reinforced concrete structures are usually designed based on Eurocode for static loading which is not sufficient in case of dynamic loading situations such as explosion. For a structure subjected to impulse loading, plastic deformation capacity is of higher importance rather than the load capacity. The regulations provided by the Swedish Fortification Agency, FKR 2011, provides certain design regulation to fulfill requirements for structures subjected to impulse load. According to these regulations for which a revision is needed, average tensile strain of reinforcement at failure is an effective factor representing plastic deformation capacity.

The aim of this project was to study the effect of reinforcement amount and decreased interaction between steel and concrete on reinforcement average strain and plastic deformation capacity of reinforced concrete beams subjected to static loading. Therefore, nine beams in three different categories were constructed and subjected to a four-point bending test as: three beams with $\phi 10$ reinforcement, three beams with $\phi 12$ reinforcement, and three beams with $\phi 12$ reinforcement with PVC tubes placed in the middle of the reinforcement to decrease the bond. The number of bars and the dimensions were the same for all beams. Before casting, the reinforcement were marked every 50 mm and then remove after testing to measure the elongation of the bars. Also some bars were 3D scanned as another method to measure the elongation and to analyse the cross-sectional changes. During the tests, the structural response of beams was recorded using Digital Image Correlation (DIC).

Although there were some scatter in test results, in general it can be concluded that beams with $\phi 12$ reinforcement provided a larger plastic deformation capacity compared to beams with $\phi 10$ reinforcement. Also, application of PVC tubes to reduce the bond between the concrete and the steel resulted in a larger plastic deformation capacity and average reinforcement strain. The utilization rate for strain values was estimated and the reinforcement bars with PVC tubes showed a increase utilization rate.

Keywords: Reinforced concrete, plastic deformation capacity, average tensile strain, bond interaction, DIC, four-point bending test, FKR.

Medeltöjning i armerade betongkonstruktioner belastade till brott
Försöksstudie på inverkan av reducerad vidhäftning och armeringsmängd med hänsyn till den plastiska deformationsförmågan
ARGHAVAN NOZAD
MOA STEINER
Institutionen för arkitektur och samhällsbyggnadsteknik
Avdelningen för konstruktionsteknik
Betongbyggnad
Chalmers tekniska högskola

Sammanfattning

Armerad betong och dess beteende är av stor betydelse inom konstruktionsteknik. Armerad betongkonstruktioner är vanligen dimensionerade enligt Eurokod för statisk belastning vilket är otillräckligt vid dynamisk belastning såsom explosionslaster. För en konstruktion belastad av en impulslast, är det högre krav på den plastisk deformationsförmågan jämfört med bärförmågan. Fortifikationsverket tillhandahåller föreskrifter, FKR 2011, för att uppfylla de krav som ställs på konstruktioner utsatta för impulslaster. Dessa föreskrifter är i behov av revidering och medeltöjningen av armeringen vid brott är en viktigt egenskap gällnade den plastisk deformationsförmågan.

Syftet med avhandligen var att undersöka vilken effekt armeringsmängden och minskad vidhäftning mellan armeringsstålet och betongen har på medeltöjningen av armeringen och den plastiska deformationsförmågan av armerade betongbalkar vid statisk belastning. Således har nio balkar med tre olika armeringskonfigurationer producerats och fyrpunktsböjningstests: tre balkar med $\phi 10$ armering, tre balkar med $\phi 12$ armering och tre balkar med $\phi 12$ armering där mittdelen av armeringen var belagd med PVC-rör för att minska vidhäftningen. Antalet armeringsstänger och tvärsnittsdimensioner var konstant för alla balkar. Under provning användes digital bildkorrelation (DIC) för att dokumentera och analysera balkens respons. Innan gjutningen av balkarna märktes alla armeringsstänger varje 50 mm för att sedan avlägsnas från betongen efter testning för att mäta förlängningen. Armeringen var också 3D-skannad innan och efter testet som en annan metod för att mäta förlängningen och analysera förändringen av armeringens tvärsnitt.

I allmänhet, balkarna med $\phi 12$ armering resulterade i en större plastisk deformationsförmåga jämfört med balkarna med $\phi 10$ armering. Likaså, användningen av PVC-rör för att reducera vidhäftningen mellan betongen och armeringsstålet resulterade i större plastisk deformationskapacitet och en högre medeltöjning. Armeringens utnyttjadegrad med hänsyn till de uppmätta töjningarna var också beräknad och armeringsstängerna med PVC-rör medförde en ökad utnyttjandegrad.

Nyckelord: Armerad betong, plastisk deformationsförmåga, medeltöjning, vidhäftning, DIC, fyrpunktsböjningstest, FKR.

Contents

Preface

This master's project is an experimental study about the effect of reinforcement ratio and reduced interaction on plastic deformation capacity of reinforced concrete beams subjected to static loading. The specimens were constructed and tested in structural engineering laboratory of Chalmers University of Technology. The project was a cooperation between Chalmers University of Technology and Norconsult AB and financed by the Swedish Fortification Agency as a continuation of an ongoing research to revise the FKR 2011 regulations.

We would like to express our appreciation to Morgan Johansson, our supportive supervisor from Norconsult AB, for providing this great opportunity of having our thesis with Norconsult and helping us obtain a deep knowledge through all stages of our project. In addition, we are very grateful for all supports, guidance, and encouragements from our examiner Joosef Leppänen. Thanks to both Morgan and Joosef we experienced working on an interesting project which was well-planned, instructive and under a stress-free situation. We appreciate the great assistance and patience of Anders Karlsson with laboratory operation. Also, we are thankful to Mathias Flansbjer, RISE, for the provided information and help with DIC procedure.

Arghavan Nozad, Moa Steiner, Gothenburg, June 2021

Nomenclature

Greek letters

χ Curvature
χ_{pl} Plastic curvature
χ_u Curvature at ultimate state
χ_y Curvature at yielding state
Δr Length of which a local bond failure occurs in the concrete
λ Shear slenderness
$\omega_{s,crit}$ Critical mechanical ratio of tensile reinforcement
ω_s Mechanical ratio of reinforcement in tension
$\omega_s^{'}$ Mechanical ratio of reinforcement in compression
ω_v Mechanical ratio of stirrups
ρ_s Reinforcement ratio parameter
τ_b Bond stress
$\theta_{pl,EC}$ Plastic rotational capacity based on Definition in Eurocode 2
θ_{pl} Plastic rotational capacity based on Definition in BK 25 Method
ε_{c1u} Concrete strain limit at maximum load
ε_{cc} Concrete compressive strain
ε_{cm} Concrete mean strain
ε_{ct} Concrete tensile strain
ε_{cu} Concrete ultimate strain
ε_{cy} Concrete strain at reinforcement yielding
ε_{su} Reinforcement ultimate strain
ε_{su}^* Reinforcement ultimate strain with simplified consideration of tension stiffening
ε_{sy} Reinforcement strain at yielding
ε_s Reinforcement average strain over the equivalent plastic length
ε_{uk} Reinforcement ultimate strain at maximum load

Roman lowercase letters

a Distance between support and concentrated load
b Width of beam cross section
d Effective depth
f_{cc} Concrete compressive strength
f_{ck} Characteristic concrete compressive strength
f_{cm} Mean concrete compressive strength
$f_{ctk0,05}$ Lower characteristic tensile strength of concrete
$f_{ctk0,95}$ Upper characteristic tensile strength of concrete
f_{ct} Concrete tensile strength
f_c Compressive cylinder strength of concrete
f_{tk} Characteristic tensile strength of reinforcement
f_{tk} Tensile strength of reinforcement
f_u Ultimate strength of reinforcement
f_{yk} Characteristic yield strength of reinforcement

f_y Yield strength of reinforcement
h Height of beam cross section
k Correction factor for plastic rotation
l Total length of beam
l_0 Length between zero moment and plastic hinge
l_1 The ratio of bending moment to shear force at support
l_p Equivalent plastic hinge length
$l_{t,max}$ Maximum transmission length
l_t Transmission length
l_y Length of yielding region
q Uniformly distributed load
r Radius of curvature
s Distance of stirrups
$s_{r,max}$ Maximum crack spacing
$s_{r,min}$ Minimum crack spacing
s_r Crack spacing
u Displacement
u_{el} Elastic deformation
u_{pl} Plastic deformation
u_{tot} Total deformation
u_u Ultimate deformation
x Distance to neutral axis from top edge (compressive block height)
x_u Compressive block height at failure state
x_y Compressive block height at yielding state
z Distance from gravity center

Roman uppercase letters
A_s Area of reinforcement in tension
$A_s^{'}$ Area of reinforcement in compression
A_v Area of reinforcement in shear
E Modulus of elasticity
E_{cm} Mean modulus of elasticity
E_s Modulus of elasticity of steel
F External force
F_{max} Maximum load
I Moment of inertia
M_{sup} Bending moment at support
M_u Ultimate moment
M_y Yielding moment
R Internal resistance force
V_{sup} Shear force at support
W_i Internal work

1 Introduction

1.1 Background

Reinforced concrete is a commonly used material for structural elements. Normally, concrete structures are designed to withstand static loading and the design regulations are made based on that fact. However, there are structures that can be subjected to other types of loading. One example of this structure is protective shelters which have to be designed not only to withstand static load but also e.g. explosion loads. To be effective, the protective structures have high demand on its plastic deformation capacity rather than large load capacity. Further, the response of a structure subjected to impulse loading may have a different response compared to structures subjected to only static loading. This means that a structure designed to withstand static loading is not always as suitable to withstand the effect of an explosion load.

Since protective structures have different demands compared to regular structures, the design regulations from the Eurocodes are not sufficient. Therefore, a structure subjected to impulse loading has to be designed according to certain design regulations, e.g. FKR 2011 (Swedish Fortification Agency, 2011). Mentioned above, the plastic deformation capacity of impulse loaded structures is crucial and, according to FKR 2011, an important parameter to determine this capacity is the average reinforcement tensile strain at failure. This parameter depends on the reinforcement configuration, mechanical properties of the materials and the interaction between reinforcement and concrete. The current regulations are in need of update and the average tensile strain is one parameter that needs to be revised.

1.2 Aim

The aim of this thesis is to provide a better understanding of structural behavior of reinforced concrete structures loaded until failure with focus on reduced bond between the reinforcing steel and the concrete and the average reinforcement strain. This behavior is considered after yielding of reinforcement and at its rupture in order to study the average reinforcement strain and plastic deformation capacity under static loading.

The above mentioned data are needed as an update of input data for Design regulations from Swedish Fortification Agency, used for impulse loaded structures – FKR 2011. The results from this project helps to calculate the average tensile reinforcement strain based on material properties, reinforcement configuration and geometry. It is important to consider that a structure exposed to static loading may have a different response compared with being exposed to an impulse load. Therefore, plastic deformation capacity has a higher importance than load capacity in the latter type of load case.

1.3 Methodology

The methodology was based on both literature survey and experimental testing. This work was a continuation of Köseoğlu (2020), in which reinforced concrete prisms loaded by a uniaxial tensile load until failure were studied. However, in the current project, beams were examined under four-point bending tests until failure with focus on the region between the point loads with constant moment.

The reinforcement bars were marked and went through 3D scanning before casting and after tests for plastic strain measurements. Plastic tubes were used in some of the test specimens to reduce the bond between steel and concrete. After casting and during the four-point bending test the cracks and deformation developments were monitored by a camera and digital image correlation (DIC) was used to to measure deformations and calculate strain fields in the concrete. After testing, the reinforcement was removed from the concrete in order to measure the elongation and calculate the strain. The expected outputs were load-displacement relation, crack pattern and plastic strain distribution in the reinforcement bars.

1.4 Limitations

The concrete material properties, specimen size and the number of bars were the same for all specimen. The beams were limited to three types with difference either in bar diameter or in bond interaction:

1. $2\phi10$ (without plastic tubes)
2. $2\phi12$ (without plastic tubes)
3. $2\phi12$ (with plastic tubes)

For this test series, three numbers of each beam type was studied. So the total number of specimen was limited to nine beams. Plastic deformation along the bars was determined in all beam specimens but only three beams (six bars) were further studied using 3D scanning. Also, the analysis was limited to static loading with two point loads.

2 Material behaviour

2.1 Introduction

In order to understand the structural behaviour and theoretical background of reinforced concrete beams, basic knowledge about the structural properties of plain concrete and reinforcing steel and their behaviour under loading is necessary. The combination of the two materials makes it possible to utilize the compressive strength of concrete and the tensile strength of reinforcement to form a high strength structure (Engström, 2014). One important parameter in the reinforced concrete structures is the bond between materials which has an influence on the transfer of stresses and the structural behaviour as crack development, crack spacing and crack width.

2.2 Concrete

The mechanical behaviour of plain concrete is characterized by the difference in tensile and compression strength where the tensile capacity is significantly lower compared to the compressive capacity as indicated in the stress-strain relationship curve in Figure 2.1 (Al-Emrani et al., 2013).

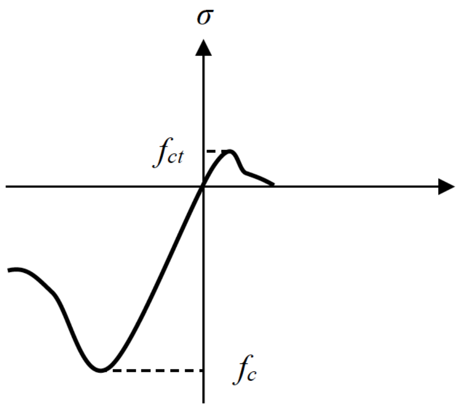

Figure 2.1 Stress-strain relationship for plain concrete under uniaxial loading where f_{ct} corresponds to the tensile strength and f_c the compression strength (Jönsson & Stenseke, 2018).

From Figure 2.1, it can be observed by the steep slope at failure, that concrete is a brittle material when it fails in tension. The failure in compression is partially brittle but the behaviour depends on the concrete strength and the loading rate (Al-Emrani et al., 2013). Concrete with lower strength classes present a larger strain at failure and are therefore more ductile compare with higher strength classes which have a more brittle failure.

The mechanical properties like tensile strength, deformation capacity and modulus of elasticity are associated with uncertainties (Engström, 2014). Because of natural scatter in the material, specimens made of the same concrete which are handle under identical conditions give various results. Therefore, a frequency distribution can be used to present results like mean values, standard variations and fractile values. An example of a typical frequency distribution for the tensile strength of plain concrete is presented in Figure 2.2.

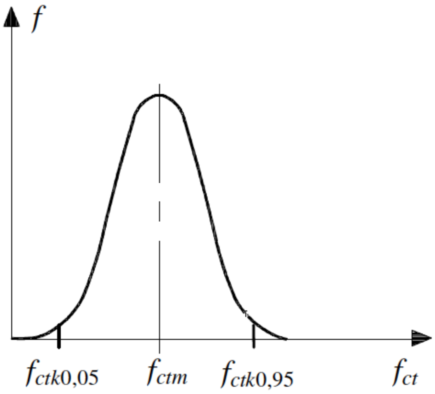

Figure 2.2 *Frequency distribution of the tensile strength with mean value f_{ctm}, low and high characteristic value, $f_{ctk0,05}$ and $f_{ctk0,95}$ (Engström, 2014).*

The low and high characteristic values, also called the fractile values, are defined by the 5%-fractile and the 95%-fractile. The low fractile implies that 95% of all test exceeds this value and for the high fractile, only 5% of the tests exceeds.

2.2.1 Compressive strength

The classification of concrete is done based on the compressive strength from standardised strength classes. The concrete compressive strength is influenced by different factor like size and shape of the specimen, curing, storage, handling and test procedure. Therefore, a standardised procedure of the compressive test is stated in the European Standard and according to Eurocode 2, the compressive strength is defined as the strength determined at an age of 28 days.

The compressive strength is determined by applying an uniaxial force to a cylindrical specimen with height 300 mm and diameter 150 mm (CEN, 2019). However, in Sweden it is more common to determine the compressive strength of concrete with cubes with a size of 150 mm. As mentioned above, the result of a compressive test is depended on the testing method and therefore a cylindrical test and a cubic test will give different concrete strengths. According to Engström (2014) the test with a cubic specimens gives a mean strength approximately 1.2 time greater compared to test preformed on cylindrical specimen. The difference in results are due to the fact that a cube will have a more favourable stress state, due to confinement effects, compared with a cylinder.

The relation between a cylinder's and a cube's compressive strength can be expressed as

$$f_{cm} \approx \frac{f_{cm,cube}}{1.2} \tag{2.1}$$

where f_{cm} is the mean strength of the compressive strength of concrete from a cylindrical specimen and $f_{cm,cube}$ from a cubic specimen.

2.2.2 Tensile strength

The tensile strength of concrete can be determined by pure tensile tests, flexure or splitting tests and the method used will influence the result. The tensile strength increases with increasing compressive strength and according to Eurocode 2 (CEN, 2004), the tensile strength can be determined by known measured values of the characteristic compressive strength. The mean tensile strength after 28 day and the low and high fractile values can be estimated by the following relationships.

For strength classes $\leq$ C50/60

$$f_{ctm} = 0.3(f_{ck})^{2/3} \tag{2.2}$$

For strength classes $>$ C50/60

$$f_{ctm} = 2.12 \ln\left(1 + \frac{f_{ck} + 8}{10}\right) \tag{2.3}$$

$$f_{ctk0.05} = 0.70 f_{ctm} \tag{2.4}$$

$$f_{ctk0.95} = 1.3 f_{ctm} \tag{2.5}$$

Where f_{ck} is the characteristic compressive strength in [MPa].

2.2.3 Modulus of elasticity

A concrete specimen subjected to uniaxial compression, the non-linear stress-strain relationship is shown in Figure 2.3. From the stress-strain curve, it can be observed that the modulus of elasticity changes with the stress level, with higher stresses the modulus of elasticity decreases. According to Eurocode 2 (CEN, 2004) the mean modulus of elasticity E_{cm} can be calculated as the secant modulus between $\sigma_s = 0$ and $\sigma_s = 0.4 f_{cm}$.

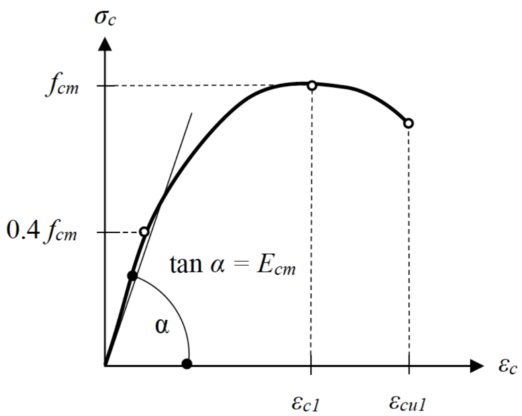

Figure 2.3 Idealised stress-strain relationship for concrete under compression to determine the mean value of the modulus of elasticity, E_{cm} by 40% of the mean compressive strength, f_{cm} (CEN, 2004).

The mean value of the modulus of elasticity can also be calculated as a relationship to the concrete's mean compressive strength

$$E_{cm} = 22 \left(\frac{f_{cm}}{10} \right)^{0.3} \tag{2.6}$$

2.3 Reinforcing steel

In contrast to concrete, the reinforcing steel has high tensile strength and a more ductile behaviour. The classification of reinforcement is based on a large number of properties like for instance, strength, fatigue strength, ductility class, size etc.

The structural response of the steel reinforcement can be examined by applying an uniaxial tensile load to a reinforcement bar. The applied force and the elongation of the specimen are measured and the steel stress can be calculated by dividing the applied load by the cross-sectional area (Al-Emrani et al., 2013). This results is a typical stress-strain relationship as is shown in Figure 2.4.

The stress-strain curve is characterised by four different stages: the elastic domain, the yielding plateau, stain hardening up to maximum tensile stress and finally, necking and rupture of the reinforcement. In the early stages of loading, during low strains the behaviour of the reinforcement is characterised by elasticity with elastic deformations. As the load increases, the strain increases and when the stress reaches a point where the deformations in the material cannot longer be considered as elastic. This point is called the yielding point and the level of stress is equal to the yielding stress f_y and the corresponding yielding strain ε_y.

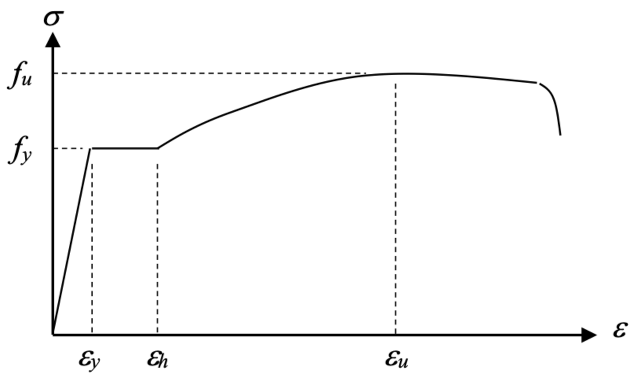

Figure 2.4 Schematic stress-strain relationship for hot-rolled reinforcing steel, modified from (Johansson & Laine, 2012).

As the yielding is reached, a plateau with constant stress and increasing strain can be distinguished in the stress-strain curve. Past the yielding plateau, the elastic behaviour has progressed to a plastic behaviour with permanent deformations in the material. When the stress reaches the ultimate strength f_u and the strain at maximum stress ε_u, further increases of stress will induce dislocations in the material and the steel bar begins to reach failure. The ratio between the ultimate strength and the yielding strength is defined as

$$\eta = f_u/f_y \tag{2.7}$$

and it is called hardening ratio which is an important parameter that influences the material's ductility.

2.3.1 Strain hardening

After yielding, the material response and the mechanical behaviour of the steel reinforcement is altered. Dislocations or so called, point of defects are forming in the lattice structure of the steel material (Al-Emrani et al., 2013). As the load increases, the amount of dislocations increase and the steel begins to harden and strengthen which means that a greater amount of force is required for further deformations. The strain hardening can be distinguished in the stress-strain curve after the yielding plateau and the it starts at the strain ε_h.

2.3.2 Necking

At the maximum load, where the strain is equal to ε_u and stress f_u, the stress-strain curve indicates a plateau and a decrease of the steel stress. The decrease can be explained by locally accumulation of dislocations which is called necking. The necking can be distinguished as a decrease in the cross-sectional area of the specimens, see Figure B.7 in Appendix B. In the necking area, the local deformations and reduced cross-sectional area under constant applied load will induce a local stress increase according to the following equation:

$$\sigma = \frac{F}{A} \tag{2.8}$$

where σ is the internal steel stress, F is applied tensile force and A is the cross-sectional area. When the necking is induced, the maximum capacity of the reinforcement bar and the failure load are reached. As a consequence of the reduced cross-sectional area, less load is required to deform the steel reinforcement further and necking is therefore an indication of near-failure.

2.3.3 Design simplifications

According to Eurocode 2 (CEN, 2004), a simplification of the stress-strain relation with a inclined top branch as shown in Figure 2.5 can be assumed in the design. The simplification disregards the yielding plateau and effects of necking. The ultimate capacity defined in Eurocode 2 corresponds to the maximum stress f_u and the strain ε_u from Figure 2.4, thus the necking and the remaining capacity after necking occurs is disregarded in the simplification. However, Eurocode 2 also allows for an even more simplified relationship of the stress-strain curve with horizontal top branch and maximum stress f_y which disregard the hardening.

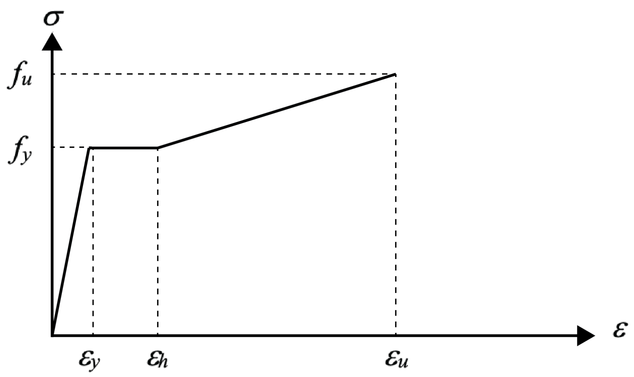

Figure 2.5 Simplified relationship of the stress-strain curve with a inclined top branch for reinforcing steel where the ultimate strain corresponds to the strain at maximum stress ε_u from Figure 2.4.

The modulus of elasticity E_s is defined as the slope of the linear elastic part of the stress-strain curve and calculated as the secant between the origin and the yielding point.

2.4 Reinforced concrete

When the plain concrete and the reinforcing steel are combined together it forms a composite material with high compressive strength from the concrete and an increased ductile behaviour and tensile strength from the reinforcement. The structural response and change of behaviour with respect to the bond between the materials are important knowledge for understanding the reinforced concrete's behaviour and the formation of cracks.

2.4.1 Structural response

Reinforced concrete as a combination of concrete and steel has a complex structural behavior. This combination is due to compensate low tensile strength of concrete and utilize its high compressive capacity. There are three simplified models, shown in Figure 2.6, to explain the structural behavior of the composite material: linear elastic, plastic and elastic-plastic response (Johansson & Laine, 2012).

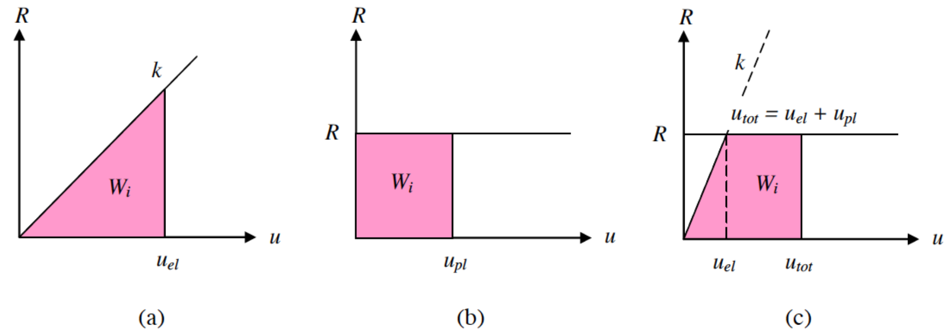

Figure 2.6 *Structural response and internal work W_i, assuming (a) linear elastic response, (b) plastic response and (c) elastic-plastic response (Johansson & Laine, 2012).*

In the elastic model there is a linear stress-strain relation and the deformations are not permanent which implies that the material returns to its original state in case of unloading. For the plastic model the deformation is zero for stresses under yield stress. Reaching the yield stress, deformation starts which is permanent and the material can not return to its original state in case of unloading. The elastic-plastic model is combination of linear elastic and ideal plastic responses. Before reaching the yield stress the material has a linear elastic behavior and deformations are reversible. Also, the material can not take more stress after the yielding stress is reached so permanent deformations take place.

2.4.2 Stages during loading

Concrete's poor performance in tension will induce cracks where the tensile stresses exceeds the concrete tensile strength. In reinforced concrete, cracks is assumed in the design in tensioned regions and reinforcing steel is used in order to distribute cracks and limit crack widths (Al-Emrani et al., 2011). For uncracked concrete it can be assumed that there is full interaction between the concrete and reinforcement which means that the steel strain increases with the same amount as the concrete strain. In order to get an effect of the reinforcement's good performance in tension, the concrete must crack so the steel strain can increase. Therefore, the structural response of reinforced concrete is highly dependent on if the section is uncracked or cracked. Before cracks are initiated, the reinforced concrete has a linear response which means that the strain increases linearly with the applied load and the reinforcement steel is generally assumed to have a small influence of the stiffness.

When the section cracks, there will be a change in behaviour since the force that was resisted by the tensile stresses in the concrete is suddenly carried by the reinforcement. Consider a simply supported beam with one span, subjected to a uniformly distributed load, q as shown in Figure 2.7. The structural behaviour of the beam can be divided into three different stages: state I, state II and state III. As the load increases, the deflection and structural response change, and those changes can be described with the load-displacement curve. The load-displacement curve illustrating the three different stages together with the elastic-plastic response with bi-linear relation, described in Figure 2.6 (blue curve).

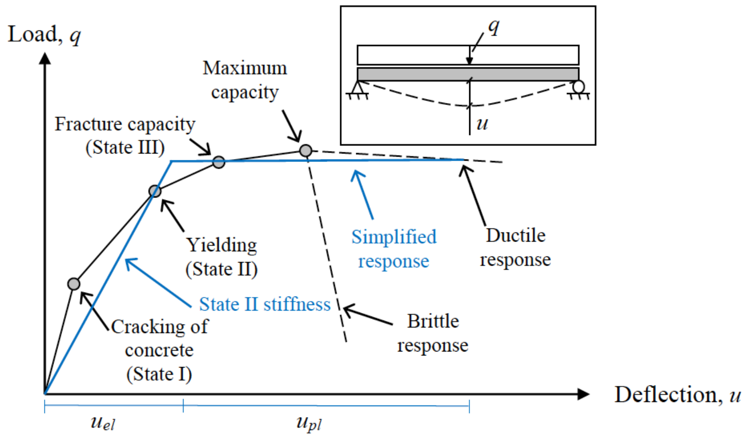

Figure 2.7 *The structural response of reinforced concrete beam with a uniformly distributed load. The blue curve represent a simplified bi-linear response of the structural behaviour. From (Jönsson & Stenseke, 2018), inspired by (Johansson & Laine, 2012).*

State I: At this state the strain is equal in concrete and reinforcement, the concrete is uncracked and linear elastic material response is assumed. The influence of reinforcement can be ignored as it has a small contribution to the stiffness.

State II: By increasing the load, tensile stress reaches concrete's tensile capacity, cracking takes place and stiffness decreases considerably. Linear elastic response is considered for both steel and concrete but influence of concrete in the tensile zone is neglected.

State III: After reinforcements start yielding, the non-linear material response is used for both steel and concrete and by load increment there will be failure either in form of concrete crushing or steel rupture.

Tension siffening

When a section cracks, the concrete does not take any stress in the tensile zone and all tensile stress is transferred into reinforcement. As a result the stiffness undergoes a significant drop at the cracked section and the stiffness can only account for reinforcement. However, in the global response of the beam, concrete between cracked sections contributes to total stiffness of the beam due to the bond between steel and concrete and this phenomena is called tension stiffening, see Figure 2.8. This effect decreases by load increment and consequently by increasing the number of cracks.

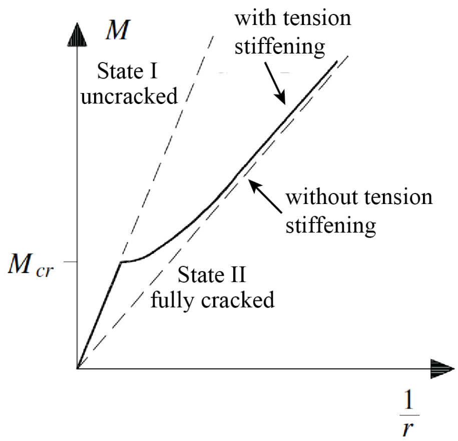

Figure 2.8 Sectional response with regard to tension stiffening in a concrete member subjected to pure bending. Based on linear stress-strain relationship for both concrete and steel, inspired by (Engström, 2015).

The effect of tension stiffening can be seen at the end of the prism in Figure 2.10 or next to a crack in Figure 2.12. The concrete tensile stress at the ends or next to the cracks gradually increases and becomes most active in the middle of the prism or between the cracks. Later, when the reinforcement starts to yield, the bond between the materials decrease and consequently, the stress in the concrete also decrease.

The effect of tension stiffening in the initial cracking stage was clearly seen in tests made by Köseoğlu (2020). A concrete prisms with one centralized reinforcement bar were loaded by a uniaxial tensile load until failure. The resulting force-strain curves for three prism with $\phi16$ reinforcement bars and the force-strain curve of a plain $\phi16$ bar are presented in Figure 2.9. At the initial stage, the prisms were stiffer compared to the plain bar due to the tension stiffening effects where the concrete contributes to the stiffness of the prisms. Towards the end of the loading, more cracks forms, the crack width increase and less concrete contributes to the global stiffness. The curves from the prisms are closer to the curve of the plain bar which indicates that the effect of tension stiffening decreases and the reinforcement bar mainly contributes to the global response of the prism.

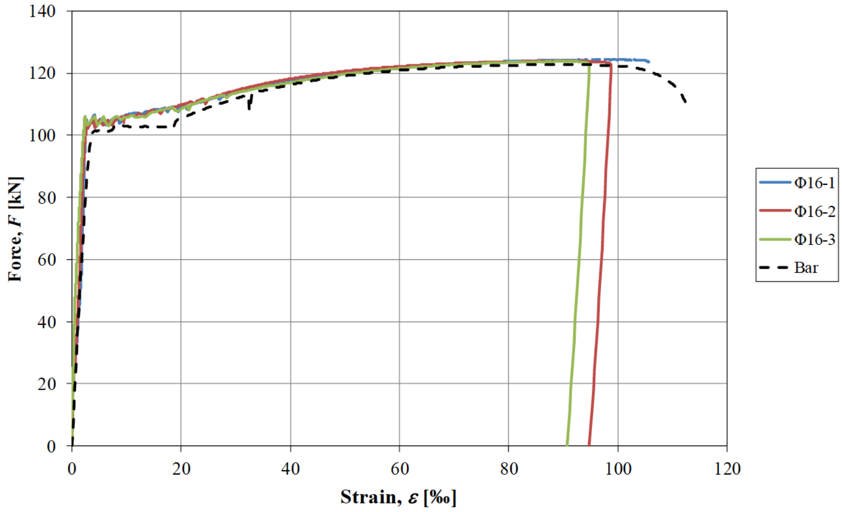

Figure 2.9 Force-displacement curve for concrete prisms subjected to uniaxial tension test (Köseoğlu, 2020).

As the number and width of cracks increase along the beam, the stiffness depends on reinforcement. Larger amount of load will result in yielding of reinforcement which starts at the section with largest stress. At this section the reinforcement experiences more deformation than adjacent sections in which the reinforcing steel has elastic response. A region with concentrated plastic rotation is called plastic hinge (Johansson & Laine, 2012).

2.4.3 Crack development

A more detailed theory behind the cracking process can be explained by studying the behaviour of a concrete prism with centric reinforcement subjected to a uniaxial tensile load. At each end, the projecting reinforcement bar is loaded by a horizontal tensile force that is less than the cracking load of the concrete, the resulting stress distribution of such loaded prism is illustrated in Figure 2.10.

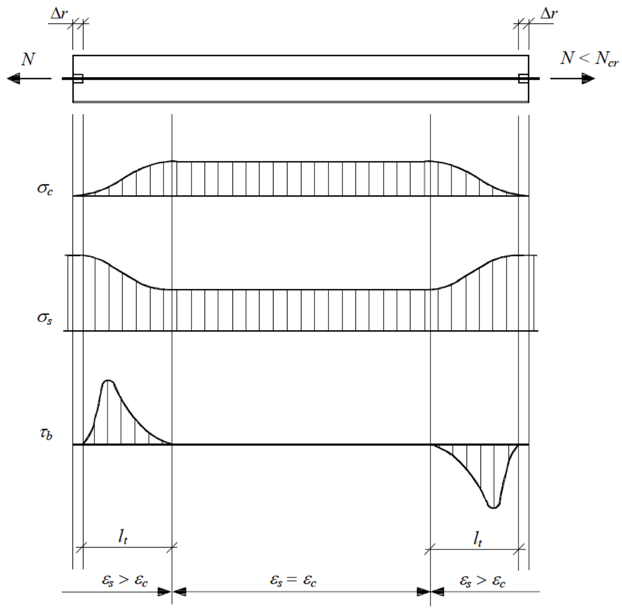

Figure 2.10 Stress distribution of a reinforced concrete member loaded in tension with a tensile force less than the cracking force (Engström, 2014).

As the reinforcement bar is loaded, the bond between the reinforcement and the concrete is preventing the bar from slipping in relation to the concrete. The bond is transferring the force from the reinforcement to the surrounding concrete which leads to a decrease of stress in the reinforcement while the stress in the concrete increases. The load transfer causes bond stresses called τ_b and the transfer takes place within a distance called transmission length, l_t. The bond stress varies along the transmission length and the mean value of the bond stress τ_{bm} can be evaluated as

$$\tau_{bm} = \frac{\int_0^{l_t} \tau_b(x)dx}{l_t} \tag{2.9}$$

The stress transfer between the reinforcing steel and the surrounding concrete is dependent on the surface properties of the reinforcement and the tensile strength of the concrete. From empirical studies, considering k_1 as a factor depending on the surface of the reinforcement, it has been shown that the mean bond stress can be estimated as

$$\tau_{bm} = \frac{3}{2 \cdot k_1} \cdot f_{ct} \tag{2.10}$$

The transmission is initiated at the ends of the specimen and continues towards the mid-section until the stress in the steel and concrete is equal and no further transmission occurs. When the stresses are equal, there is compatibility between the deformation in the materials. However, this is not the case for the material within the transmission length since the strain in the steel is higher compared to the strain in the concrete and a local slip of the bar occurs when the bar elongates more than the concrete.

At the ends of the prism, the load is causing a local bond failure of the concrete's free edge which has a length Δr, see Figure 2.11. The failure results in a zone where no bond stress can be transferred from the reinforcement to the concrete and therefore the stress in the bar is constant. According to Engström (2014), the local cone failure can be approximated as two times the reinforcement bar's diameter:

$$\Delta r \approx 2\phi \tag{2.11}$$

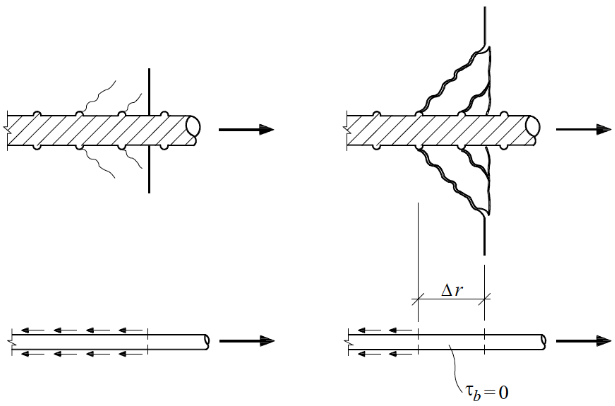

Figure 2.11 Principle of local cone failure of the concrete near to the loaded end (Engström, 2014).

2.4.4 Crack formation

As the load increases, the transmission length and the stress in the materials increase. The increase continues until the tensile stress exceeds the tensile strength of the concrete and a crack appears. The crack affects the bond between the materials since no stresses can be transferred from the reinforcement to the concrete in the cracked section.

Since the tensile stress in the concrete is higher in the mid-region compared to within the transmission length, the crack can be initiated anywhere in the mid-region of the specimen. When the first crack appears, the transmission length has reached its maximum length, $l_{t,max}$. No further increase of the transmission length can occur since that requires an increase of the tensile stress, which in turn, is not possible since no additional tensile force can be applied without further cracking. In theory, when the tensile strength of the concrete is exceeded more cracks can appear without an increase of the load. However, in practice a small increase of load is needed since there is a slightly variation of tensile strength between sections due to normal distributed scatter, illustrated in Figure 2.2.

The cracking process can be described as shown in Figure 2.12 and after the first crack appears, the concrete prism is divided into two parts which acts as two different tensile members with the reinforcement loaded in their ends. The two members behave similar to the originally uncracked concrete prisms described above. On each side of the crack, the reinforcement tends to slip in relation to the concrete which results in a development of a new transmission zone where the stress is transferred from the loaded bar to the concrete. The distance between the two cracks cannot be less than $2 \cdot l_{t,max}$ since the tensile stress within this distance cannot exceed the concrete tensile strength and a new crack can not appear. On the other hand, if the distance is more than $2 \cdot l_{t,max}$ the tensile stress can be build up again until the concrete tensile strength is reached and a new crack can be initiated. The cracking process will continue until the spacing between all cracks are smaller than $2 \cdot l_{t,max}$ and at that point, no further cracks can appear, and the crack formation is finalised. This is called stabilized cracking stage. In theory, if the load increases, no further cracks can occur but the steel stress is still increasing which results in an increased crack width. Observations from Köseoğlu (2020) showed that further cracking appeared at much later stages when the reinforcement was yielding. However, the initial cracking prior to yielding was dominating the final crack pattern.

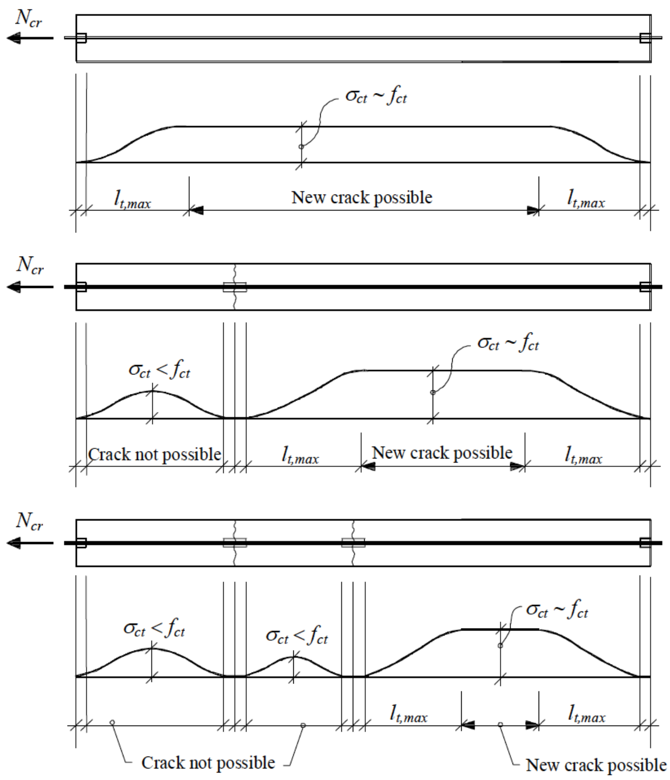

Figure 2.12 Concrete stress distribution during the cracking process in a reinforced concrete member subjected to a tensile force higher than the cracking load (Engström, 2014).

Bond-slip relation

As mentioned above, within the transmission length the steel stress is larger than the concrete stress which cause elongation of the bar and a slip in relation to the concrete. The bond stress has the maximum value at a cracked section and deceases towards the opposite end of the transmission length. However, according to Lundgren (1999), the transfer of bond stresses is highly effected when the reinforcement bar yields. Due to the so called Poisson effect, the cross-sectional area of the reinforcement decreases at yielding which reduces the stress transfer between the reinforcement and concrete.

The relation between the bond stress and the slip has been studied experimentally in pull-out tests and as a result a schematic relationship curve is presented in Figure 2.13 where the slip is the relative difference in displacement between the reinforcement bar and the concrete. The upper curve displays the bond-slip relation at pull-out and the dashed curve shows loss of bond due to yielding of the reinforcement.

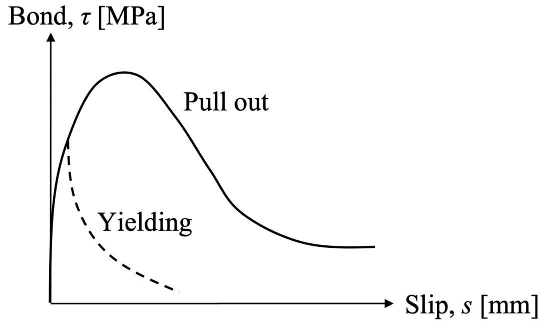

Figure 2.13 A schematic relationship between the bond stress and local slip from pull-out tests and yielding of reinforcement. Figure inspired by (Plos et al., 2021).

Crack spacing and crack width

The bond failure of the concrete near the ends of each cracked member is resulting in zero transferred stress between the steel and concrete. As a consequence, the length it takes to reach equilibrium between the concrete stress and the steel stress is equal to the sum of the transmission length and the length of the concrete cone failure, $l_{t,max} + \Delta r$. Therefore, the minimum crack distance $s_{r,min}$, is equal to the distance between the loaded end and the crack and cannot be less than $l_{t,max} + \Delta r$, indicated to the left hand side in Figure 2.14. The maximum crack distance $s_{r,max}$, is the distance between two cracks and cannot be more than $2(l_{t,max} + \Delta r)$ as shown to the right in Figure 2.14. Thus, the crack spacing must fulfil the following condition

$$l_{t,max} + \Delta r \leq s_r \leq 2 \cdot l_{t,max} + 2\Delta r \tag{2.12}$$

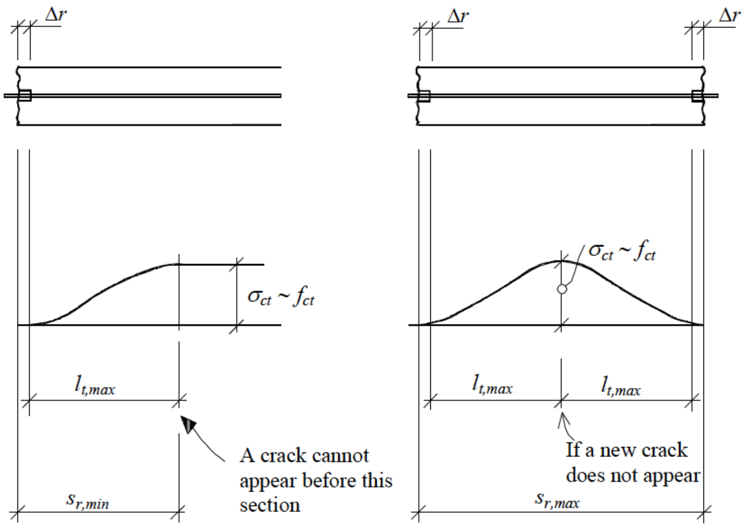

Figure 2.14 The minimum and maximum of the crack spacing after fully developed crack formation (Engström, 2014).

With known bar diameter, concrete tensile strength and average bond stress the minimum and maximum crack spacing can be calculated using Equations (2.13) and (2.14) respectively.

$$s_{r,min} = \Delta r + \frac{1}{4} \cdot \frac{f_{ct}}{\tau_{bm}} \cdot \frac{\phi}{\rho} \tag{2.13}$$

$$s_{r,max} = 2\Delta r + \frac{1}{2} \cdot \frac{f_{ct}}{\tau_{bm}} \cdot \frac{\phi}{\rho} \tag{2.14}$$

where ρ is the reinforcement amount described as the ratio between the steel area, A_s and concrete cross-sectional area, A_c.

$$\rho = \frac{A_s}{A_c} \tag{2.15}$$

In Eurocode 2 (CEN, 2004), the concrete area is determined as the effective concrete area in tension that surrounds the reinforcement, $A_{c,eff}$. The height of the concrete zone in tension $h_{c,eff}$ can be defined as

$$h_{c,eff} = min \begin{cases} 2.5(h-d) \\ (h-x)/3 \\ h/2 \end{cases} \tag{2.16}$$

where h is the height of the cross section, d is the distance from the top of the cross section to the center of gravity of the reinforcement layer and x is height of the compressive zone.

According to Eurocode 2 (CEN, 2004), the characteristic crack width can be calculated by using the maximum crack spacing, $s_{r,max}$ multiplied with the mean strain difference between the steel and concrete.

$$w_k = s_{r,max}(\varepsilon_{sm} - \varepsilon_{cm}) \tag{2.17}$$

The characteristic crack width equation from Eurocode 2 is an approximation by assuming perfect bond between the steel and concrete; i.e. no slip. However, a more correct approach to determine the crack width is obtained by integrating the difference between the steel strain ε_{sx} and the concrete strain ε_{cx} over the crack spacing s_r (Tammo, 2009).

$$w = \int_{s_r} (\varepsilon_{sx} - \varepsilon_{cx})dx \tag{2.18}$$

Factors influencing the crack width

An important parameter that effect's the crack width is the steel stress and the corresponding steel strain (Tammo, 2009). A weak bond between the materials results in larger crack spacing since less stresses are transfer from the reinforcement bar to the surrounding concrete. The stress development is also effected by the cross-sectional area of the steel bar. A larger reinforcement amount gives a decrease of the steel stress and therefore a decrease in steel strain and as a result a smaller strain difference between the steel and concrete, see Equation (2.17).

The configuration of the reinforcement bars is also affecting the crack width. The bar diameter is important since the contact area between the steel and concrete influence the transmission of bond stresses. The local slip of the bar on each side of the crack affects the crack width. Therefore, a small bar diameter and small spacing will increase the bond between the materials and reduce crack width, given that the reinforcement area is constant.

2.4.5 Cracking of flexural loaded beam

The axially loaded concrete prism can be used to describe the cracking process of the tensile zone of a beam loaded in bending. In Figure 2.15 a schematic explanation of crack formation of a beam subjected to a bending moment is illustrated. According to Al-Emrani et al. (2011), tests have shown that the crack distance decreases when a structure is loaded by a bending moment compared to uniaxial tensile loading. Further, the crack spacing is decreased with increasing curvature of the beam.

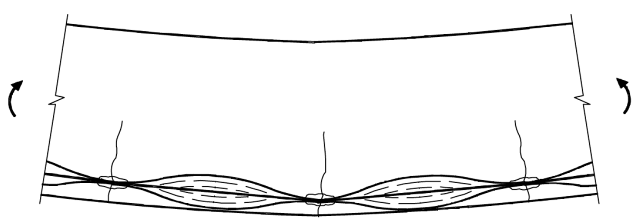

Figure 2.15 The principle of flexural loaded structure with tensile concrete stress between two cracks (Al-Emrani et al., 2011).

One important thing to mention is that the cracking process described above is valid for cracking in SLS and is based on the approach used in Eurocode. However, in this thesis the behaviour of the structure beyond the SLS is of interest. To describe the structural behaviour at rupture of the reinforcement a theory based on plastic deformation capacity is needed since the structure will have considerable plastic deformation at rupture. Ansell and Svedbjörk (2000) refer to this stage as state IV.

3 Plastic deformation capacity

3.1 Introduction

Reinforced concrete is a composite material and it can show either brittle or ductile response depending on the reinforcement ratio and material properties. As a result of ductility, plastic hinges are formed where reinforcement yields and stiffness finds the lowest value along the beam at the place of plastic hinge. With change of stiffness a moment redistribution takes place due to non-linear behavior of material and increases load carrying capacity while deformations increase (Johansson & Laine, 2012).

To study structural behavior under impulse load the energy absorption capacity is of great importance and according to Johansson and Laine (2012) plastic hinges provide plastic redistribution of stresses and consequently, higher energy absorption capacity. It is often assumed that a plastic hinge takes place in a concentrated point while it distributes over a plastic region as shown in Figure 3.1.

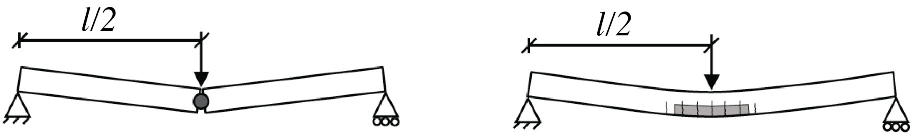

(a) Assumption of concentrated hinge. *(b) Real distribution of plastic hinge.*

Figure 3.1 Plastic hinge representation (Lozano & Makdesi, 2017).

With formation of plastic hinges as a consequence of ductile behavior from a structure subjected to loading, the structural element deforms. The resulting rotation is interpreted as plastic rotation and the deformation caused by this rotation is plastic deformation. According to Engström (2014) plastic rotational capacity is the rotation of plastic hinge when the load increases from yielding to collapse. This concept has a close connection to energy absorption capacity of structure as it is related to ductility. Therefore, high plastic deformation capacity in a structure ensures higher capacity of energy absorption.

3.2 Relation of plastic rotational capacity and curvature

3.2.1 Definition of curvature

Considering the strain distribution of a reinforced concrete cross section, strain in any section can be derived as (Engström, 2014)

$$\varepsilon_c(z) = \varepsilon_{cm} + \frac{1}{r} \cdot z \tag{3.1}$$

Where ε_{cm} is mean strain or strain in center of gravity, r is curvature radius, $\frac{1}{r}$ is curvature and z is distance from gravity center, see Figure 3.2.

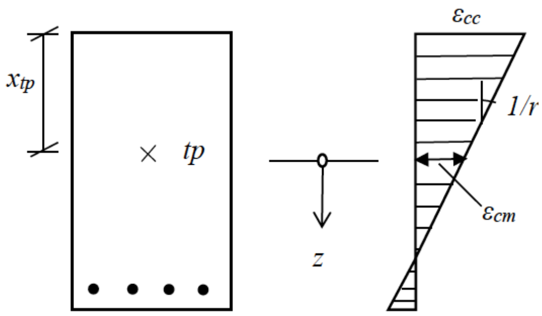

Figure 3.2 Strain distribution in a reinforced concrete cross section (Jönsson & Stenseke, 2018).

Denoting curvature as χ and considering a beam with constant curvature, where $d\varphi$ is change of angle over element length and dx is element length along gravity axis, it can be written

$$dx = r \cdot d\varphi \quad \Rightarrow \quad \chi = \frac{1}{r} = \frac{d\varphi}{dx} \tag{3.2}$$

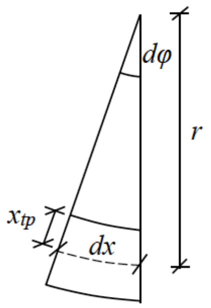

Figure 3.3 Relation of curvature radius and deformation (Jönsson & Stenseke, 2018).

For an infinitely small element, curvature can be derived as angle change per unit length, where ε_{cc} is concrete compressive strain, ε_{ct} is concrete tensile strain and ε_s is steel strain.

$$\chi = \frac{1}{r} = \frac{\varepsilon_{cc}}{x} = \frac{\varepsilon_{cc} + \varepsilon_{ct}}{h} \tag{3.3}$$

$$\chi = \frac{1}{r} = \frac{\varepsilon_s}{d - x} = \frac{\varepsilon_{cc} + \varepsilon_s}{d} \tag{3.4}$$

According to Jönsson and Stenseke (2018) Equations (3.3) and (3.4) can always be used for states I, II, III and also for different material properties.

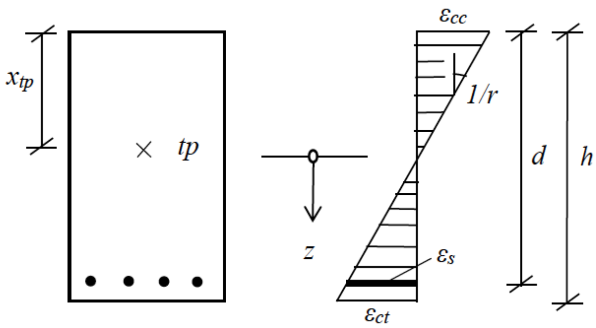

Figure 3.4 Geometry of cross section and strain distribution (Jönsson & Stenseke, 2018).

3.2.2 Theoretical explanation for plastic rotation

According to Engström (2015) plastic rotation can be derived by integration of plastic curvature over the length l_y at which strain of steel goes above yielding strain to ultimate strain.

$$\theta_{pl} = \int_{l_y} (\chi(x) - \chi_y)dx \tag{3.5}$$

Figure 3.5 shows moment-curvature diagram and two corresponding strain distributions for cross sections at yielding and ultimate states. Also, there is a simplified bi-linear diagram based on elasto-plastic material response.

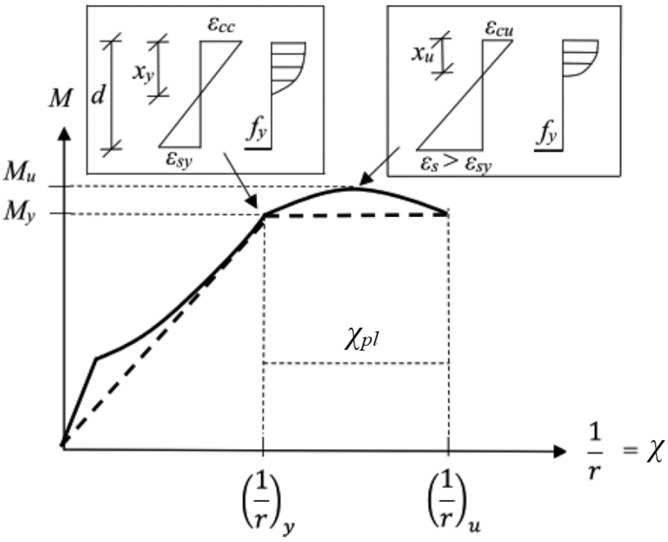

Figure 3.5 Moment curvature diagram for a concrete cross section reinforced at the bottom and simplified bi-linear diagram (Jönsson & Stenseke, 2018).

When reinforcement starts yielding, concrete and steel strain can be denoted as ε_{cy} and ε_{sy} respectively and the height of the compressive zone as x_y. Therefore, curvature at the beginning of plastic deformation can be derived as

$$\chi_y = \left(\frac{1}{r}\right)_y = \frac{\varepsilon_{cy}}{x_y} = \frac{\varepsilon_{sy}}{d - x_y} \tag{3.6}$$

For failure, depending on concrete crushing or reinforcement rupture the equations for curvature can vary

Concrete crushing: $$\chi_u = \left(\frac{1}{r}\right)_u = \frac{\varepsilon_{cu}}{x_u} = \frac{\varepsilon_s}{d - x_u} \tag{3.7}$$

Reinforcement failure: $$\chi_u = \left(\frac{1}{r}\right)_u = \frac{\varepsilon_{cc}}{x_u} = \frac{\varepsilon_{su}}{d - x_u} \tag{3.8}$$

The plastic curvature can be estimated as

$$\chi_{pl} = \left(\frac{1}{r}\right)_{pl} = \left(\frac{1}{r}\right)_u - \left(\frac{1}{r}\right)_y \tag{3.9}$$

$$\chi_{pl} = \left(\frac{1}{r}\right)_{pl} = \frac{\varepsilon_s}{d - x_u} - \frac{\varepsilon_{sy}}{d - x_y} \approx \frac{\varepsilon_s - \varepsilon_{sy}}{d - x_u} \tag{3.10}$$

Both reinforcement strain and plastic curvature vary between yielding state and failure state. Therefore, plastic rotation can be calculated by integration of plastic curvature for all sections along l_y (Jönsson & Stenseke, 2018)

$$\theta_{pl} = \int_0^{l_y} \left(\frac{\varepsilon_s(x) - \varepsilon_{sy}}{d - x_u}\right) dx \tag{3.11}$$

According to Engström (2015) although Equation (3.11) is theoretically correct and it provides a basic theoretical definition it cannot be used for calculation of real plastic rotation as practically this parameter is dependent on several factors such as material properties, amount of reinforcement and geometry, loading, cracking, tension stiffening and bond slip, definition of yielding curvature and ultimate curvature.

3.2.3 Ratio of $\frac{M_u}{M_y}$ and plastic rotation

Ultimate and yielding values have a significant role in estimation of plastic rotational capacity. In theoretical methods the ratio between ultimate moment M_u and yielding moment M_y is a decisive factor influencing plastic rotational capacity and length of plastic hinge. This ratio is based on moment distribution which depends on load application and boundary conditions. In Figure 3.6 three different load cases are shown for a simply supported beam and case (a) is the only case that Eurocode 2 estimates the rotational capacity for. The parameter l_y is the length of yielding region which increases from three-point loading to uniform load case showing that the plastic rotational capacity also increases by increment of M_u/M_y.

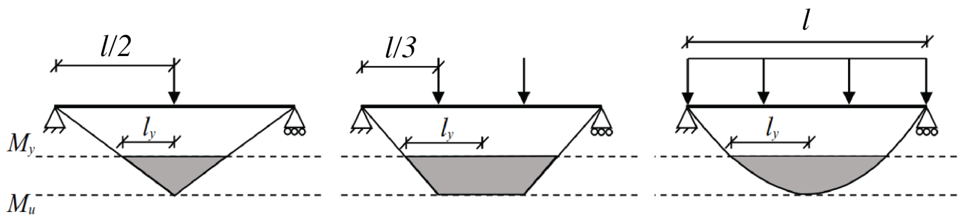

Figure 3.6 Moment diagrams for three different load cases for a simply supported beam.

From the ratio between ultimate moment to yielding moment M_u/M_y the ratio between ultimate load to yielding load f_u/f_y can be derived. Larger values of M_u/M_y lead to larger f_u/f_y ratio and higher capacity of plastic rotation in a structure. Table 3.1 provides the values of ε_{su} and f_u/f_y for reinforcement classes A, B and C showing that ductility increases as a result of larger ultimate strain and f_u/f_y ratio.

Table 3.1 Values of f_u/f_y and ε_{su} for reinforcement classes A, B, and C.

Reinforcement class	f_u/f_y	ε_{su}
A	1.05	25‰
B	1.08	50‰
C	1.15	75‰

3.3 Different methods for calculation of plastic rotational capacity

Plastic deformation capacity is a complex phenomena and the results for calculation of plastic rotational capacity have a wide variety due to its dependence on several parameters and as a result different methods have been introduced to estimate this parameter.

3.3.1 Plastic rotation estimation from test results

Definition of yielding and ultimate values is an important step for calculation of plastic rotation. Eurocode 2 (CEN, 2004) defines the ultimate deformation value corresponding to ultimate load in critical section but ultimate deformation is often not presented in a load-displacement curve from test results as the structure experiences considerable deformations after reaching the maximum load values. In order to obtain a more robust definition, Betonghandboken (1990) suggests a method which is based on an utilized value considering elastic deformation and ultimate deformation corresponding to 95% of F_{max}. This approximation estimates plastic rotational capacity based on relationship between load and deformation.

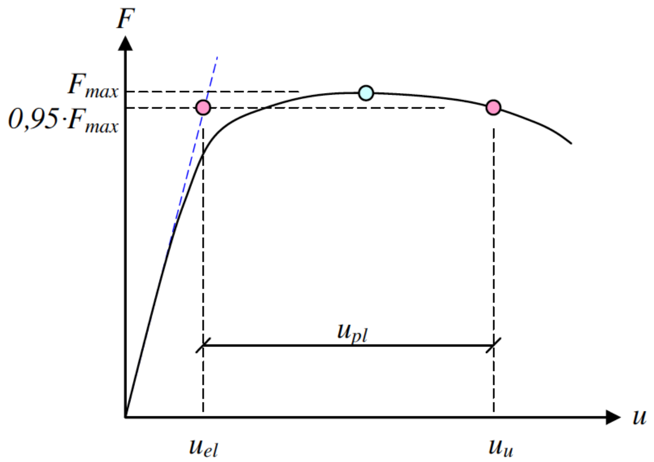

Figure 3.7 The value of $0.95 \cdot F_{max}$ *in load-deformation curve (Johansson & Laine, 2012).*

Therefore, u_{pl} can be defined as:

$$u_{pl} = u_u - u_{el} \tag{3.12}$$

where u_u represents the total deformation of the beam at 95% of maximum load on the descending branch and u_{el} indicates the elastic deformation at the same load level. From this, for the cases illustrated in Figure 3.7, the plastic rotational capacity can be calculated as (Johansson & Laine, 2012)

$$\theta_{pl} = \frac{u_{pl}}{l_0} \tag{3.13}$$

the parameter l_0 is the length between zero moment and plastic hinge which is dependant on loading type and boundary conditions.

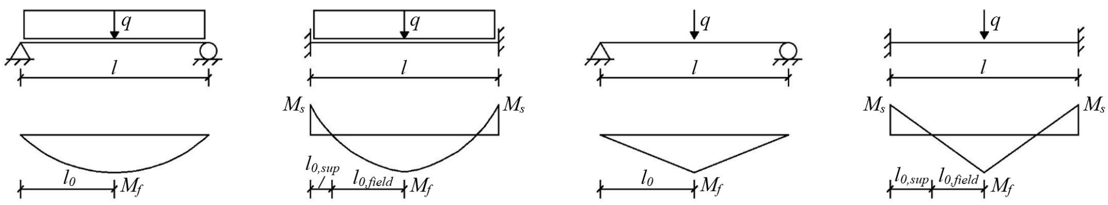

Figure 3.8 Length of l_0 for two different types of loading and boundary conditions.

Parameter a is the distance between support and the point at which concentrated load is applied. As shown is Figure 3.9 for a special case which is studied in this project and is simply supported, subjected to four-point bending, and the distance between loads is equal to the distance between each support and load, it can be said that $a = l_0 = l/3$ and the plastic rotation can be determined as

$$\theta_{pl} = \frac{3 \cdot u_{pl}}{l} \tag{3.14}$$

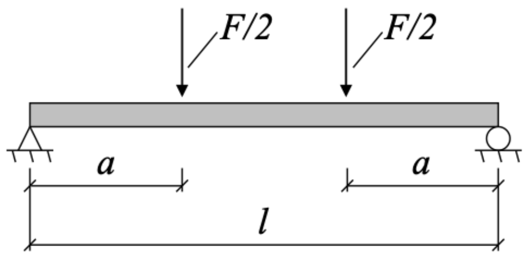

Figure 3.9 Simply supported beam subjected to four-point bending.

3.3.2 BK 25 method

FKR 2011 is a set of certain design regulations from the Swedish Fortification Agency which is based on *BK 25* Method. According to Swedish Fortifications Agency, plastic rotational capacity for a reinforced concrete beam subjected to impulse load can be estimated considering a simply supported beam with uniformly distributed load using *BK 25* method (Johansson & Laine, 2012).

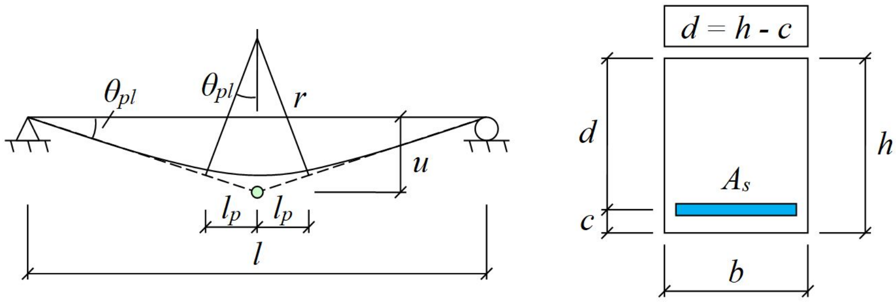

Figure 3.10 Geometry definitions of a simply supported beam based on Johansson and Laine (2012).

In this method the length of the equivalent plastic hinge, l_p with constant curvature is defined as

$$l_p = 0.5 \cdot d + 0.15 \cdot l \tag{3.15}$$

Which is directly used in calculation of plastic rotational capacity, θ_{pl}

$$\theta_{pl} = \frac{l_p}{r} \tag{3.16}$$

Total plastic deformation caused by plastic hinge at mid-span is

$$u = \frac{\theta_{pl} \cdot l}{2} \tag{3.17}$$

for a cross section at ultimate moment, curvature is defined according to Equation (3.7)

$$\chi_u = \frac{1}{r} = \frac{\varepsilon_{cu}}{x} = \frac{\varepsilon_s}{d - x} = \frac{M}{EI} \tag{3.18}$$

For a beam with tensile reinforcement at bottom layer, considering yielding of reinforcement, the compressive block height can be solved as

$$x = \frac{\omega_s \cdot d}{0.8} \tag{3.19}$$

where ω_s is mechanical ratio of tensile reinforcement and ρ_s is reinforcement ratio parameter defined as

$$\rho_s = \frac{A_s}{b \cdot d} \tag{3.20}$$

$$\omega_s = \rho_s \cdot \frac{f_y}{f_c} \tag{3.21}$$

$\omega_{s,crit}$ is a limit for mechanical ratio that specifies the failure mode. If ($\omega_s > \omega_{s,crit}$) the failure is due to concrete crushing, otherwise, reinforcement rupture is the reason of failure.

$$\omega_{s,crit} = \frac{0.8 \cdot \varepsilon_{cu}}{\varepsilon_{cu} + \varepsilon_{su}} \tag{3.22}$$

Finally, the plastic rotational capacity in the span can be obtained considering the failure mode.

Failure due to concrete crushing ($\omega_s > \omega_{s,crit}$)

$$\theta_{pl} = \frac{l_p}{r} = \frac{0.8 \cdot \varepsilon_{cu}}{\omega_s \cdot d} \cdot (0.5 \cdot d + 0.15 \cdot l) = \frac{0.4 \cdot \varepsilon_{cu}}{\omega_s}(1 + 0.3 \cdot \frac{l}{d}) \tag{3.23}$$

Failure due to reinforcement rupture ($\omega_s < \omega_{s,crit}$)

$$\theta_{pl} = \frac{l_p}{r} = \frac{0.8 \cdot \varepsilon_{su}}{d \cdot (0.8 - \omega_s)} \cdot (0.5 \cdot d + 0.15 \cdot l) = \frac{0.4 \cdot \varepsilon_{su}}{(0.8 - \omega_s)}(1 + 0.3 \cdot \frac{l}{d}) \tag{3.24}$$

Also, considering fixed supports for the same beam at Figure 3.10, the equivalent plastic hinge takes a shorter value compared to a simply supported beam.

$$l_p = 0.5 \cdot d + 0.1 \cdot l_1 \tag{3.25}$$

where l_1 can be described as the ratio of bending moment to shear force at support

$$l_1 = \frac{M_{sup}}{V_{sup}} \tag{3.26}$$

If $M_{sup} = M_{field}$ this ratio can be derived as

$$l_1 = 0.125 \cdot l \tag{3.27}$$

Therefore, plastic rotational capacity for a beam with fixed supports can be derived as

Failure due to concrete crushing ($\omega_s > \omega_{s,crit}$)

$$\theta_{pl} = \frac{l_p}{r} = \frac{0.8 \cdot \varepsilon_{cu}}{\omega_s \cdot d}(0.5 \cdot d + 0.1 \cdot l_1) = \frac{0.4 \cdot \varepsilon_{cu}}{\omega_s}(1 + 0.2 \cdot \frac{l_1}{d}) \tag{3.28}$$

Failure due to reinforcement rupture ($\omega_s > \omega_{s,crit}$)

$$\theta_{pl} = \frac{l_p}{r} = \frac{0.8 \cdot \varepsilon_{su}}{d \cdot (0.8 - \omega_s)}(0.5 \cdot d + 0.15 \cdot l_1) = \frac{0.4 \cdot \varepsilon_{su}}{(0.8 - \omega_s)}(1 + 0.2 \cdot \frac{l_1}{d}) \tag{3.29}$$

3.3.3 Eurocode 2

Definition of plastic rotational capacity in Eurocode 2

According to Eurocode 2 (CEN, 2004) plastic rotational capacity, $\theta_{pl,EC}$, for a continuous beam is defined as the rotation over an inner support. Also, the length of rotation is assumed 1.2 times of support section depth.

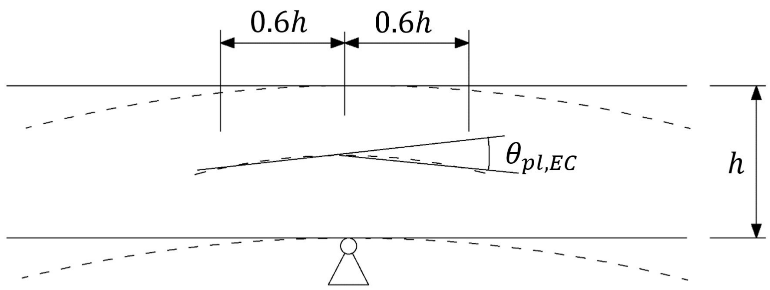

Figure 3.11 Plastic rotational capacity based on Eurocode 2.

For an equivalent simply supported beam with concentrated load and a length corresponding to zero moments over the support of mentioned continuous beam, the rotation of mid-span is approximately equal to the same value of $\theta_{pl,EC}$ (Latte, 1999).

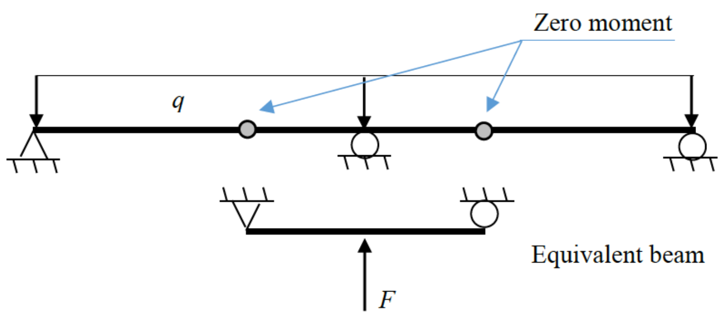

Figure 3.12 Simply supported beam equivalent to a continuous beam for plastic rotation capacity calculation (Lozano & Makdesi, 2017).

According to Eurocode 2, the plastic rotation capacity in the middle of this equivalent beam is twice the rotation at its support which corresponds to the value of plastic rotation presented by BK 25.

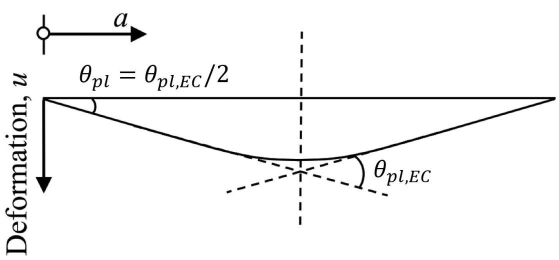

Figure 3.13 The relation between plastic rotational capacity and support rotation for equivalent simply supported beam based on Lozano and Makdesi (2017).

Plastic rotational capacity and x/d ratio

Eurocode 2 provides a simplified procedure in which there is a relation between plastic rotational capacity and x/d depending on reinforcement class and concrete class (CEN, 2004). For this approach the following conditions must be checked for plastic hinge regions

For concrete classes less than or equal to C50/60:

$$\frac{x_u}{d} \leq 0.45 \tag{3.30}$$

For concrete classes greater than or equal to C55/67:

$$\frac{x_u}{d} \leq 0.35 \tag{3.31}$$

A correction factor k_λ which depends on shear slenderness should be multiplied to $\theta_{pl,EC}$

$$k_\lambda = \sqrt{\frac{\lambda}{3}} \tag{3.32}$$

$$\theta^*_{pl,EC} = k_\lambda \cdot \theta_{pl,EC} \tag{3.33}$$

l_0 denotes the distance between sections with zero moment and maximum moment after redistribution, d is effective depth and λ is shear slenderness defined as

$$\lambda = \frac{l_0}{d} \tag{3.34}$$

The significant difference in Figure 3.14 shows how more ductile reinforcement provide larger plastic rotational capacity.

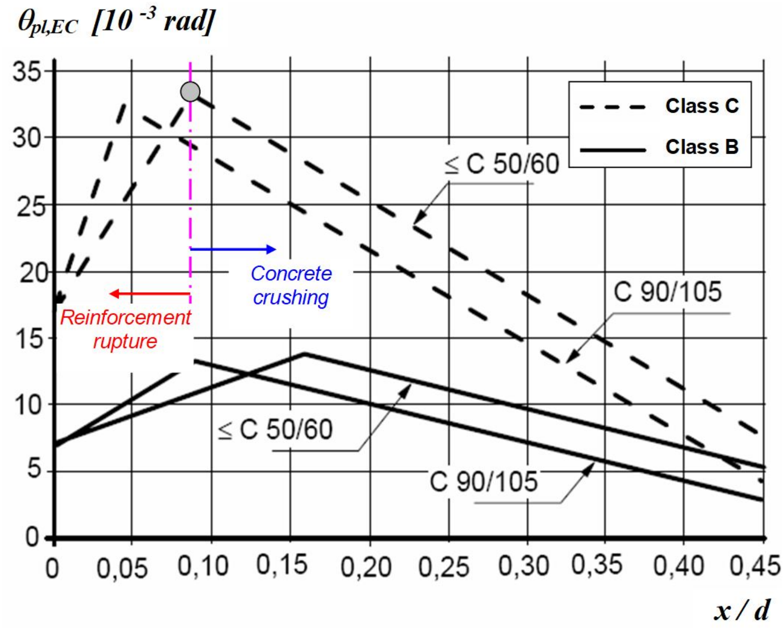

Figure 3.14 Allowable rotation of reinforced concrete sections for different concrete classes, and Class B and C steel reinforcement. Valid for shear slenderness λ=3. Modified from CEN (2004).

When reinforcement rupture failure mode is decisive, the steel bars use their strain capacity completely and $\theta_{pl,EC}$ increases by increasing x/d ratio. While for concrete crushing failure mode $\theta_{pl,EC}$ decreases by increasing x/d ratio as concrete crushing happens when steel strain capacity has not been fully utilized.

As shown in Table 3.1 reinforcement bars in class C have larger value of f_u/f_y and a larger ultimate strain which leads to a higher rotational capacity. It is also observed in Figure 3.14 that plastic rotational capacity is considerably larger for class C reinforcement with more ductile behaviour.

3.3.4 German method (background of Eurocode 2)

According to Zilch and Zehetmaier (2010) and CEB (1998) there is an earlier numerical model provided by a German approach called "Stuttgart method". This method considering an equation for calculation of plastic rotation in which plastic rotation for an internal support of a continuous beam under distributed load is the same as plastic rotation for mid-section of a simply supported beam under point load and with a length corresponding to distance between zero-moment points as shown in Figure 3.15. This approach is a base for what is presented in Eurocode 2.

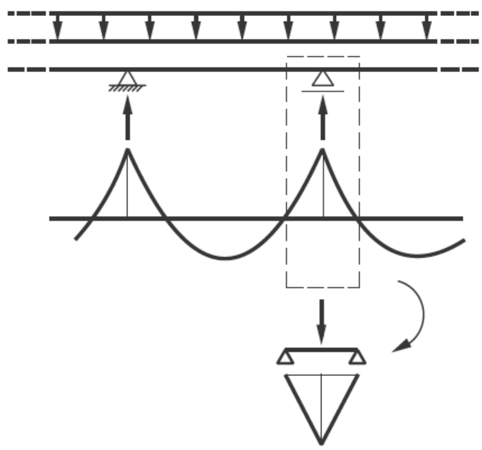

Figure 3.15 Plastic rotation of an internal support in continuous beam under distributed load equivalent to plastic rotation of midspan in a simply supported beam under concentrated load (Zilch & Zehetmaier, 2010).

In this method, the moment-curvature diagram is estimated for a confined and an unconfined model based on provided geometry and stress-strain curves for steel and concrete taking Euler–Bernoulli assumption so plane sections remain plane.

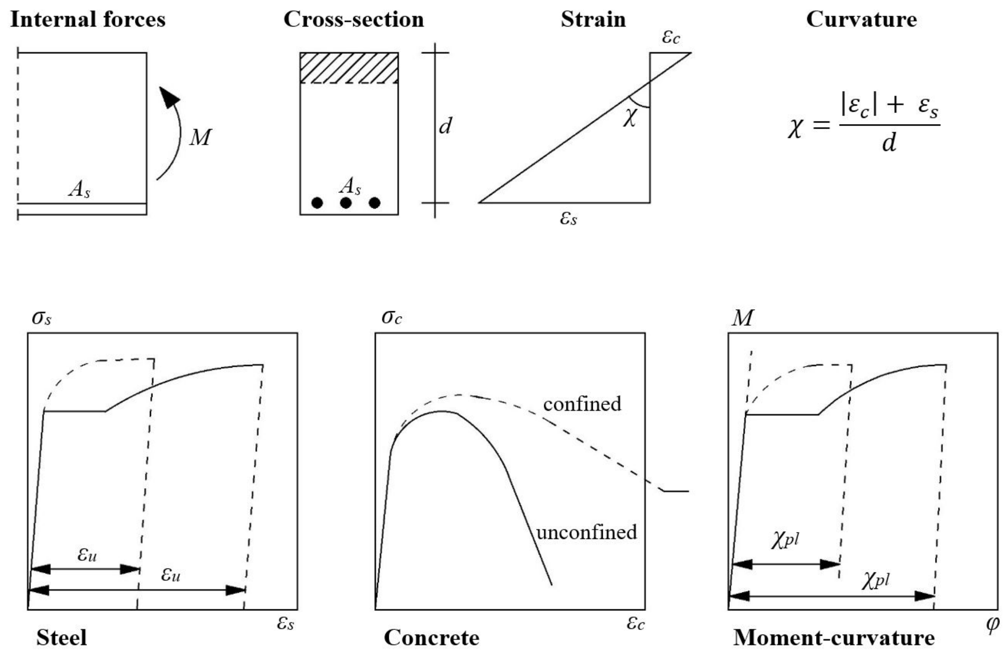

Figure 3.16 Moment-Curvature model from Stuttgart method (CEB, 1998).

From moment-curvature relationship, tensile force-curvature and as a result, curvature in cracks can be anticipated as shown in Figure 3.17. Where dash line represents confined model not considering cracks.

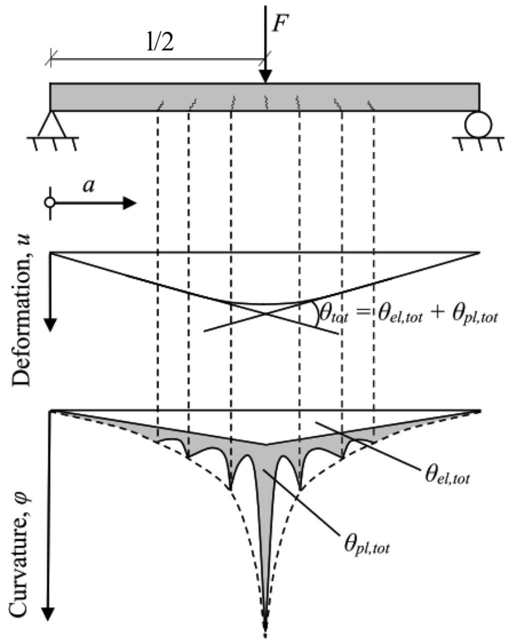

Figure 3.17 Integration of curvature from Stuttgart model (CEB, 1998).

CEB (1998) defines plastic rotation as the difference between rotation at yielding of reinforcement and rotation at ultimate load. Also, Eurocode 2 is based on this definition.

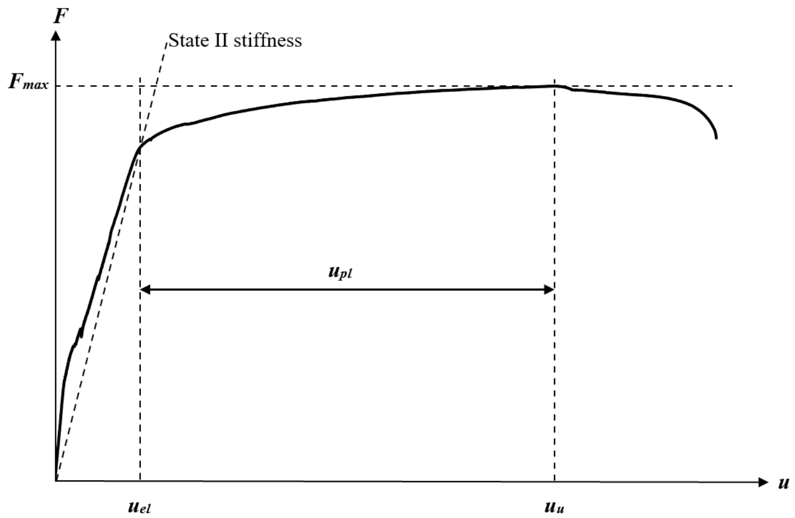

Figure 3.18 Schematic definition of plastic deformation based on Eurocode 2 and CEB (1998).

In addition, Stuttgart method introduces the relation between plastic rotation and percentage of reinforcement. This approach is also used in Eurocode 2 to provide the graph in Figure 3.14. Although, it is not clearly mentioned in Eurocode 2, but according to CEB (1998), Zilch and Zehetmaier (2010) and DAfStb (2010) Figure 3.14 is based on f_u/f_y ratio.

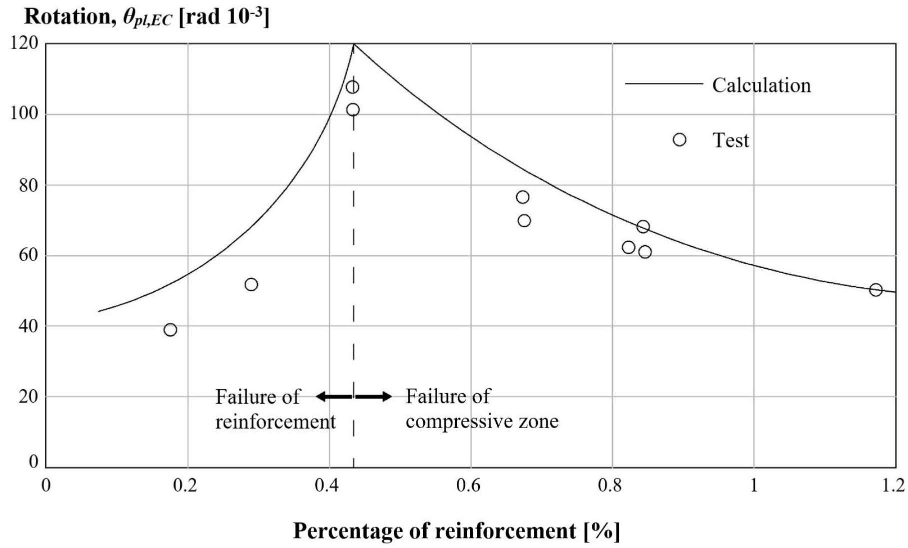

Figure 3.19 Relation between rotation and percentage of reinforcement from Stuttgart model (CEB, 1998).

Finally, Zilch and Zehetmaier (2010) gives the following equation based on Stuttgart model to calculate plastic rotational capacity.

$$\theta_{pl,EC} = \beta_n \cdot \beta_s \cdot \frac{\varepsilon^*_{su} - \varepsilon_{sy}}{1 - \frac{x_d}{d}} \cdot \sqrt{\frac{\lambda}{3}} \cdot 10^3 \qquad [mrad] \tag{3.35}$$

where

$$\varepsilon^*_{su} = min \begin{cases} 0.28 \cdot \left(\beta_{cd} \cdot \frac{x_d}{d}\right)^{0.2} \cdot \varepsilon_{uk} & \text{(steel failure)} \\ \\ 1.75 \cdot \left(\frac{x_d}{d}\right)^{\frac{2}{3}} \cdot \left(1 - \left(\frac{x_d}{d}\right)^{-1}\right) \cdot \varepsilon_{c1u} & \text{(concrete failure)} \end{cases} \tag{3.36}$$

Different parameters included in equation of plastic rotation capacity are defined as

$$\beta_n = 22.5 \tag{3.37}$$

$$\beta_s = (1 - \frac{f_{yk}}{f_{uk}}) \tag{3.38}$$

$$\beta_{cd} = \left(\frac{-0.0035}{\varepsilon_{c1u}}\right)^3 \tag{3.39}$$

While, ε^*_{su} is steel ultimate strain with simplified consideration of tension stiffening, ε_{uk} is steel ultimate strain at maximum load and ε_{sy} is steel ultimate strain at yielding. ε_{c1u} denotes concrete strain limit at maximum load, f_{yk} represents yielding strength of reinforcement and f_{tk} is tensile strength of reinforcement.

Johansson et al. (2021) provides a study on effect of f_u/f_y ratio and ε_{su} on plastic rotational capacity based on the background of Eurocode. From this study,

Figure 3.20 shows the relation between plastic rotational capacity and x/d ratio for reinforced concrete specimen with steel classes A, B, C, Ks 40 (1), and Ks 40 (2)[1]. The reinforcement classifications Ks 40 (1), and Ks 40 (2) are from old Swedish regulations which were used until 1995. It is obvious that reinforcement Ks 40 is noticeably better than reinforcements A, B, and C.

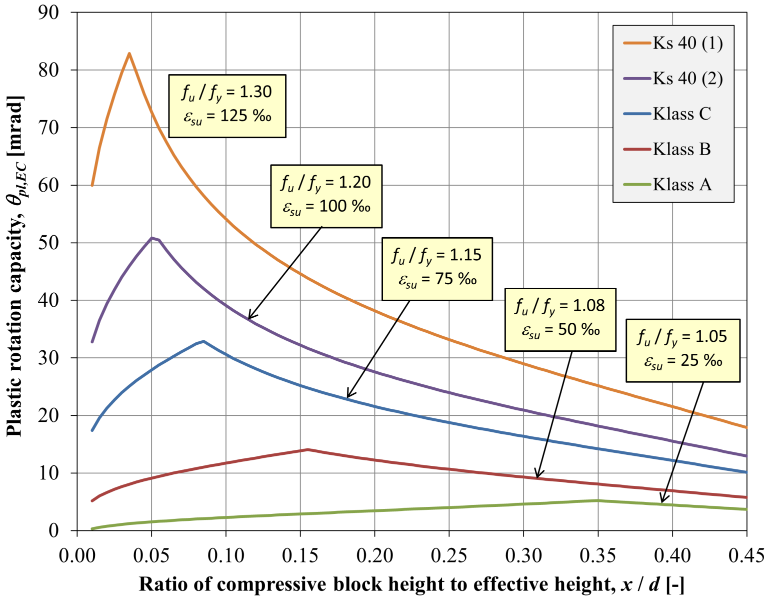

Figure 3.20 Relation between plastic rotation and x/d ratio for reinforced concrete specimen with steel classes A, B, C, ks40(1), and ks40(2).

According to Johansson et al. (2021) having a constant value for the ratio of f_u/f_y leads to higher plastic rotation capacity for a bar with higher value of ultimate strain. Also, larger constant value of f_u/f_y results in larger plastic rotation capacity. Similarly, keeping ε_{su} constant shows higher plastic rotation capacity for a bar with larger ductility and larger constant value of ultimate strain provides larger plastic rotation capacity.

[1]The properties of Ks 40 was never defined and are estimated by Johansson et al. (2021)

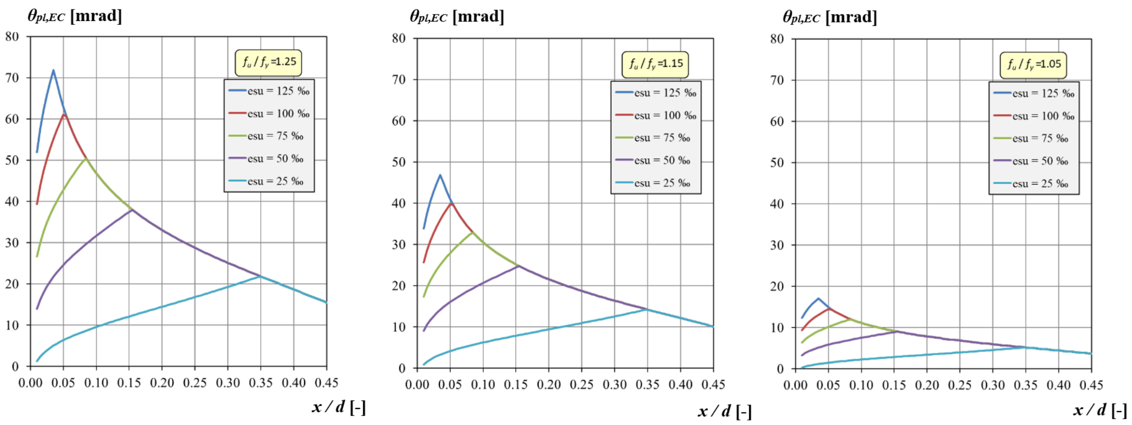

Figure 3.21 *Relation between plastic rotation and x/d ratio for reinforced concrete specimen with steel classes A, B, C, ks40(1), and ks40(2) by keeping f_u/f_y constant.*

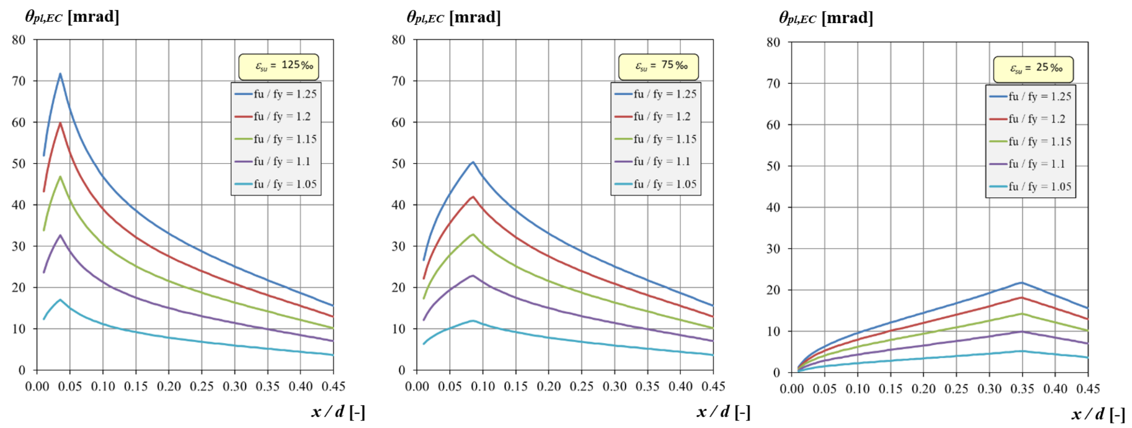

Figure 3.22 *Relation between plastic rotation and x/d ratio for reinforced concrete specimen with steel classes A, B, C, ks40(1), and ks40(2) by keeping ε_{su} constant.*

3.3.5 Betonghandboken 1990 (ABC method)

This is an empirical method to calculate plastic rotation for a reinforced concrete beam under static loading and on one side of critical cross section provided by Betonghandboken 1980 (Lozano & Makdesi, 2017). As mentioned in Section 3.3.1, Betonghandboken considers the plastic rotations corresponding to 95% of ultimate load and in order to calculate it, three parameters are used considering different factors affecting plastic rotational capacity.

$$\theta_{pl,95\%} = A \cdot B \cdot C \cdot 10^{-3} \tag{3.40}$$

Factor A is derived based on amount of tensile, compression and transverse reinforcement with strength values from Swedish concrete code

$$A = 1 + 0.6 \cdot \omega_v + 1.7 \cdot \omega_s^{'} - 1.4 \cdot \frac{\omega_s}{\omega_b} \geq 0.05 \tag{3.41}$$

ω_v denotes mechanical ratio of stirrups, $\omega_s^{'}$ is mechanical ratio of reinforcement in compression and ω_s is mechanical ratio of reinforcement in tension

$$\omega_v = \frac{A_v}{b \cdot s} \cdot \frac{f_y}{f_{ct}} \tag{3.42}$$

$$\omega_s^{'} = \frac{A_s^{'}}{b \cdot d} \cdot \frac{f_y}{f_{cc}} \tag{3.43}$$

$$\omega_s = \frac{A_s}{b \cdot d} \cdot \frac{f_y}{f_{cc}} \tag{3.44}$$

Parameters A_v, $A_s^{'}$ and A_s are areas of reinforcement in shear, compression and tension, respectively. f_y is strength value of reinforcement. f_{ct} denotes concrete tensile strength and f_{cc} is concrete compressive strength. Parameter b is width of cross section, s is distance of stirrups and d is effective height. Considering ultimate strain of concrete as $\varepsilon_{cu} = 3.5‰$ and reinforcement yield strain as $\varepsilon_{sy} = f_y/E_s$

$$\omega_b = \frac{0.8 \cdot \varepsilon_{cu}}{\varepsilon_{cu} + \varepsilon_{sy}} \tag{3.45}$$

For measured values of strength, the following equation can be used for A

$$A = 1 + 1.3 \cdot \omega_v + 3 \cdot \omega_s^{'} - 5 \cdot \omega_s \qquad (0.05 \leq A \leq 2.30) \tag{3.46}$$

Factor B is derived based on shape of the stress-strain diagram for reinforcement and has different values depending on type and grade of bars. The reinforcement classification in Table 3.2 is from old Swedish regulations which were used until 1995.

Table 3.2 Values for factor B. ε_p is the strain value for prestressing steel (Jönsson & Stenseke, 2018)

Type of reinforcement	B	Max A.B
Ks 60, Ks 40*, Ss 26, Ss 26S	1.0	1.7
Ks 60S, Ks 40S	0.8	1.1
Cold-worked steel with $\varepsilon_{su} \geq 3\%$ and $f_t/f_y \geq 1.1$	$0.6 \cdot \left(1 - 0.7 \cdot \frac{\varepsilon_p}{\varepsilon_{su}}\right)$	0.5

*NOTE: Values for Ks 60 and Ks 40 can be used if $\varepsilon_{su} \geq 8\%$ and $f_t/f_y \geq 1.4$. The letter S in Ks 60S and Ks 40S indicates that the reinforcement can be welded and it should be considered that ductile properties will be reduced after welding.

Factor C is derived based on the placement of plastic hinge and can be calculated as

$$C_{sup} = 10 \cdot \frac{l_{0,sup}}{d} \tag{3.47}$$

$$C_{field} = 7 \cdot \frac{l_{0,field}}{d} \tag{3.48}$$

while $l_{0,sup}$ and $l_{0,field}$ are defined as shown in Figure 3.8.

ABC method and BK 25 use the same definition of plastic rotation. BK 25 studies a beam under uniformly distributed load with fixed supports while Eurocode 2 considers a simply-supported beam with point load. With a similar approach to the idea presented in Figure 3.12, fixed supports on a beam can be taken as internal support in a continuous beam. Considering an equal simply supported beam subjected to a point load in midspan, the rotation values from BK 25 and ABC method can be the same value as the support rotation in Figure 3.13. Therefore, in order to compare the results from BK 25 or ABC method with Eurocode 2, values from Eurocode 2 must be multiplied by a factor 0.5.

4 Previous testing

4.1 Introduction

This chapter provides a summary from two sets of studies on plastic deformation capacity of reinforced concrete elements which were performed at Chalmers University of Technology 2020 and KTH from 2000 to 2005. These projects are also used as reference and study background for this thesis. Hence, a short description of mentioned projects and their results are provided.

4.2 Chalmers experiment

This project is a continuation of a BSc thesis made by Köseoğlu (2020). The project was meant to study the average reinforcement strain and how the strain is affected by altered parameters. The experiments were performed under static axial tensile loading as a simplification to study the average strain of reinforcement bars i order to estimate the plastic rotational capacity.

Eighteen reinforced concrete prisms with one centralized reinforcement bar were subjected to static tensile load until failure, see Figure 4.1. Difference in size of reinforcement bars ($\phi 16, \phi 12, \phi 10$) and implementing PVC tube segments around some of the $\phi 12$ bars with different configurations to reduce the bond resulted in different strain values. Strain fields, crack widths and total displacements were studied for each prism using data from DIC.

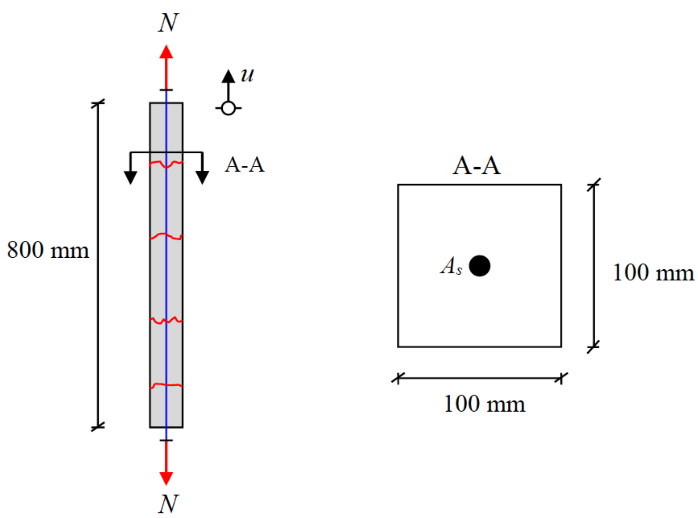

Figure 4.1 Reinforced concrete prism geometry and cross section (Köseoğlu, 2020).

The test results showed that with increased bar diameter the average strain value also increased, more cracks were observed and influence of concrete between cracks decreased. Prisms with PVC tubes showed fewer cracks compared with prisms with full interaction. Also, it was expected that the plastic deformation capacity increases by reduction of interaction between steel and concrete while, the results showed the reverse and lower values of strains and total displacements were obtained with increasing PVC volumes. How the average reinforcement strain varies with applied tensile force for the different bar sizes with and without plastic tubes is presented in Figure 4.2.

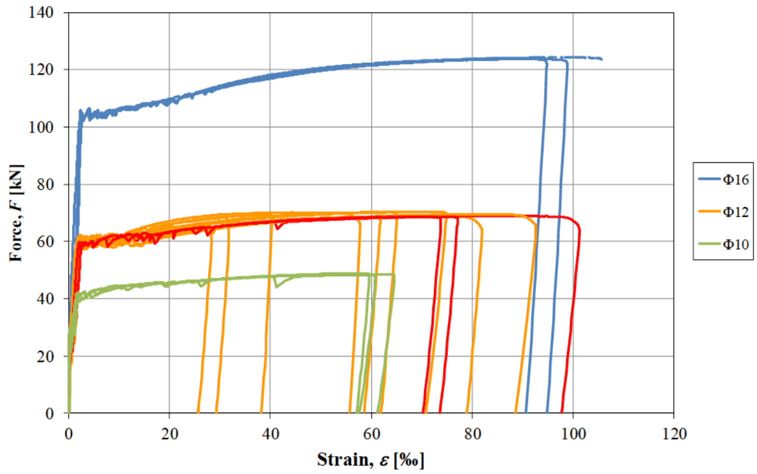

Figure 4.2 *Results for all reinforced concrete prisms. Red curves represent ϕ12 prisms without PVC and orange curves represent ϕ12 prisms with PVC (Köseoğlu, 2020).*

The average strains at rupture in the reinforcement bars without PVC tubes were 9% in the ϕ16, 7% in ϕ12 and 6% in ϕ10. The average reinforcement strain in the bars with PVC tubes was approximately equal to 6.5%, compared with the 7% for the ϕ12 prisms without PVC tubes. However, it was predicted that the results will be different in beams due to different reinforcement ratio and configuration and also uneven concrete cover.

4.3 KTH experiments

Previous research about impulse loaded structures and plastic deformation capacity have been preformed at KTH university in Stockholm. A series of static and dynamic tests on concrete slab strips have been performed on behalf of the Swedish Armed force between the years 2000-2005.

Today's modern reinforcement has a decreased ratio between the yielding strength and the ultimate strength (Ansell & Svedbjörk, 2000). Therefore, the aim of the test series was to compare the plastic behaviour and plastic rotational capacity between concrete members with the new reinforcement, B500BT and the previous used Ks40 and Ps50. The test set-up from KTH is similar to the one used in this thesis with a four-point bending test, shown in Figure 4.3. During the test, the applied load was measured and the corresponding deformation was registered.

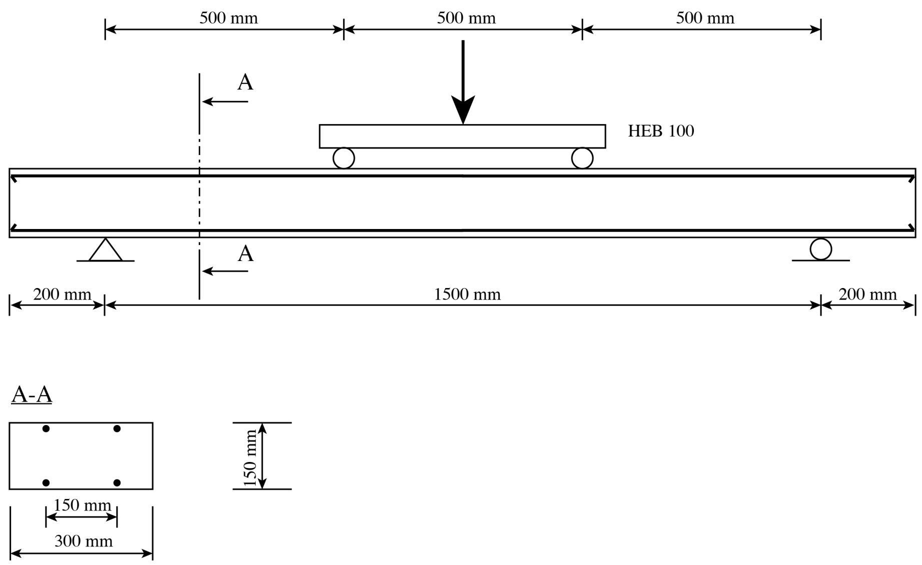

Figure 4.3 *Illustration of the test set-up from the four-point bending test of a slab strip from test conducted at KTH.*

Before the casting, the reinforcement bars were marked every 50 mm and after the tests, the bottom reinforcement was removed and the strain difference between two marks was evaluated. The results were presented in bar charts and an example of the strain distribution of on of the slab strip with reinforcement quality B500BT is presented in Figure 4.4.

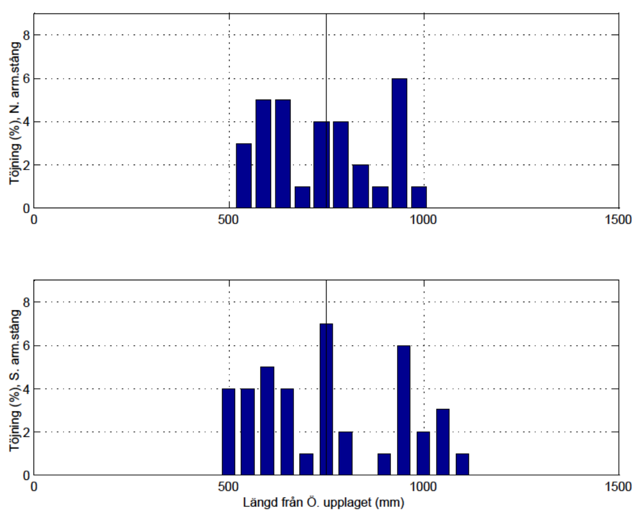

Figure 4.4 *Example of results from the measured strain distribution in the bottom reinforcement. The first diagram is the strain difference in the reinforcement bar to the left and the second diagram for the reinforcement bar to the right (Ansell & Svedbjörk, 2000).*

Johansson and Laine (2012) summarized the results from the test series at KTH for simply supported slab strips with varying cross sections, reinforcement amount and reinforcement quality, see Table 4.1.

Table 4.1 Summary of the average strain results from tests conducted at KTH (Johansson & Laine, 2012).

Reference [1)]	Name	l [mm]	b [mm]	h [mm]	d [mm]	A_s [mm^2]	f_{cc} [MPa]	f_{sy} [MPa]	f_{su} [MPa]	γ [-]	ω_s [-]	ε_s [%]
(2000)	PLS 1	1500	300	150	126	101	28.1	500	575	1.15	0.047	3.2
	PLS 2	1500	300	150	126	101	28.1	500	575	1.15	0.047	3.2
	PLS 3	1500	300	150	126	101	28.1	500	575	1.15	0.047	3.0
	PLS 4	1500	300	150	126	101	28.1	570	660	1.16	0.054	3.1
	PLS 5	1500	300	150	126	101	28.1	570	660	1.16	0.054	3.4
	PLS 6	1500	300	150	126	101	28.1	570	660	1.16	0.054	3.6
(2003a)	PLS 2	1500	300	150	124	113	35.1	516	624	1.21	0.045	3.7
	PLS 3	1500	300	150	126	101	39.9	514	653	1.27	0.034	4.4
	PLS 4	1500	300	150	126	101	83.6	514	653	1.27	0.016	5.0
(2005)	PLS 1a	1500	530	150	122	201	45.0	534	643	1.20	0.037	1.0
	PLS 1b	1500	530	150	122	201	40.3	534	643	1.20	0.041	0.8
	PLS 1c	1500	530	150	122	201	37.9	534	643	1.20	0.044	1.6
	PLS 3a	1500	400	150	122	201	45.0	534	643	1.20	0.049	1.5
	PLS 3b	1500	400	150	122	201	40.3	534	643	1.20	0.055	1.9
	PLS 3c	1500	400	150	122	201	37.9	534	643	1.20	0.058	1.6
	PLS 4a	1500	320	150	122	201	45.0	534	643	1.20	0.061	3.2
	PLS 4b	1500	320	150	122	201	40.3	534	643	1.20	0.068	3.2
	PLS 4c	1500	320	150	122	201	37.9	534	643	1.20	0.073	1.6

[1)] Ansell & Svedbjörk

5 Experimental procedure

5.1 General description

Reinforced concrete beams were manufactured and tested to study the parameters that effects the average reinforcement strain and plastic deformation capacity. Nine concrete beams were constructed as well as one test beam. The length of the beams were equal to 2.8 m and a cross-sectional height and width of 200 mm, see Figure 5.1. The beams were reinforced with two steel reinforcement bars with a nominal diameter of 10 mm or 12 mm, respectively. In order to eliminate the influence of top reinforcement and stirrups on plastic deformation capacity, the bars are just placed at the bottom layer of the beams. After casting and curing, the beams were subjected to a four-point bending test until failure. The manufacturing of the beams and performing of tests were conducted in the Structural engineering laboratory at Chalmers University of Technology. A more detailed description of the preparations can be found in Appendix A.

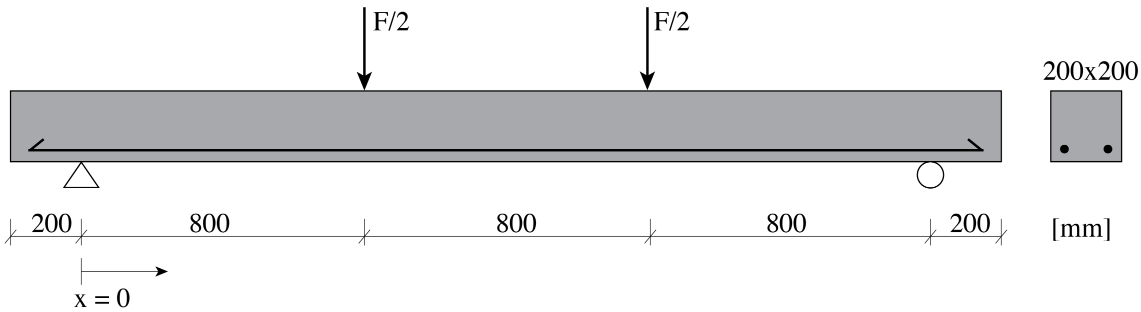

Figure 5.1 Reinforced concrete beam geometry and cross section.

5.2 Manufacturing of concrete beams

As mentioned, in total ten beams were manufactured and tested of which one beam was a test beam. Three different beam types were constructed, see Table 5.1. All three beam types had the same dimensions but different reinforcement amount, $\phi10$ or $\phi12$ and one beam type with the $\phi12$ reinforcement had low-friction PVC tubing. The test beam, beam number 10, was made by the research engineer to be used as a test beam or an additional beam for unpredicted situation. However, the $\phi10$ reinforcement bars in beam number 10 were unmarked and could not be used for strain measurements and the reinforcement quality was unknown.

Table 5.1 Naming of beams based on used reinforcement type and PVC tubes.

Name	Bar diameter	Bar label	Configuration
Beam 1	10	A,B	No PVC
Beam 2	10	A,B	No PVC
Beam 3	10	A,B	No PVC
Beam 10[1]	10	A,B	No PVC
Beam 4	12	A,B	No PVC
Beam 5	12	A,B	No PVC
Beam 6	12	A,B	No PVC
Beam 7	12	A,B	4x100 PVC
Beam 8	12	A,B	4x100 PVC
Beam 9	12	A,B	4x100 PVC

[1] Additional test beam.

5.2.1 Preparations before casting

The preparation started with cutting the reinforcement bars in length of 2.79 m to fit the beams and cut 6 samples from each bar diameter for tensile strength testing. To be able to measure the elongation of the reinforcement and calculate the plastic reinforcement strain all bars were marked each 50 mm using a hammer and an awl. Also, the middle one meter of the bars was marked using zip ties.

From each type of beam, two bars were scanned with 3D scanning tools to make a 3D model of the reinforcement bar. The bars for beams 1, 4 and 7 were scanned both before casting and after testing as another tool to measure the elongation and estimate the plastic strains. The 3D models were also used to analyse the change of cross sectional-area due to yielding.

After 3D scanning, PVC tube segments with length of 100 mm and spacing 200 mm were glued at the 1 m length in the middle of the reinforcement bars of the beams with plastic tubes, see Figure 5.2. The intention with the plastic tubes was to reduce the interaction and the transfer of bond stresses between the reinforcement and the concrete to increase the plastic deformation capacity of the beam.

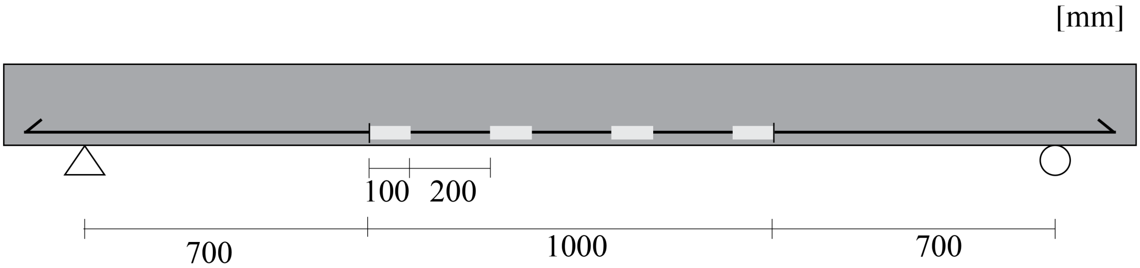

Figure 5.2 Configuration of the PVC tubes.

Before the reinforcement was placed inside the moulds, the moulds were oiled to facilitate the cleaning afterwards. Spacers were nailed inside the forms to have concrete cover equal to 35 mm, see Figure 5.3.

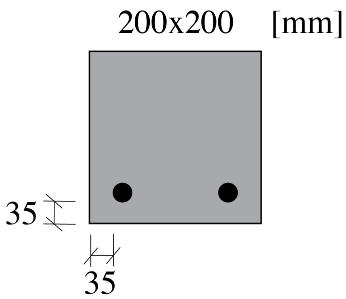

Figure 5.3 Geometry of the cross section and concrete cover.

5.2.2 Casting

Concrete with the strength class C40/50 was ordered and delivered to the site by a concrete mixing truck and the fresh concrete was poured from the truck into the forms. Concrete cubes for material testing were also casted to use for compressive strength tests and wedge-splitting tests (WST). A vibrator was used to eliminate air in the concrete. The beams were watered before covered by a plastic sheet to harden and the cubes were submerged in water until the material testing.

After demoulding, the beams were prepared for the digital image correlation (DIC). A DIC camera was used during the beam test to document the development of cracks and the deformation of the beam. The software require a high contrast pattern and therefore the side towards the camera was painted with a white backdrop. After drying, a black speckle pattern was added to the white backdrop with a brush.

5.2.3 After testing

In order to measure the plastic strain of the reinforcement, the bars was removed from the concrete beams after testing. A cut was sawn along each reinforcement bar and a sledgehammer was used to remove the concrete. A schematic illustration of the cutting process is shown in Figure 5.4.

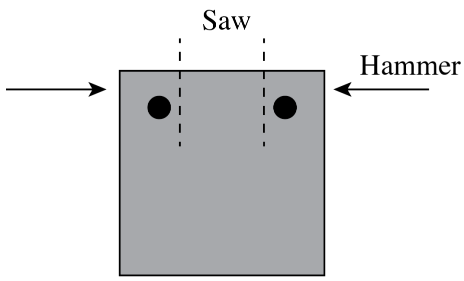

Figure 5.4 A schematic illustration of the process to remove the reinforcement bars from the concrete. The dashed lines represent the position of the saw cuts and the arrows hit with the sledgehammer.

After the reinforcement was removed from the concrete the elongation of the bars was measured by measuring the distance between the marks on the reinforcement bars. The 3D scanned bars was scanned again and the concrete residuals was removed prior to the 3D scanning by sandblasting the bars. To fit the bars into the sandblasting machine, the middle one meter was cut with 100 mm margin at each side. Also, reinforcement specimens was cut at each end of the reinforcement bars to be used for a second reinforcement tensile strength test.

5.3 Beam test setup

The load rig was prepared for a four-point bending test with two point loads. Between the two point loads, a tensile zone with constant moment can be distinguished and it is within this tensile zone, the first cracks were expected to appear, see Figure 5.5.

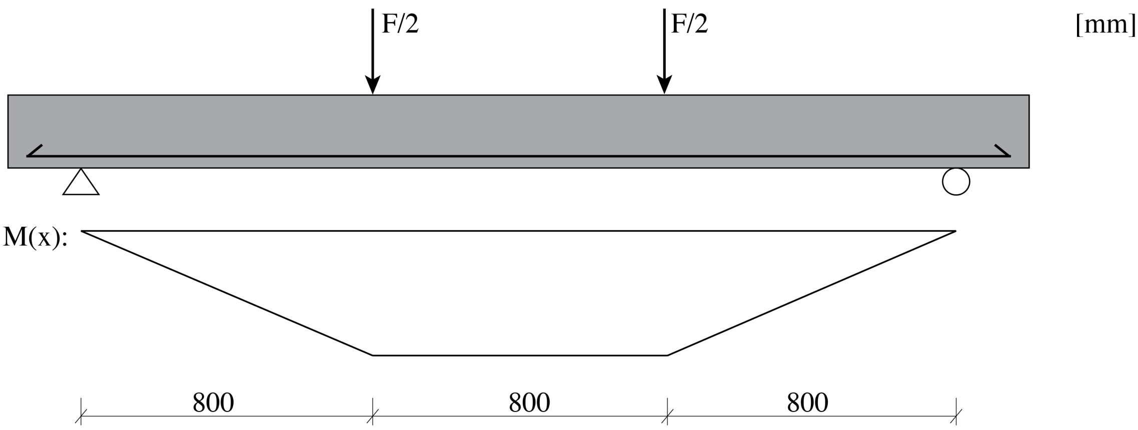

Figure 5.5 Schematic illustration of the moment distribution.

The loading was deformation controlled by a hydraulic jack connected to the steel loading beam with two roller supports. Steel plates and thin wooden plates were placed between the roller supports and the concrete beam. The beam was placed on a pinned support to the left and a roller support to the right, the test setup is presented in Figure 5.6. A load cell and a displacement sensor were connected to the hydraulic jack to measure applied load and midspan deflection. At the beginning of the loading session, the beam was loaded with an initial load equal to 8 kN and then unloaded to 2 kN to avoid effect of settlements in the load-deformation results. After the unloading, the loading continued according to the predetermined loading rate until failure. The loading was stopped when the applied load decreased drastically due to rupture of reinforcement or crushing of concrete. Also, for some beams the test was stopped before failure because the loading device got in contact with the beam.

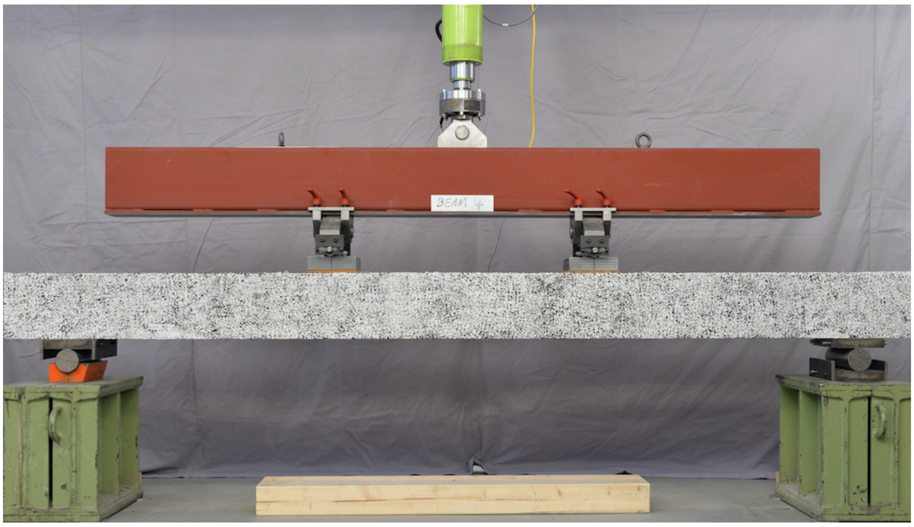

Figure 5.6 Test setup. Example from beam number 4.

The measuring sequence had a limited number of captured images and to prevent a restart of the program during a test, adjustment of the load rates was done during testing. The loading was divided into two phases, the first phase with a lower speed to capture the changes in the force-displacement curve more carefully and allow for a slower crack development. The second phase, with a higher load rate, was initiated at a certain deformation which are presented together with the load rates for each beam in Table 5.2.

Table 5.2 Adjustments of the loading rates.

Beam	Load rate	Deformation
1, 5	1 mm/min 4 mm/min	< 10 mm
8	2 mm/min 4 mm/min	< 20 mm
2, 3, 4, 6, 7, 9, 10	2 mm/min 5 mm/min	< 20 mm

As mentioned in the description of the beam test setup, loading plates were placed under the point loads. For beams 1, 5 and 8 the size of the loading plates was equal to 100x200 mm. To increased the capacity and prevent eccentricity of the loading points due to movements of the concrete beam, the size of the plates was increase to 200x200 mm. An illustration of the eccentricity problem due to movements of the beam is shown in Figure 5.7.

Figure 5.7 Eccentricity of loading point for beam 8 with small loading plate.

5.4 Digital image correlation

DIC is a non-interferometric method and is as a powerful analysis tool used for experimental measurements and the method has been used to capture the behaviour of the beam under loading. Two cameras were used to record data that resulted in 3D models and strain fields of the beam surface. The cameras use the white and black speckle pattern to analyse the deformation of the painted surface during testing. The cameras recorded the data from the 1 m in the middle of the beams, see Figure 5.8.

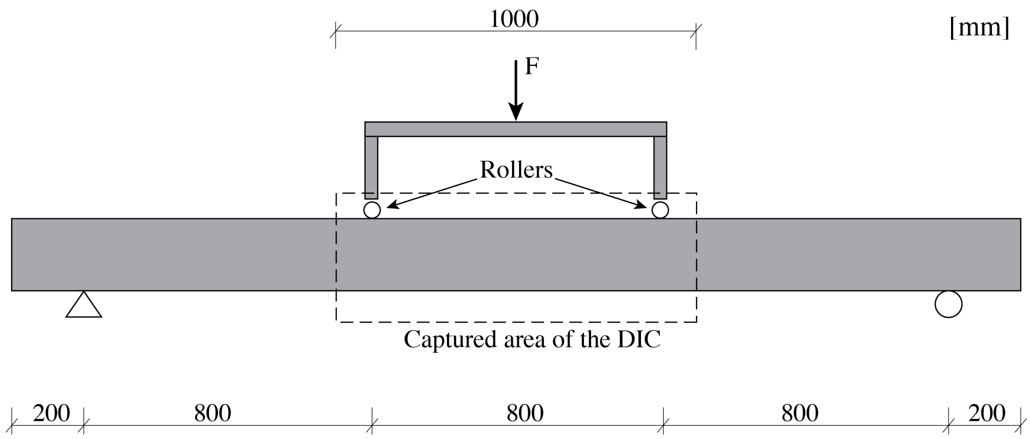

Figure 5.8 Area captured by the DIC camera.

The frequency of the DIC camera was set to 0.5 Hz which implies that one picture is captures every two seconds. However, the frequency was changed for beam 6, 7 and 9 where the first 600 s had the frequency 0.5 Hz and between 600 s and 1656 s the frequency was set to 0.25 Hz and the remaining running time, the frequency was again 0.5 Hz. The adjustment of the camera frequency was due to a limitation of total number of pictures that can be captured with the DIC camera before a restart of the sequence is needed. The frames captured by the DIC cameras were processed in the software GOM Correlate to analyse the deformation and crack development of the beam during testing.

6 Predictions

6.1 Introduction

Predictions of the load capacity were made to estimate the ultimate load and the load at yielding. The material properties used for the calculations are results from the material testing presented in Section 7.2. The concrete compressive strength was approximated by interpolating the results from the compressive strength tests preformed at 28 days and at 40 days after casting to estimate to the strength at 33 days. The average values from the material testing have been used in the calculations, see Table 7.1 for concrete compressive strength and Table 7.3 for reinforcement properties. The method used to estimated the load capacity is based on the procedures presented in (Al-Emrani et al., 2011) and (Al-Emrani et al., 2013).

6.1.1 Ultimate load capacity

The ultimate load was determined using the stress block method. The ultimate concrete strength is assumed to be reached and is equal to $\varepsilon_{cu} = 3.5‰$ and the reinforcement is yielding. A linear strain distribution and a parabolic relation of stress distribution in the compressive zone are also assumed, see Figure 6.1.

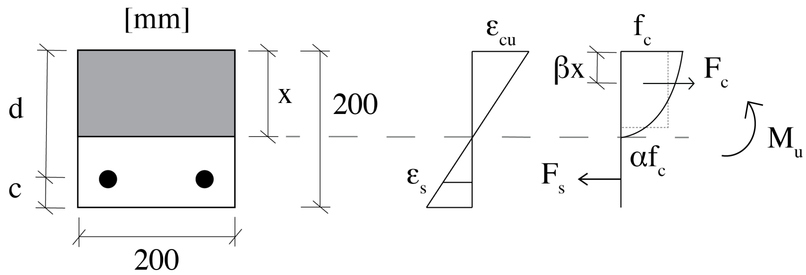

Figure 6.1 Schematic illustration of the stress block method to determine the ultimate moment capacity.

Equilibrium condition:
$$\alpha \cdot f_c \cdot b \cdot x = f_{sy} \cdot A_s \tag{6.1}$$

Ultimate moment:
$$M_u = \alpha \cdot f_c \cdot b \cdot x(d - \beta \cdot x_u) \tag{6.2}$$

Equation (6.1) was used to calculate the height of the compressive zone, x_u and then inserted in Equation (6.2) to calculate the ultimate bending moment. The coefficients α and β is called stress block factors and are stated in (Al-Emrani et al., 2013) and have the values

$$\alpha = 0.810 \tag{6.3}$$

$$\beta = 0.416 \tag{6.4}$$

To consider the dead weight of the beam, the ultimate moment was reduced by the moment due to dead weight to calculate the remaining moment capacity that the beam can carry in the ultimate limit state

$$M_q = M_u - M_g = M_u - \frac{g \cdot l^2}{8} \tag{6.5}$$

The corresponding load can be calculated by dividing the reduced moment by the distance a, which is the length from the support to the point load equal to L/3 then multiply the expression with two to obtain the total load from the two point loads, see Equation (6.6). The estimated ultimate moment including dead weight and load capacity is presented in Table 6.1.

$$F_{tot,q} = 2 \cdot \frac{M_q}{a} \tag{6.6}$$

Table 6.1 Predicted ultimate load capacities when dead weight is considered, for beams with reinforcement ϕ10 and ϕ12, respectively.

Beam	Ultimate moment, M_q [kNm]	Ultimate applied load, $F_{tot,q}$ [kN]
ϕ10	13.6	34.0
ϕ12	18.6	46.6

6.1.2 Load at yielding

The stress block method was also used to calculate the capacity at yielding. The calculations are similar to the calculations at the ultimate limit state but with a triangular stress block, see Figure 6.2.

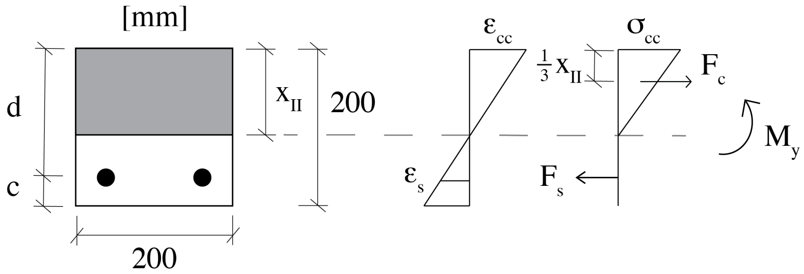

Figure 6.2 Schematic illustration of the triangular stress block to determine the yielding moment.

The height of the compressive zone, x_{II} is determined for the cross section in state II where α is the ratio between the modulus of elasticity of the reinforcement and concrete.

$$b \cdot x_{II} \cdot \frac{x_{II}}{2} = \alpha \cdot A_s(d - x_{II}) \tag{6.7}$$

Equilibrium condition:

$$\frac{\sigma_{cc}}{2} \cdot b \cdot x_{II} = \sigma_s \cdot A_s \tag{6.8}$$

The stress in the concrete at yielding is unknown and the stress in the steel is equal to the yielding strength f_y. The yielding moment is calculated with moment equilibrium around the concrete compressive resultant and then reduced by the dead weight moment, see Equation (6.9). The corresponding load capacity at yielding is calculated according to Equation (6.6) and the results are presented in Table 6.2.

$$M_y = \sigma_s \cdot A_s(d - \frac{x_{II}}{3}) - M_g \tag{6.9}$$

Table 6.2 Predicted yielding moment and yielding load when dead weight is considered, for beams with reinforcement $\phi 10$ and $\phi 12$, respectively.

Beam	Yield moment, M_y [kNm]	Yield load, $F_{tot,y}$ [kN]
$\phi 10$	13.0	32.4
$\phi 12$	17.7	44.4

7 Experimental results

7.1 General description

The results from the material testing, bending tests, strain measurements and determination of plastic rotation capacity are presented within this chapter. Firstly, the material testing of the concrete and reinforcement are treated in order to get necessarily background information of the materials. Then the results from the bending tests are presented in terms of structural response under loading and crack formation. Also, beam results with respect to plastic reinforcement strain from measurements and 3D scanning are presented. At last, determination of plastic rotation capacity and a summary of the concrete beam results are included.

7.2 Material testing

To obtain necessary background information about the materials, testing of both plain concrete and steel reinforcement was performed. Compressive strength tests and wedge-splitting test (WST) were performed to determine the concrete properties and tensile tests of the reinforcement were performed twice, both before and after beam testing to determine the steel properties.

7.2.1 Concrete

Compressive strength test and wedge-splitting test were performed on the concrete in order to obtain material properties. Therefore, three concrete cubes were subjected to compressive test at 28 days after casting. Also, the test was repeated for three concrete cubes at the age of 40 days. Wedge-Splitting test was performed on three cubic specimens to reach the fracture energy of concrete. The detailed test results are provided in Appendix B and the results from the compressive tests in presented in Table 7.1 where the cylindrical compressive strength was approximated using Equation (2.1) and the result from the WST in Table 7.2.

Table 7.1 Average compressive strength.

Test type	Cube strength [MPa]	Cylinder strength [MPa]
28-days compressive strength	64.8	54.0
40-days compressive strength	70.4	58.7

Table 7.2 Average values from the WST results.

Accumulated G_F [Nm/m^2]	Maximum splitting load F_{sp} [kN]	Maximum CMOD [mm]
151	5.79	2.13

7.2.2 Reinforcement

Six reinforcement specimens for each bar diameter was subjected to a tensile test to provide material properties. The stress-strain curves are plotted for respective reinforcement diameter in Figures 7.1 and 7.2 and a summary of the average material properties is presented in Table 7.3. Complete result from the twelve reinforcement specimens and more information about the tensile test setup are presented in Appendix B.

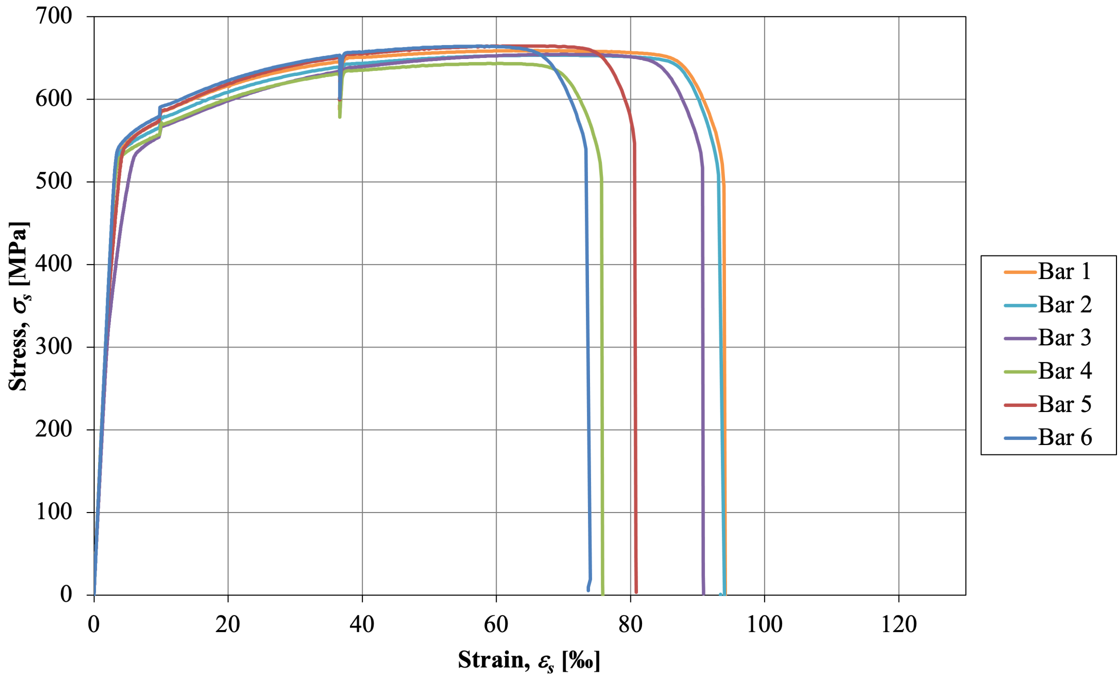

Figure 7.1 Stress-strain curves for six $\phi 10$ reinforcement specimens.

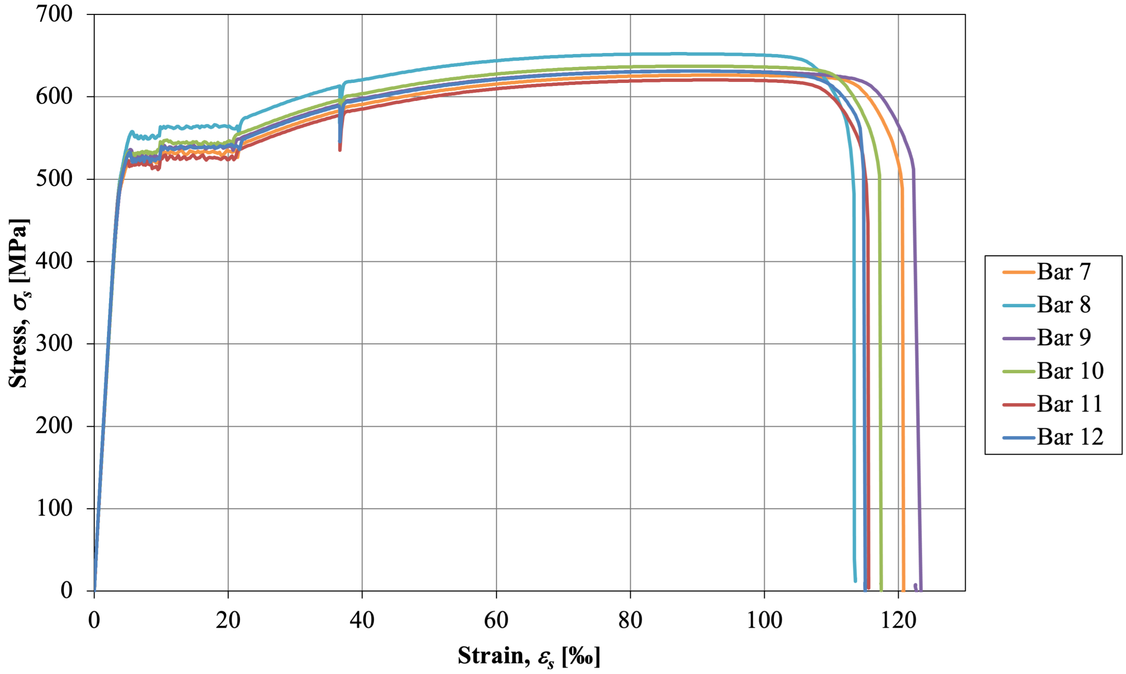

Figure 7.2 Stress-strain curves for six ϕ12 reinforcement specimens.

With results from the tensile tests, material data as modulus of elasticity, yielding strength, ultimate strength, tensile strain at maximum stress and the yield to ultimate tensile strength ratio were determined. The average properties for each respective reinforcement diameter are presented in Table 7.3.

Table 7.3 Average modulus of elasticity, strain at ultimate stress, yielding strength, ultimate tensile strength and f_y/f_u-ratio.

ϕ [mm]	E_s [GPa]	ε_{su} [‰]	f_y [MPa]	f_u [MPa]	f_y/f_u [-]
10	198	64	564	656	1.16
12	191	90	535	622	1.18

7.3 Beam results, structural response

In this section the results are presented from the four-point bending tests on ten reinforced concrete beams which were introduced in detail in Section 5.2.1. The results are illustrated and compared in form of load-displacement curves, displacement-width curves for cracks, displacement-time curves for loading points, and crack pattern figures.

The values in load-displacement curves are provided from hydraulic jack while the other values are provided from DIC results. In order to facilitate the comparison, the first part of load-displacement curves including initial loading and unloading are omitted and the curves are adjusted to have the same starting point.

Test results are presented and processed in three categories $\phi 10$ reinforcement, $\phi 12$ reinforcement, and $\phi 12$ reinforcement with PVC tubes. From each category, the load-displacement curve of all beams is provided in one graph. The displacement-width curves for cracks together with corresponding load-displacement curve and crack pattern figure for one beam is presented in the report representing the general structural behavior of each group. All other curves and figures can be found in Appendix C.

Symmetrical structural behavior and its effect on structural response is studied for each beam. It is observed that some beams have more symmetrical behavior such as beam 8 compered to beam 9 which has an unsymmetrical behaviour, see Figure 7.3. Displacement-time curve under each loading point and the point between loading points (see Figure C.11) are provided in these graphs. All relevant curves are provided in Appendix C.

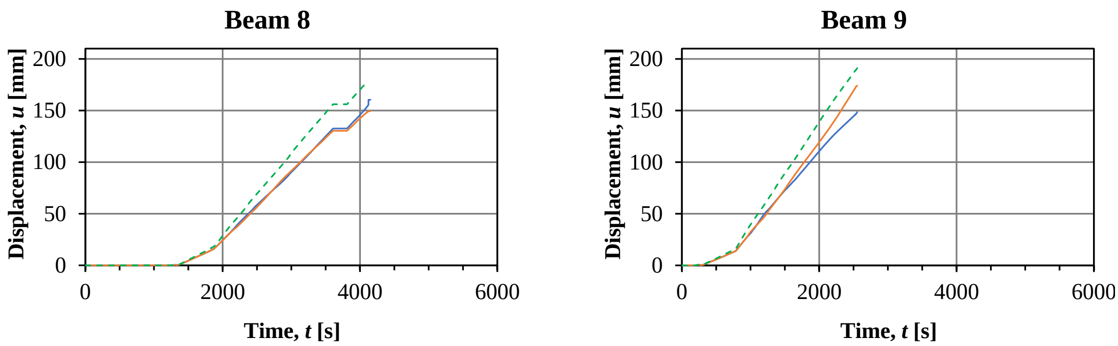

Figure 7.3 *Displacement-time curve under loading points and mid-point for beams 8 and 9 with $\phi 12$ reinforcement. The data for mid-point, point 1, and point 2 is shown by green dash-line, orange, and blue line, respectively (see Figure C.11).*

A table of results is also included for each category at which the force, maximum displacement, and displacement for maximum force values are obtained from hydraulic jack. Load level at which first crack appears, displacement of mid-point, number of cracks, average crack width, and total crack width values are provided from DIC results. Symmetrical behavior is also studied based on DIC results. The number of cracks are counted at yielding and cracks which are formed after yielding are not considered in measurements. The crack width was measured at the level of reinforcements and when the load reached the maximum value. All crack measurements are performed at the region with constant moment between loading points.

7.3.1 Beams with ϕ10 reinforcement

Beams 1, 2, 3, and 10 contain ϕ10 reinforcement bars. However, reinforcement bars in beam 10 are not identical to ϕ10 bars in other three beams. Also, beam 10 with a symmetrical behavior shows a higher deformation capacity under same four-point bending test and other three beams have a more similar behavior with smaller deformation capacity.

Beams 1, 2, and 3 failed due to rupture of reinforcement. Beam 10 did not reach failure and the test was stopped because of test setup limitations when the structure was close to failure and the load was not increasing anymore. Although there was a damage observed in concrete on the top surface of beam 10, the exact failure mode cannot be predicted for it.

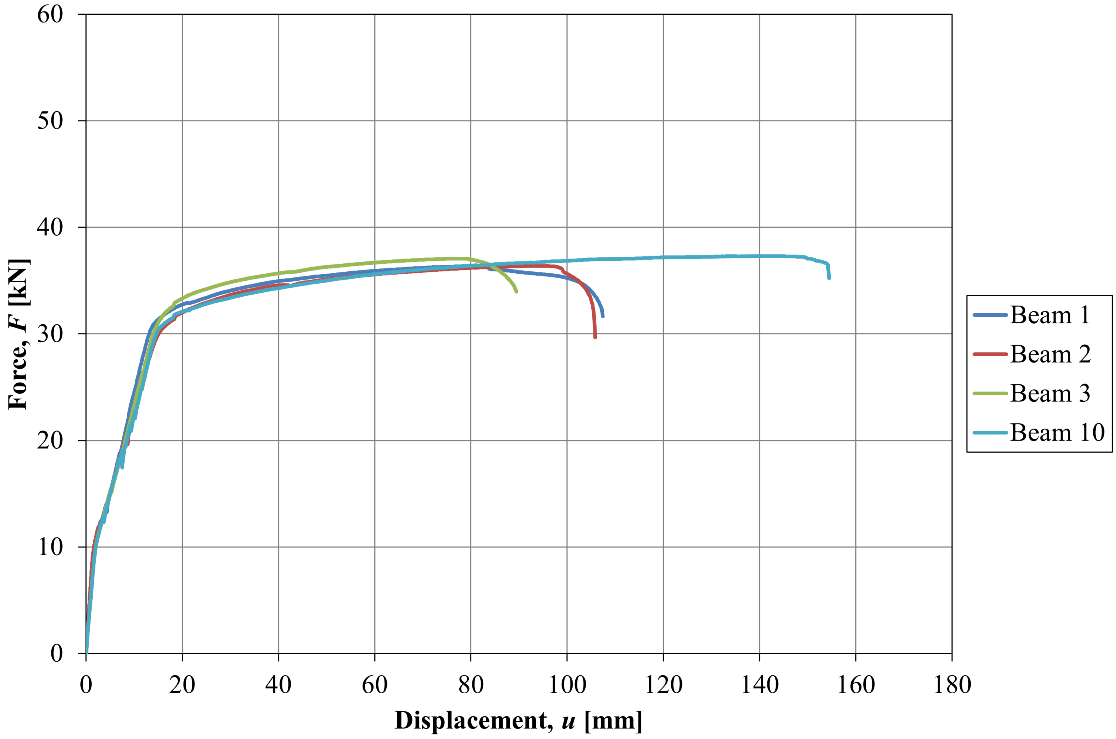

Figure 7.4 Load-displacement curves for beams with ϕ10 reinforcement.

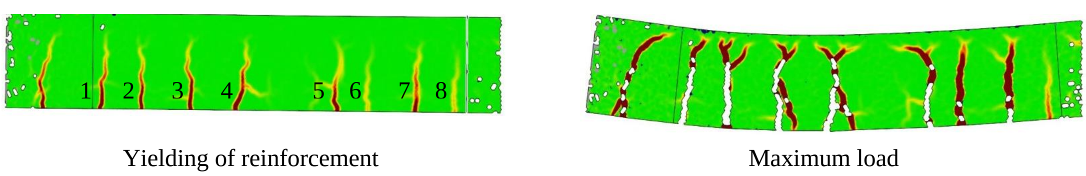

Figure 7.5 Crack pattern of beam 2 at yielding and maximum load.

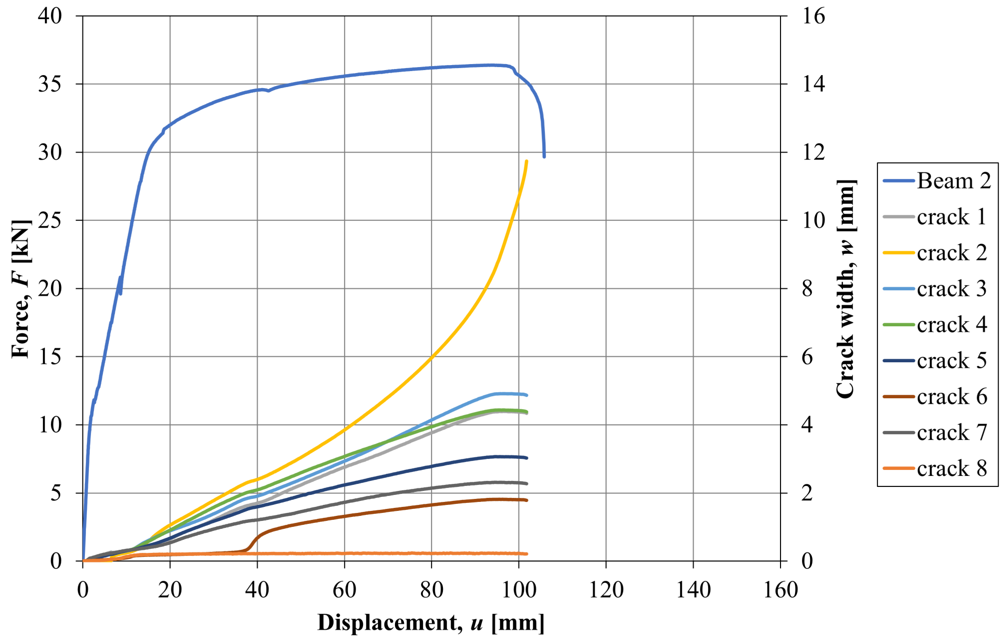

Figure 7.6 *Load-displacement curve of beam 2 and displacement-width curves for cracks.*

Table 7.4 *Summary of testing results for beams with ϕ10 reinforcement.*

Beam no.	1	2	3	10
F_{max} [kN]	36.4	36.4	37.1	37.3
F_{cr} [kN]	10.8	10.0	11.0	10.4
$u(F_{max})$ [mm]	81	93	78	141
u_{max} [mm]	107	106	89	155
u_{mid} [mm]	122	121	101	187
Failure[1]	R	R	R	-
Symmetrical behavior[2]	US	US	US	S
Number of cracks	7	8	6	7
Average crack width [mm]	3.2	3.5	2.7	6.1
Total width of cracks [mm]	22	28	16	43
Loading plate[3]	S	L	L	L

[1] "R", "C", and "-" stand for reinforcement rupture, concrete crushing, and not reaching failure, respectively.
[2] "S" and "US" stand for Symmetrical and asymmetrical behavior, respectively.
[3] "L" and "S" stand for large and small loading plate, respectively.

7.3.2 Beams with ϕ12 reinforcement

Beams 4, 5, and 6 contain ϕ12 reinforcement bars. Beams 4 and 5 show symmetrical behavior compared to beam 6 according to Appendix C.2. However, beam 4 shows a considerable higher deformation capacity. Also, beam 5 is tested with small loading plate which led to eccentricity of loading point.

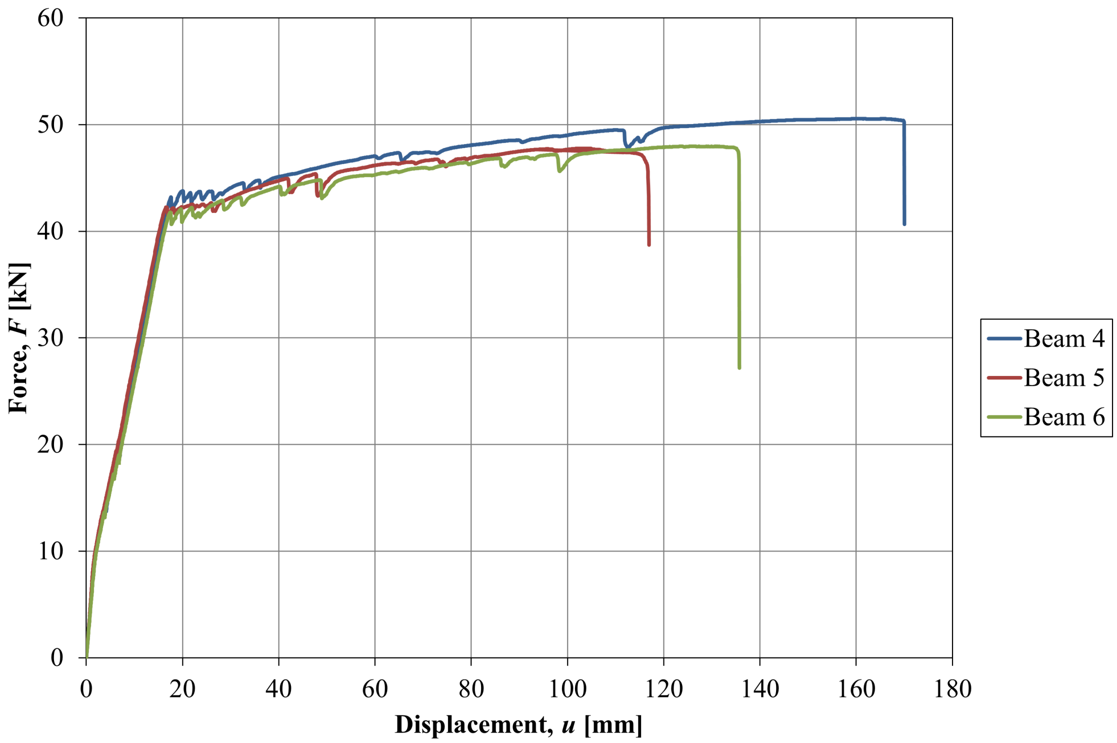

Figure 7.7 Load-displacement curves for beams with ϕ12 reinforcement.

All beams in this group failed due to concrete crushing and all obtained eight cracks between loading points at the stage of reinforcement yielding.

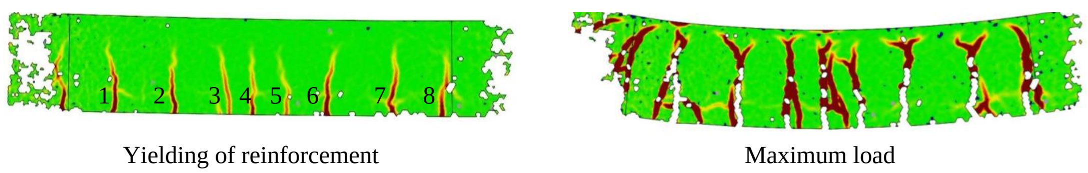

Figure 7.8 Crack pattern of beam 6 at yielding and maximum load.

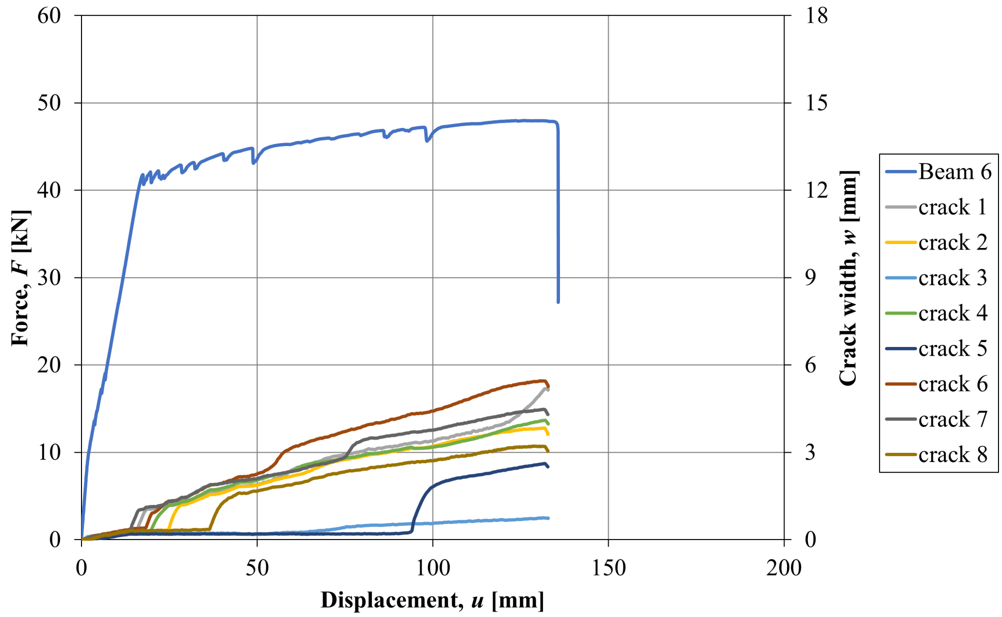

Figure 7.9 Load-displacement curve of beam 6 and displacement-width curves for cracks.

Table 7.5 Summary of testing results for beams with $\phi 12$ reinforcement.

Beam no.	4	5	6
F_{max} [kN]	50.6	47.8	48.0
F_{cr}[1] [kN]	-	10.5	10.5
$u(F_{max})$ [mm]	160	103	126
u_{max} [mm]	170	117	136
u_{mid} [mm]	197	133	159
Failure[2]	C	C	C
Symmetrical behavior[3]	S	S	US
Number of cracks	8	8	8
Average crack width [mm]	4.6	2.6	3.4
Total width of cracks [mm]	37	21	28
Loading plate[4]	L	S	L

[1] The data for beam 4 is missing due to delayed DIC recording.
[2] "R", "C", and "-" stand for reinforcement rupture, concrete crushing, and not reaching failure, respectively.
[3] "S" and "US" stand for Symmetrical and asymmetrical behavior, respectively.
[4] "L" and "S" stand for large and small loading plate, respectively.

7.3.3 Beams with ϕ12 reinforcement and PVC tubes

Beams 7, 8, and 9 contain ϕ12 reinforcement bars with PVC tubes. Beam 8 with small loading plates shows symmetrical behavior compared to beams 7 and 9 and it has the lowest deformation capacity in this group. Beams 7 and 9 did not reach failure as the beams got connected to the steel loading beam after deformation, see Figure 7.10, and it was not possible for the test to be continued. However, both beams were expected to be close to failure according to their load-displacement curves, see Figure 7.11.

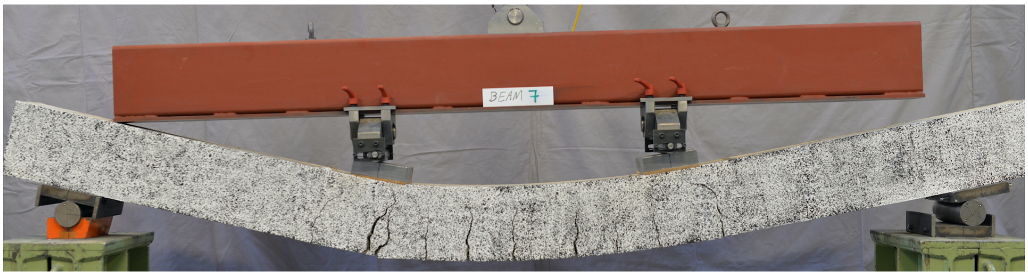

Figure 7.10 Connection of beam 7 and loading device before failure.

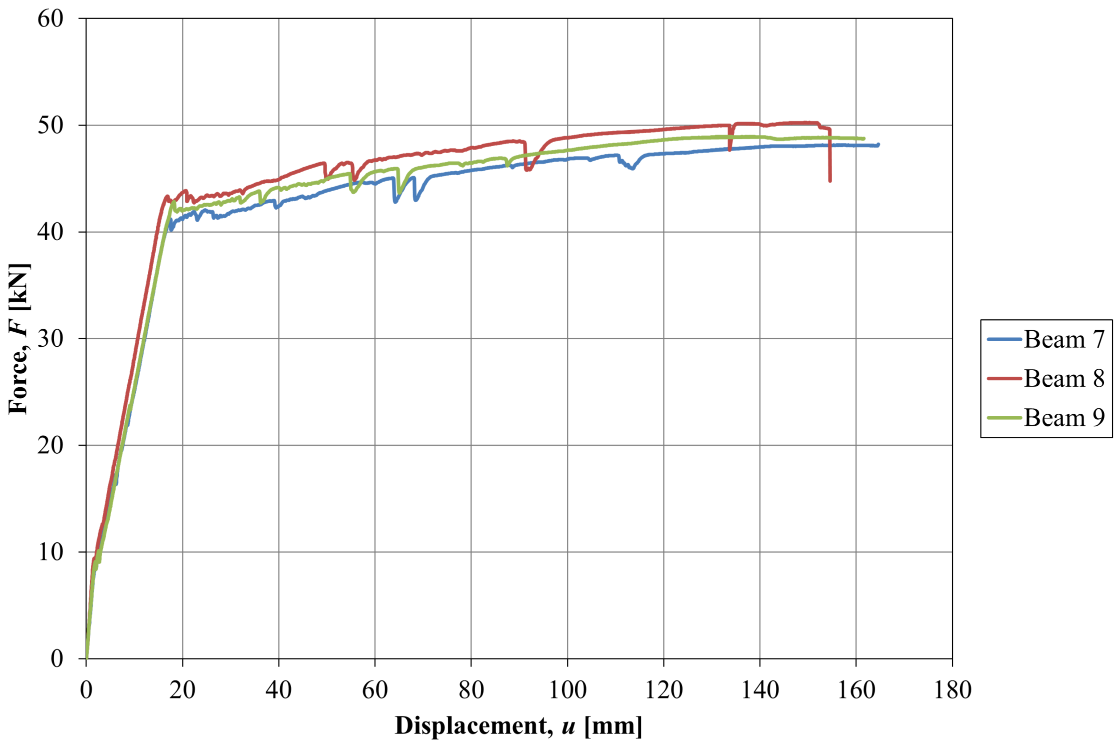

Figure 7.11 Load-displacement curves for beams with ϕ12 reinforcement and PVC tubes.

As for the ϕ12 beams without PVC tubes, concrete crushing was the cause of failure. All beams 7, 8, and 9 have seven cracks between loading points at the stage of reinforcement yielding.

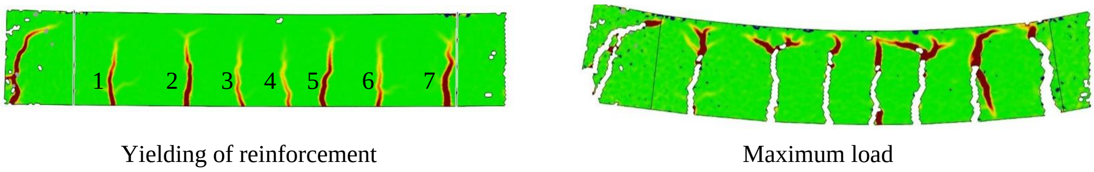

Figure 7.12   Crack pattern of beam 8 at yielding and maximum load.

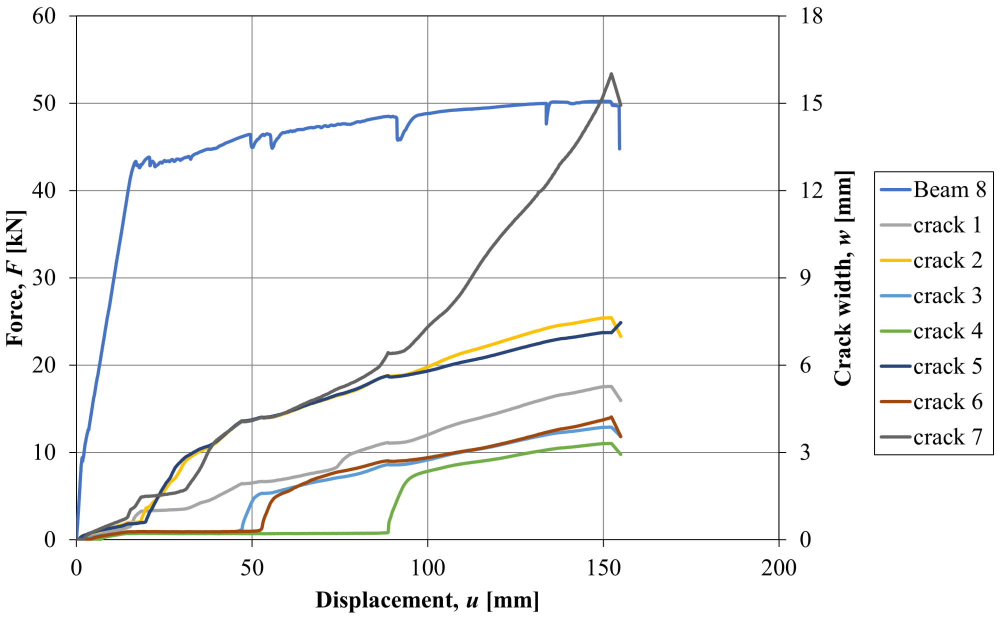

Figure 7.13   Load-displacement curve of beam 8 and displacement-width curves for cracks.

Table 7.6 Summary of testing results for beams with $\phi 12$ reinforcement and PVC tubes.

Beam no.	7	8	9
F_{max} [kN]	48.2	50.2	48.9
F_{cr} [kN]	8.0	9.3	8.7
$u(F_{max})$ [mm]	165	149	132
u_{max} [mm]	165	155	169
u_{mid} [mm]	186	179	191
Failure[1]	-	C	-
Symmetrical behavior[2]	US	S	US
Number of cracks	7	7	7
Average crack width [mm]	5.8	5.3	6.1
Total width of cracks [mm]	41	37	42
Loading plate[3]	L	S	L

[1] "R", "C", and "-" stand for reinforcement rupture, concrete crushing, and not reaching failure, respectively.
[2] "S" and "US" stand for Symmetrical and asymmetrical behavior, respectively.
[3] "L" and "S" stand for large and small loading plate, respectively.

7.4 Beam results, strain measurements

The results from the strain measurements are presented in bar charts for every 50 mm mark. Each figure includes strain measurements for each reinforcement bar and the average plastic strain for the two bars which corresponds to the average plastic reinforcement strain of the beam. The crack pattern figure from the DIC is also included to show the connection between the crack pattern and the plastic strain. The crack pattern figure is placed in relation to the average reinforcement strain of the beam in order to match the loading points.

Since the strains close to the ends of the beam are equal to zero, the presented results are limited to the coordinates 600 mm to 1800 mm. The loading points are marked with a red circle and a rupture of the reinforcement is denoted with *. The result from the reinforcement tensile strength test shows that the average ultimate strain for the $\phi 10$ bars is limited to 64 ‰ and 90 ‰ for the $\phi 12$ bars, see Table 7.3. Therefore, in the calculations to determine an average strain, the individual strain value in a given section is also limited to 64 ‰ for $\phi 10$ bars and to 90 ‰ for $\phi 12$ bars, hence all strains above that limit is set to equal to 64 ‰ or 90 ‰ in the calculations. However, if the measured strain exceeds this value, the strain value is marked in a text box alongside the bar in the bar chart.

In the bar chart with the average reinforcement strain of the beam, the total average plastic strain, ε_{ave} is presented as a horizontal line. This value is calculated by taking the average of all strains within the region with measured strains. One example of the strain measurement result, from the reinforcement in beam 1 is presented in Figure 7.14. The results from the other beams are presented in Appendix D.

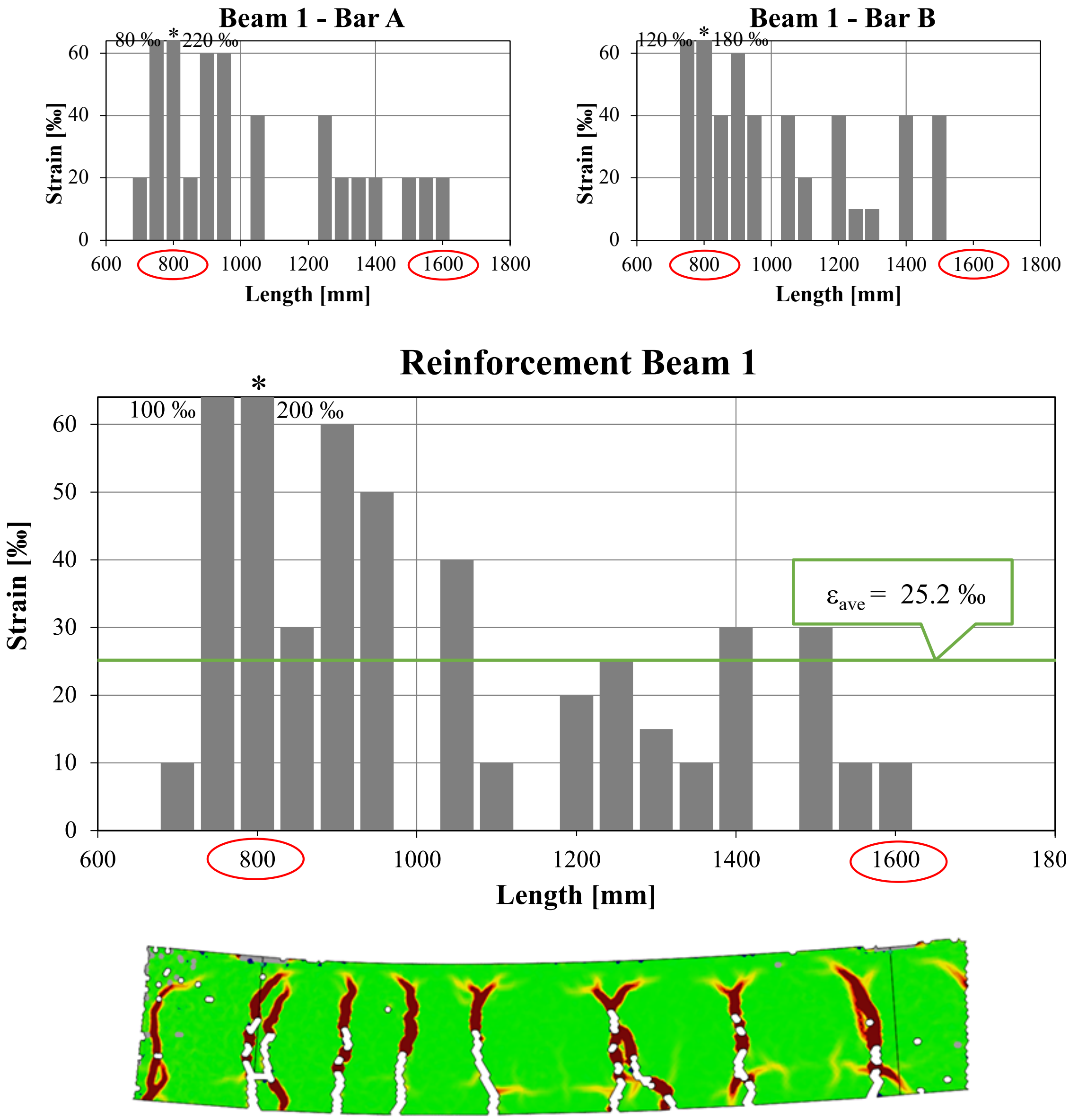

Figure 7.14 *Plastic reinforcement strain measurements for each reinforcement bar (upper charts), the average strain of the two bars (middle chart) and the crack pattern figure from DIC for beam 1.*

A summary of the average plastic reinforcement strain results is presented in Table 7.7 and as average values of each beam type in Table 7.8 and Table 7.9. Due to asymmetric loading of some of the beams, the average plastic strain is also calculated to the left and to the right side of the middle. If the reinforcement ruptured, the measured strain is marked with *, both for the full beam and to the left or right side of the middle depending on where the rupture was located.

The average plastic reinforcement strain was also calculated without the limit of 64 ‰ or 90 ‰, presented in parentheses. The results show that it is mainly the $\phi 10$ bars that are effected by the strain limit since they had measured strains greater than the 64 ‰. The beams that are not effected by the limit and have the same average plastic strain with and without strain limits are not presented. Note that the average plastic strain within a ruptured area was approximated by assembly the two ruptured parts together to measure the elongation. Therefore, the measured plastic strain is an approximation of the distance between the to marks. Also note that the theoretical measured strain at rupture is included in the average strain calculation and the maximum measured plastic strain presented in Table 7.7 is without the strain limits.

Table 7.7 Average plastic reinforcement strain from measured elongation. The presented strains are the maximum average strain, the average value of the full beam and the average of the left and right part respectively. The average plastic strains in parentheses is calculated without the strain limits.

Beam no.	Maximum strain [‰]	Full beam [‰]	To the left [‰]	To the right [‰]
1	200*	25.2* (34.2)	31.6* (47.3)	16.7
2	200*	24.3* (30.5)	32.6* (43.1)	13.0
3	190*	19.2* (25.2)	21.8* (31.5)	15.6
4	110	43.3 (44.2)	40.0	47.5 (49.2)
5	75	30.9	26.7	32.7
6	80	37.6	40.8	34.4
7	80	42.1	51.9	30.8
8	80	42.2	36.5	49.1
9	90	39.2	50.8	26.2

* Ruptured bar.

Due to unsymmetrical loading, the measured strains for most of the beams were larger at one side. Therefore, the average strain for each beam type is presented in two different ways. In Table 7.8, the average strain is based on the result from the full beam from Table 7.7. Whilst in Table 7.9, the average strain of each beam type is based on the average strain to the left or to the right, where the highest strain at each side of the beams is used in the average strain calculation of the beam type. To compare the measured strains with the strain at ultimate stress from the material testing, the utilization rate is calculated by

$$\eta = \frac{\varepsilon_{ave}}{\varepsilon_u} \tag{7.1}$$

where ε_{ave} is equal to the average strain presented in Tables 7.8 and 7.9 and ε_u the strain at ultimate stress from the material testing presented in Table 7.3. The strain at ultimate stress was equal to 64 ‰ for the ϕ10 reinforcement and 90 ‰ for the ϕ12 reinforcement.

Table 7.8 A summary of the average reinforcement strain for each beam type, based on the average value from the full beam and the utilization rate with respect to the ultimate strain from material testing.

Beam type	Average strain [‰]	Utilization rate [%]
ϕ10	22.9* (30.0)	36
ϕ12	37.3 (37.6)	41
ϕ12 PVC	41.2	46

* Ruptured bar.

Table 7.9 A summary of the average reinforcement strain for each beam type, based on the average value to the left or to the right side and the utilization rate with respect to the ultimate strain from material testing.

Beam type	Average strain [‰]	Utilization rate [%]
ϕ10	28.7* (40.6)	45
ϕ12	40.3 (40.9)	45
ϕ12 PVC	50.6	56

* Ruptured bar.

7.4.1 3D scanning

The plastic strain results from the 3D scanning are presented in the same way as the plastic strain measurements. The plastic strain between coordinate 1650 mm and 1700 mm is missing due to an unfortunate placing of the zip-tie which made the 1700 mm mark invisible. Data that was missing from the scanning is illustrated with a red cross. For the reinforcement in beam 1, the resolution of the 3D model made the marks less visible at the second scanning and therefore some data went missing. One example of the 3D strain measurement result, from the reinforcement in beam 1 is presented in Figure 7.15. The results from the other beams are presented in Appendix D. Note that the same interval in the bar charts is used as for measurements made by hand even though the results from the 3D scanning were between the coordinate 700 mm to 1700 mm. From the strain measurement results from beam 1, bar B, see Figure 7.15 is can be seen that the strains between the coordinates 1200-1400 mm are somewhat higher compared to the results from the manually made measurements, see Figure 7.14.

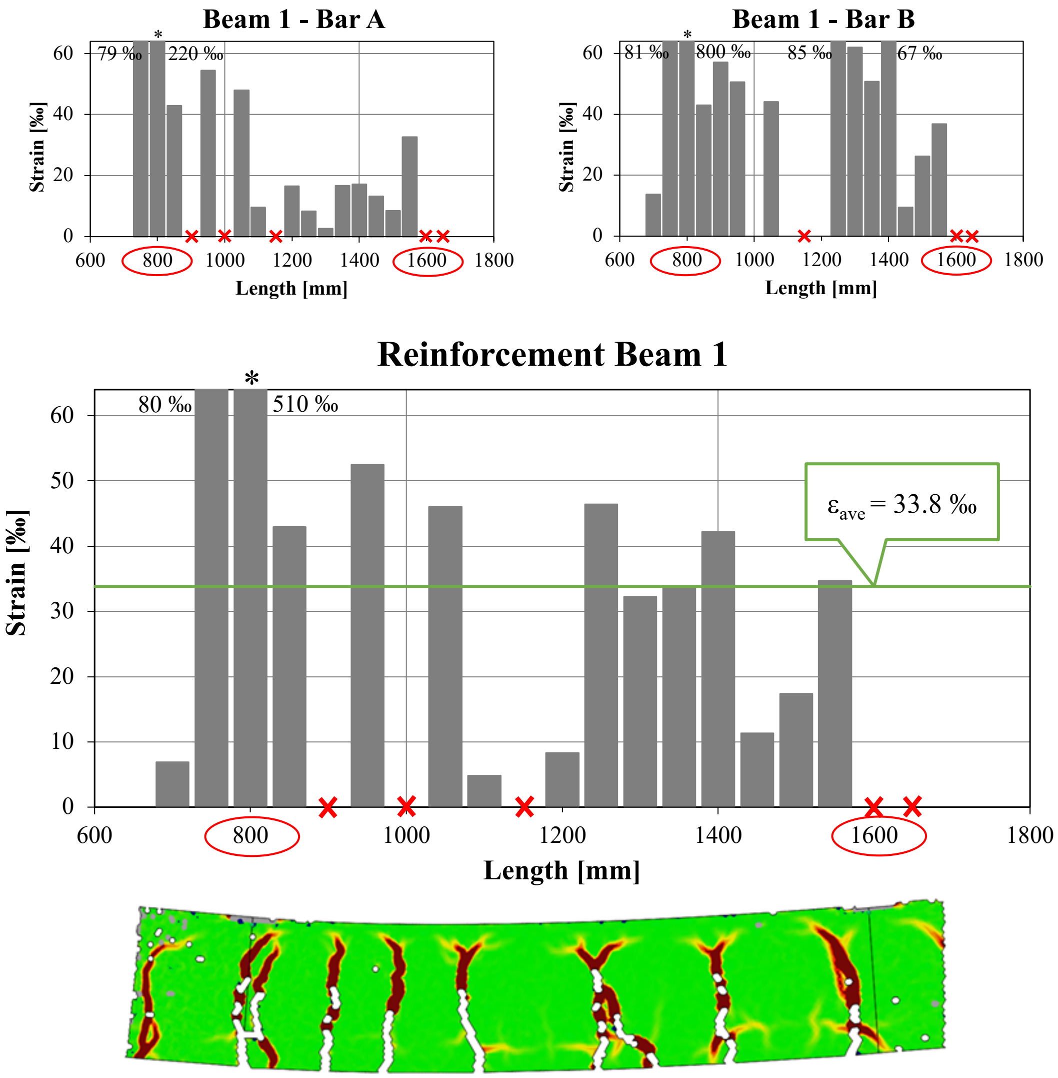

Figure 7.15 Plastic reinforcement strain from 3D scanning for each reinforcement bar (upper charts), the average strain of the two bars (middle chart) and the crack pattern figure from DIC for beam 1.

A summary of the plastic reinforcement strain results from 3D scanning is presented in Table 7.10. In the same way as in Table 7.7, the average plastic strain is also calculated to the left and to the right side of the middle to indicate asymmetric loading. Note that the theoretically measured strain at rupture is included in the calculations without strain limit, result presented in parenthesis. For beam 1, the difficulty in assembling the ruptured parts together resulted in a large elongation and therefore high measured strain.

Table 7.10 Average plastic reinforcement strain from 3D scanning. The presented strains are the average maximum strain value, average strain of the full beam and the average of the left and right part respectively.

Beam no.	Maximum strain [‰]	Full beam [‰]	To the left [‰]	To the right [‰]
1	510*	33.8* (64.6)	36.2* (93.3)	28.3
4	110	49.1	43.3	56.2
7	105	50.5 (52.0)	55.5 (58.2)	40.3

* Ruptured bar.

7.4.2 Comparison

The comparison of the plastic strain results from measurements and 3D scanning is done by comparing the average strain from the reinforcement bars in each beam and the results are presented in bar charts see Figures 7.16-7.18. Note that 1 mm difference in elongation results in strain difference equals to 20 ‰, which means that the difference in strain for a 50 mm long mark compare to a 51 mm long mark is equal to 20 ‰. The effect of the unexpected high strains from bar B in beam 1 can also be seen when comparing the two methods in Figure 7.16. A closer comparison of the strain between each mark is presented in Appendix D.

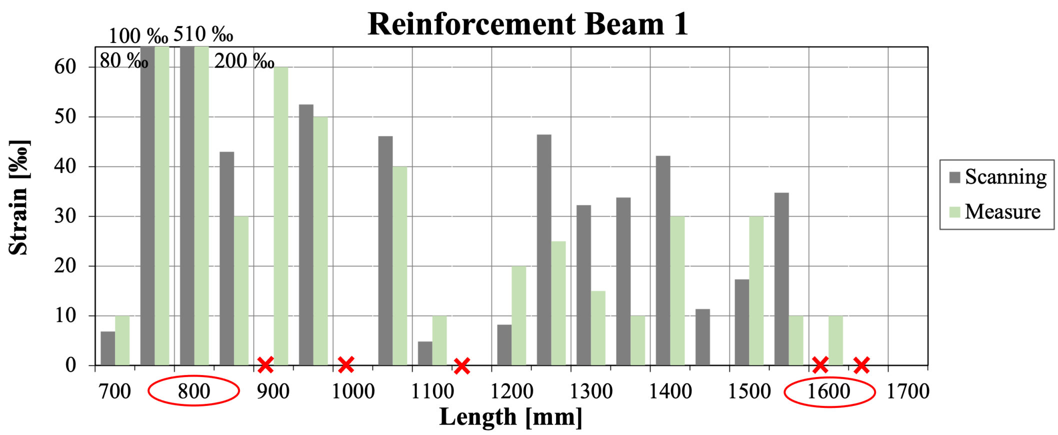

Figure 7.16 *Comparison of the plastic reinforcement strain results by 3D scanning and measurements for beam 1.*

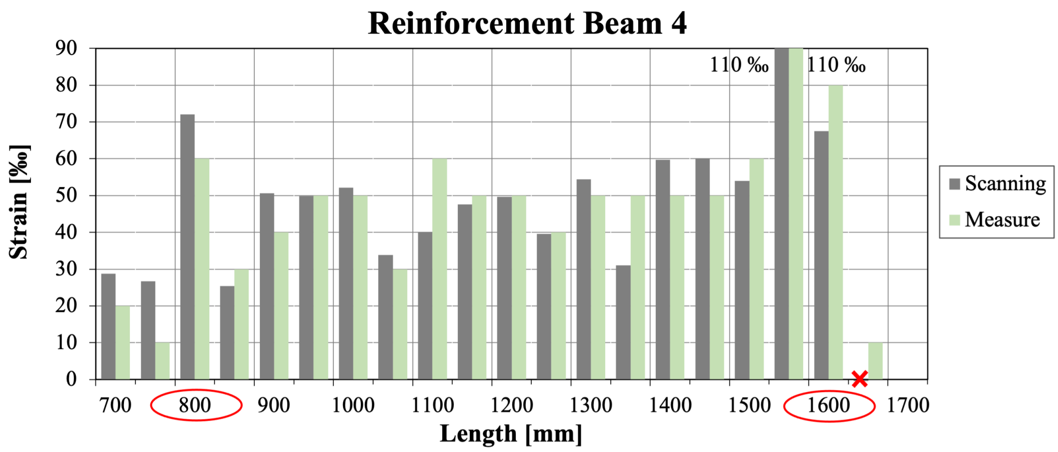

Figure 7.17 *Comparison of the plastic reinforcement strain results by 3D scanning and measurements for beam 4.*

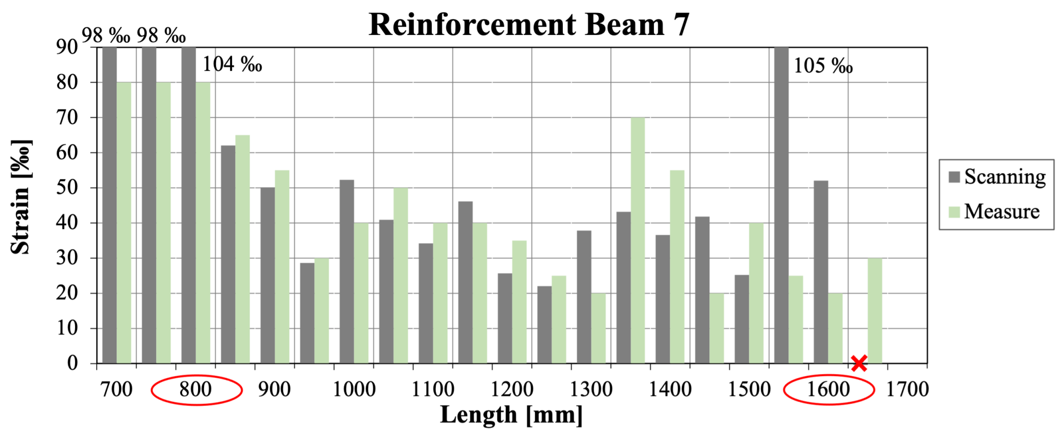

Figure 7.18 *Comparison of the plastic reinforcement strain results by 3D scanning and measurements for beam 7.*

In Table 7.11, a comparison of the average strain from the two methods is presented. The results considered the average strain between the coordinates 700 mm and 1700 mm and are based on the maximum measured strain to the left or to the right side for beams 1, 4 and 7.

Table 7.11 Comparison of the average strain results from 3D scanning and manually measurements.

Beam no.	3D scanning [‰]	Measurements [‰]
1	36.2*	31.6*
4	56.2	47.5
7	55.4	51.9

* Ruptured bar.

7.4.3 Cross-sectional area from 3D scanning

As mentioned in Section 5.2.1, the results from 3D scanning of reinforcement in beams 1, 4, and 7 before and after testing, are used to study the change of cross-sectional area due to yielding. For each bar the data are provided for the part with largest strain value. However, for bar B in beam 1 and bar B in beam 4 the data was missing for the part with largest strain and the comparison is therefore made for the part next to it with the second largest strain value. Figure 7.19 shows the cross-sectional area for a part from coordinate 800 mm to 850 mm in bar A of beam 1 and the considerable drop in the orange curve is due to rupture of reinforcement. The regular fluctuation of each curve is because of ribs along the bar. Other graphs are provided in Appendix D. Also, the reduction of area is calculated at three sections for each part: at the beginning, middle, and the end and is presented at Table 7.12.

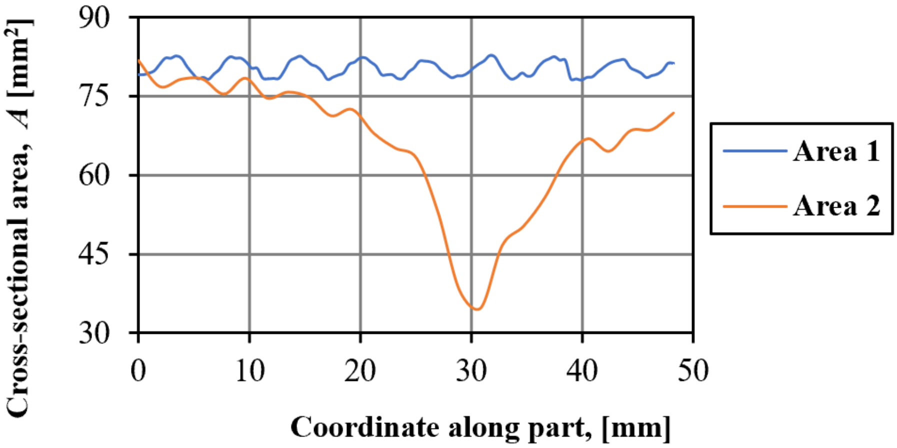

Figure 7.19 *Cross-sectional area of bar A from beam 1 for the part with coordinate from 800 mm to 850 mm, before and after testing.*

Table 7.12 *Cross-sectional area and comparison before and after testing for 3 sections at a part with largest strain value from each bar of beams 1, 4, and 7.*

Part	Area 1 [mm²]			Area 2 [mm²]			Reduction [%]		
	S1	S2	S3	S1	S2	S3	S1	S2	S3
Beam 1-A (800-850)*	80.1	79.7	78.6	78.5	72.5	55.8	2	8.9	28.9
Beam 1-B (750-800)	80.6	78.1	80.1	70.6	76.9	79.9	12.5	1.6	0.3
Beam 4-A (1550-1600)	114.1	112	113.8	100.6	98.67	98.3	11.8	11.9	13.6
Beam 4-B (1500-1550)	111.4	114	111.7	108.9	107.9	101.1	2.2	5.4	9.5
Beam 7-A (800-850)	112.1	114.4	11.6	101.9	102	101.2	9.1	10.8	9.3
Beam 7-A (800-850)	113.5	110.7	112.1	103.4	101.2	102.2	8.9	8.6	8.8

* Ruptured bar.

7.5 Determination of plastic rotation capacity

Plastic rotation capacity is calculated from test results for each beam corresponding to F_{max} which is the maximum load and 95% of F_{max}, using the method in Section 3.3.1 and Equation (3.14). Plastic deformation is estimated from load-displacement curve as shown in Figure 7.20. Notations u_{el} and u_u represent elastic and ultimate displacement for a certain load, respectively. The results for plastic rotational capacities are provided in Table 7.13. The stiffness value at state II is derived using a calculation software as 2.7 kN/mm for beams with ϕ10 and 3.6 kN/mm for beams with ϕ12.

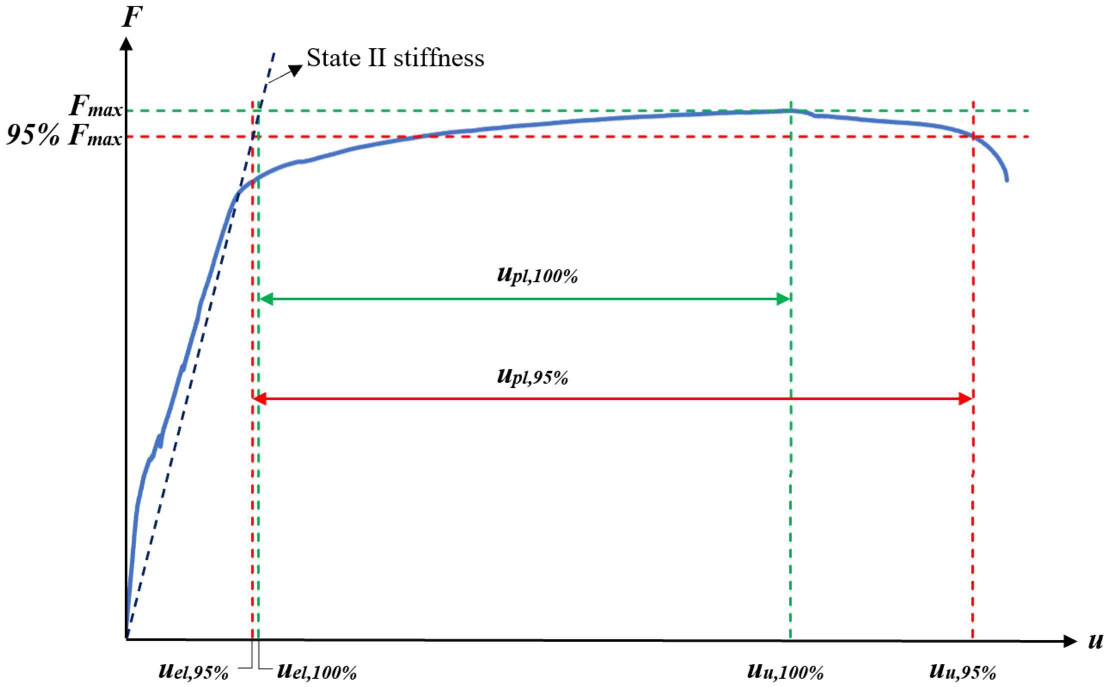

Figure 7.20 Calculation of plastic displacement from load-displacement curve.

Table 7.13 Values of plastic rotation capacity for all tested beams corresponding to F_{max} and $95\%F_{max}$.

Beam no.	$\theta_{pl,95\%}$ [mrad]	$\theta_{pl,100\%}$ [mrad]
1	109	82
2	107	93
3	89	76
10	171	152
4	188	175
5	124	106
6	146	133
7	182	180
8	170	162
9	177	139

Plastic rotational capacity for all beams has a larger value being calculated based on 95% of maximum load. For beams 7 and 9 the value of $\theta_{pl,95\%}$ is even expected to be larger as these beams have not failed and $u_{u,95\%}$ reaches a larger value if beam fails.

Although the equations from BK 25 and German Method which are provided in Sections 3.3.4 and 3.3.2 are based on different loading conditions, they are used to calculate plastic rotational capacity to compare with the values from test results. Detailed calculations are presented in Appendix C. Bk 25 calculates θ_{pl} for a beam subjected to uniformly distributed load while German method considers concentrated point load in the middle of beam. Comparing the values of plastic rotational capacity from results of four-point bending test in Table 7.13 with results from BK 25 and German method in Table 7.14, it is observed that the structural behavior is more similar to uniformly distributed loading condition and in this case using the results from German method leads to underestimation of θ_{pl}. As the provided solution in Eurocode 2 is based on German method, it also can be said that Eurocode 2 underestimates θ_{pl} for the loading condition used in this project.

Table 7.14 Values of θ_{pl} from BK 25 and German method.

Bar size	$\theta_{pl,German}$ [mrad]	$\theta_{pl,BK25}$ [mrad]
ϕ10	16	68
ϕ12	22	143

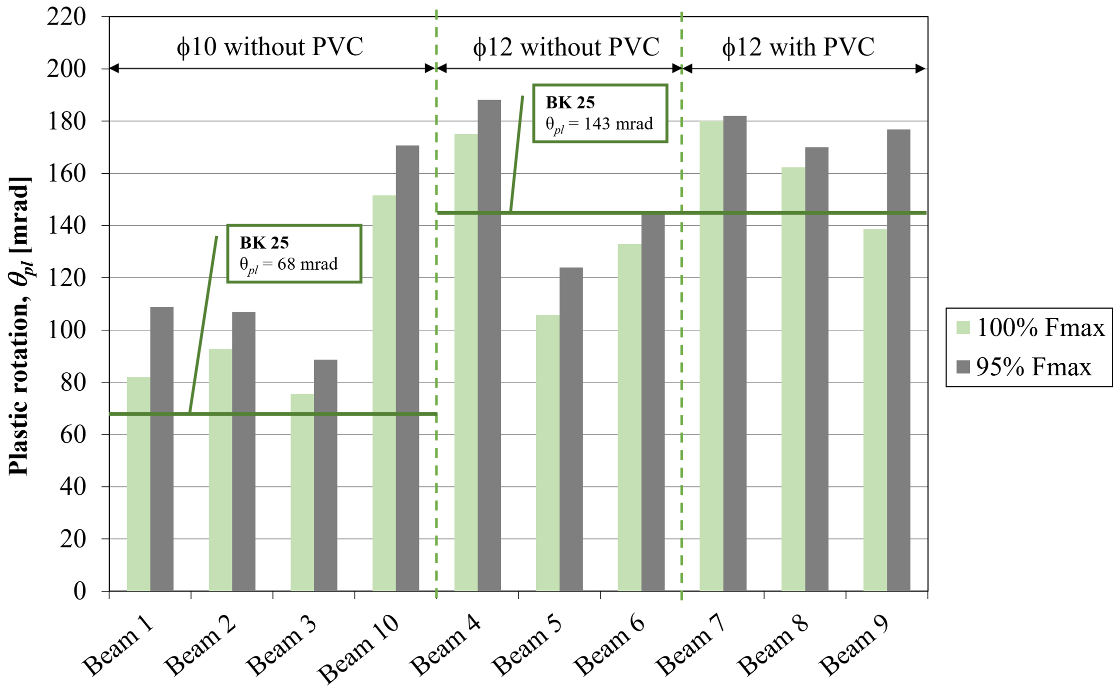

Figure 7.21 *Plastic rotational capacity of each beam corresponding to 100%* F_{max} *and 95%* F_{max}.

7.6 Summary of the beam test results

A summary of the maximum load, maximum deformation, average plastic reinforcement strain and utilization rate when considered the maximum average strain to the left or to the right side of the beam and plastic rotational capacity for each beam is presented in Table 7.15.

Table 7.15 Summary of test results.

Name	F_{max} [kN]	$u(F_{max})$ [mm]	u_{max} [mm]	ε_{ave} [‰]	Utilization [%]	$\theta_{pl,95\%}$ [mrad]	$\theta_{pl,100\%}$ [mrad]
Beam 1	36.4	81	107	31.6*	50	109	82
Beam 2	36.4	93	106	32.6*	51	107	93
Beam 3	37.1	78	89	21.8*	34	89	76
Beam 10	37.3	141	155	-	-	171	152
Beam 4	50.6	160	170	47.5	53	183	175
Beam 5	47.8	103	117	32.7	36	124	106
Beam 6	48.0	126	136	40.8	45	146	133
Beam 7	48.2	165	165	51.9	58	182	180
Beam 8	50.2	149	155	49.1	54	170	162
Beam 9	48.9	132	169	50.8	56	177	139

* Ruptured bar.

8 Discussion

The discussion includes general observations and interpretations of the results and the chapter is divided into three parts, the first part regarding the results from the beam tests and the second part the plastic reinforcement strain. The last part includes discussion about the test setup and how the results can be applicable on impulse loaded structures.

8.1 Structural response

From the beam test results it can be observed that the beams with ϕ 10 reinforcement have lower capacity for both maximum load and plastic deformation compared to beams with ϕ 12 reinforcement, see Figure 8.1. Theoretically, the final failure should have occurred in the middle of the beam because of the dead weight. However, due to reasons as asymmetric loading, natural scatter in the material and locally confinement effects of loading plates, most of the failures were located closer to one of the point loads.

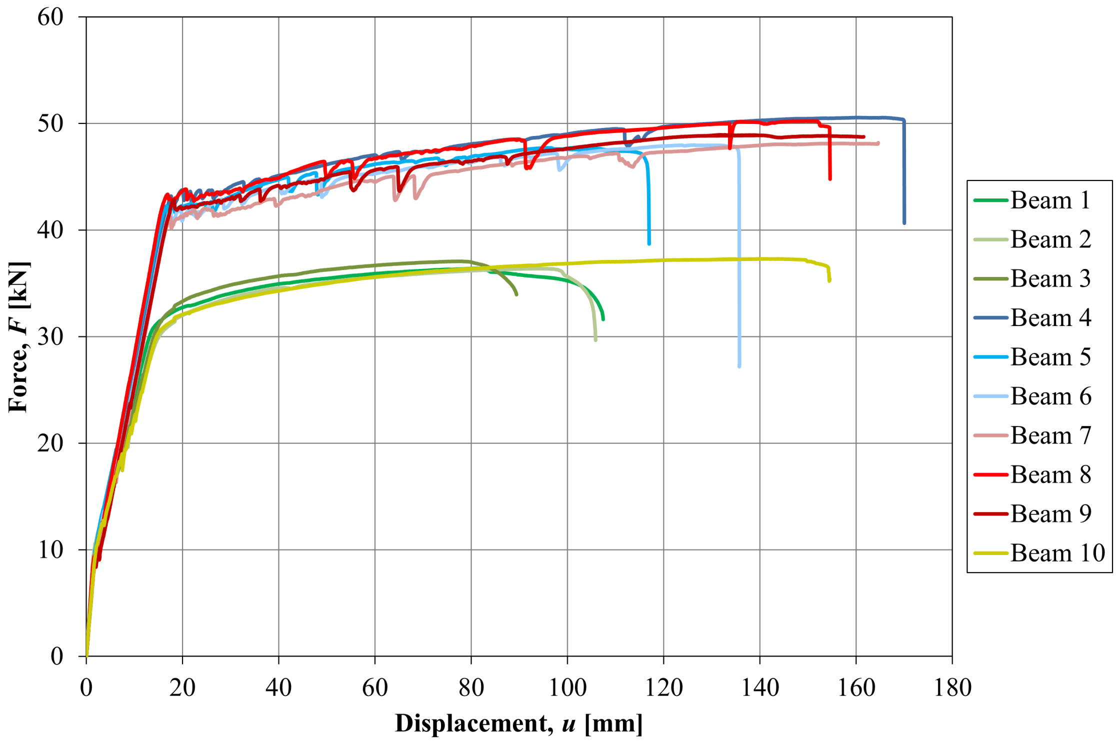

Figure 8.1 Load-displacement curve of all tested beams.

In general, the beams with $\phi 12$ reinforcement and PVC tubes showed larger plastic deformation capacity compared with the beams with $\phi 12$ reinforcement without PVC tubes, see Figure 8.2.

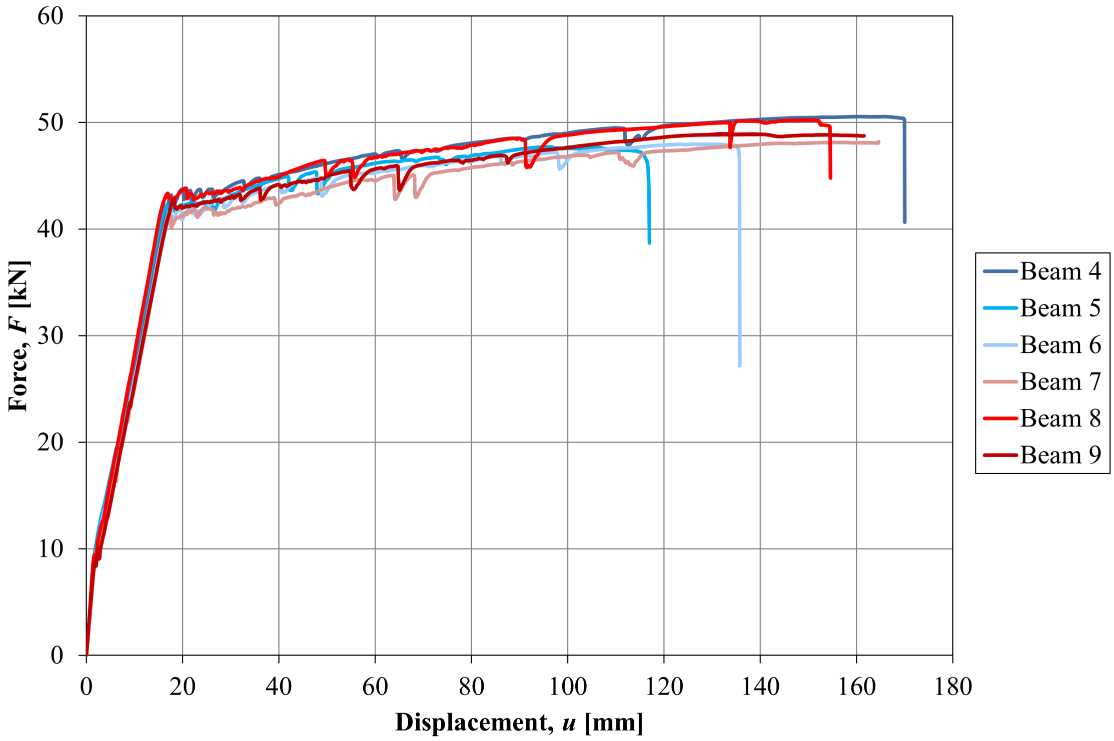

Figure 8.2 Load-displacement curve of beams with ϕ 12 reinforcement.

However, beams 10 and 4 provided larger deformation capacity compared to other beams in their group. The difference in behavior of the beams in each group can somehow be justified based on differences in material properties, test setup and test application. Symmetrical deformation and larger loading plates are both expected to have had positive effect on the ultimate capacity of the tested beams. Larger loading plates increased the confinement effect and lead to locally higher concrete strength and ductility in regions close to the loading plates.

The results from the tensile strength test of the reinforcement in beam 10, see Table B.9, indicates that the reinforcement quality differ from the one used in beam 1, 2 and 3. The results did not show a significant difference in total tensile capacity but higher f_u/f_y ratio. The larger deformation capacity of beam 10 can be due to its symmetrical behavior while beams 1, 2, and 3 had a more unsymmetrical deformation.

Beam 4 provides a considerable large capacity even compared to beams with PVC tubes. This beam has large loading plates which lead to larger capacity than beam 5 with small loading plates. It is also expected for this beam to have larger capacity than beam 6 as it has a more symmetrical behavior while the response of beam 6 is unsymmetrical.

The average values of load-displacement for beams in each group represent larger capacity for beams with PVC tubes than beams without. The $\phi 12$ beams also show larger capacity than the $\phi 10$ beams as expected. As the number of data from results are not the same for different beams and beams do not fail at the same displacement, it is not possible to continue the average curve after failing of the first beam in a group. The average value of final deformation capacity is therefore shown by dashed lines in Figure 8.3.

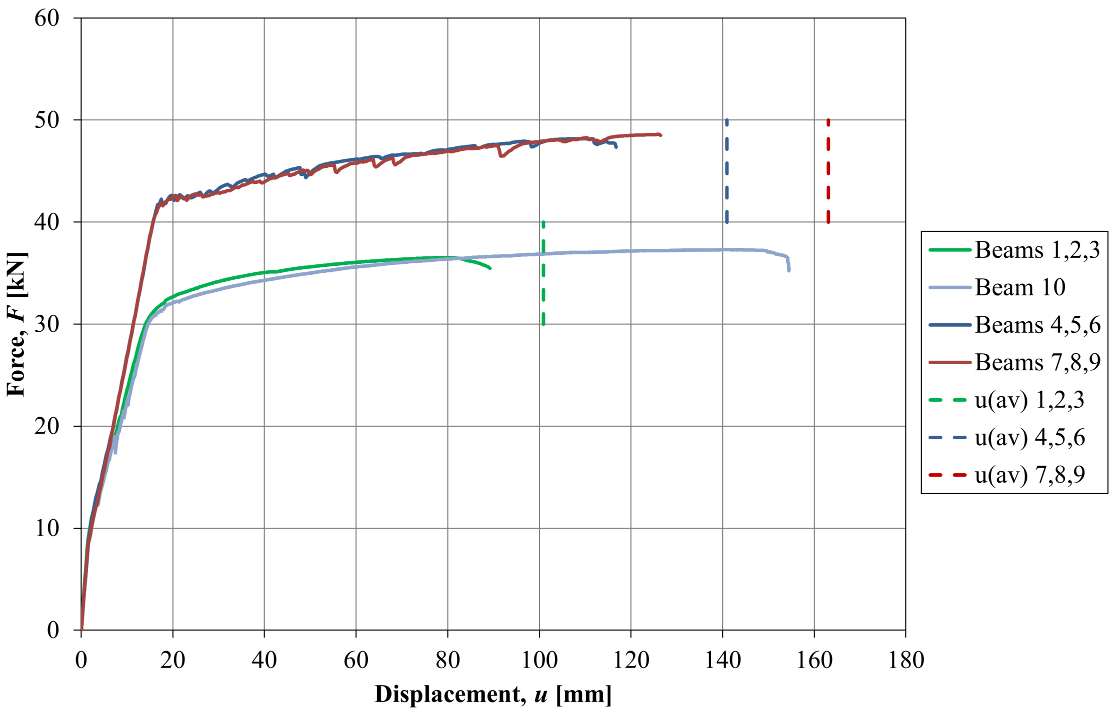

Figure 8.3 Average load-displacement curve of each group.

Beams with $\phi 10$ reinforcement failed due to reinforcement rupture and beams with $\phi 12$ reinforcement failed because of concrete crushing. This behaviour can also be reasoned according to the concept presented in Figures 3.14 and 3.19. In Figure 8.4 the value of $\theta_{pl,EC}$ is calculated based on German method, see Section 3.3.4, for beams with material and geometry properties of tested beams. The blue line and dash-line show the curve for the relation between plastic rotation and x/d ratio for class C reinforcement. The ratio of x/d is calculated in Appendix C for beams with material and geometry properties of tested beams with $\phi 10$ and $\phi 12$ reinforcement. The ratio of x/d for a tested beam with $\phi 10$ reinforcement is 0.061 and for a tested beam with $\phi 12$ reinforcement is 0.083 which are shown by the yellow points. The position of these yellow points indicates that the type of failure observed in the tests can be anticipated from these curves. Although the concept in Eurocode 2 and German method is not meant to be used to estimate θ_{pl} for four-point bending test, but it can still provide help to predict the failure mode.

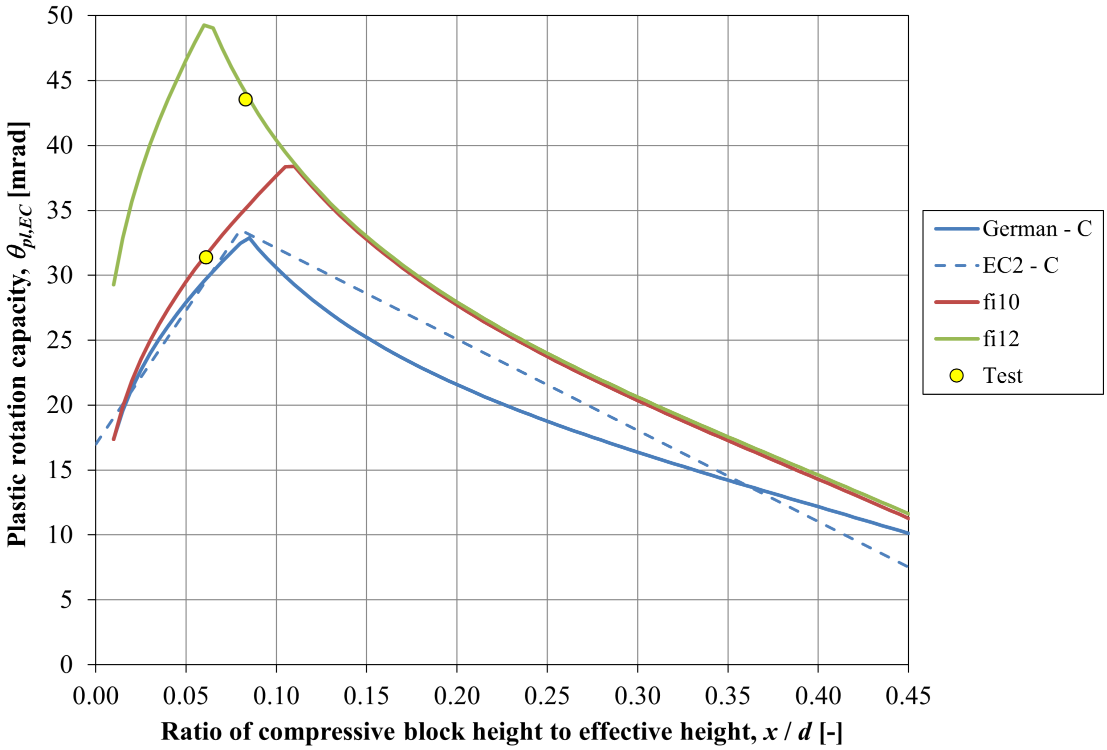

Figure 8.4 Average load-displacement curve of each group.

In case of plastic rotation capacity from test results, the ϕ12 beams with PVC tubes show larger capacity than beams without tubes and the ϕ12 beams provide larger capacity than ϕ10 beams. Although beam 10 in first group and beam 4 in second group are exceptions, comparison of average plastic rotational capacity can prove the significant positive effect of PVC tubes.

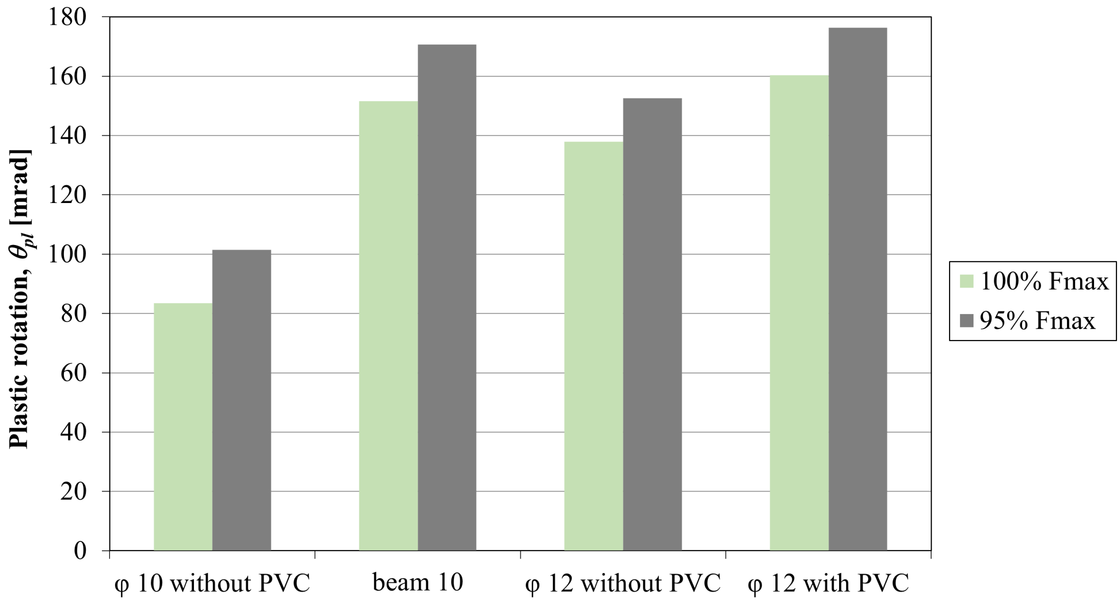

Figure 8.5 Average plastic rotational capacity for each group.

Plastic tubes prevent stress transition between reinforcement and concrete so, the reinforcement can elongate more inside the PVC tube as it is not restricted by concrete. Consequently, the number of cracks decrease by using PVC tubes but the crack width increases as there is larger plastic deformation.

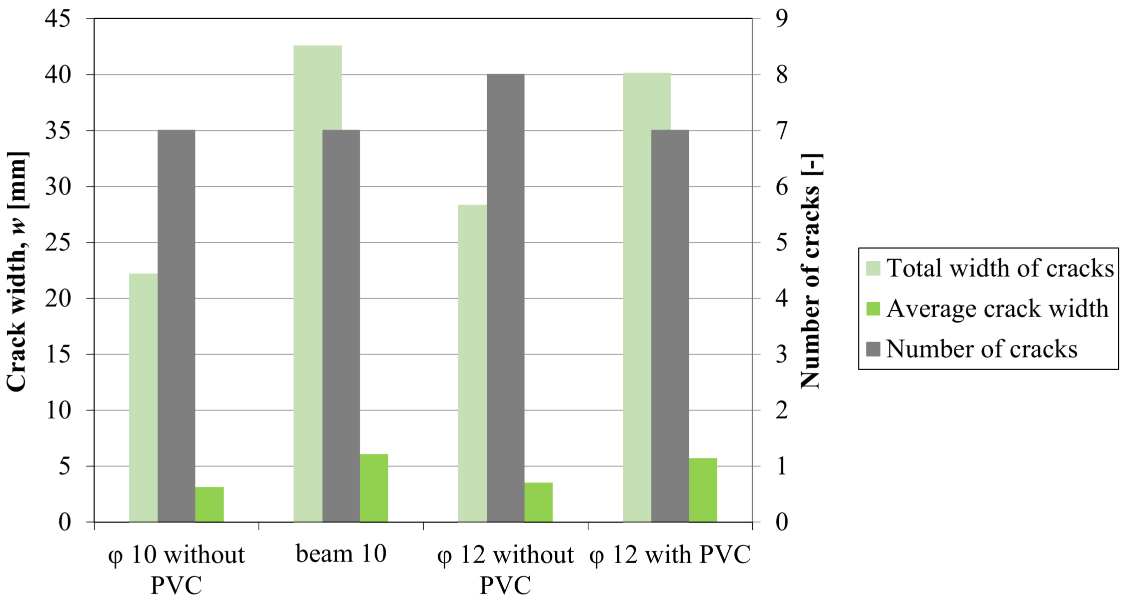

Figure 8.6 Average values of crack width, total width of cracks , and number of cracks for each group.

8.2 Plastic reinforcement strain

From Section 8.1 it can be concluded that the PVC tubes had a positive effect on the average plastic strain. By decreasing the interaction and the bond between the reinforcement and concrete, the plastic deformation capacity increased. The beams with plastic tubes generally provided a higher average strain and utilization rate compared with the beams without tubes. The $\phi 12$ bars had higher measured strains compared to the $\phi 10$ bars. However, since the result from the material testing showed the the strain at ultimate stress for the $\phi 12$ reinforcement was equal to 90 ‰ and 64 ‰ for $\phi 10$, see Table 7.3, they both resulted in similar utilization rates. The utilization rate is an important parameter with respect to the plastic deformation capacity. To utilize the plastic deformation capacity of the reinforcement, the average strains should be similar to the strain at ultimate stress of the material in order to increase the deformation capacity of the beams.

The result with similar utilization rates for the different reinforcement diameters were not expected. The $\phi 12$ reinforcement was expected to result in a higher utilization rate compared to the $\phi 10$ reinforcement since an increased bar diameter results in larger reinforcement ratio with more cracks and therefore higher strains and higher load capacity which reduce the effect of tension stiffening. One possible reason to the similar utilization rates could be that the results from the material testing of the $\phi 10$ bar showed that the strain at ultimate stress was equal to 64 ‰ which is a lower result compared to the recommended value for class C reinforcement, equal to 75 ‰, see Table 3.1.

How the calculations are performed to estimate the average reinforcement strains highly affects the results. From Table 7.7 it can be seen that the average calculations of the full beam, to the left or to the right side of the beam were different depending on which values were considered. In the summary table, see Table 7.15 the average strains and utilization rates are estimated based on the maximum measured strain to the left or to the right side of the beam since this value is more reasonable to used when defining the capacity of the reinforcement. From Table 7.7, it can also be seen that there are some scatter in the results. Beam 3 showed a considerable lower average strain compared to the other $\phi 10$ beams and the same for beam 5 which also had a lower average strain compared to the other beams of the same type. Beam 4 provided a higher average strain compared to the other beams of same type and the results from the second tensile strength test of the reinforcement indicates a somewhat higher f_u/f_y-ratio compared to the other reinforcement specimens, see Table B.10. However, the results from the strain measurements corresponds well to the results from the beams tests. As mentioned, beam 4 had large measured strains and large deformation capacity, see Table 7.15, and beam 3 had the lowest measured strain and the lowest deformation capacity which shows that the there is a good correlation between the results.

The effect of plastic tubes on the strain measurements was expected to result in constant strain where the tubes were placed since no interaction with the concrete results in no stress transfer and an evenly distributed elongation. To see the effect with constant strain under the tubes in the bar charts from the strain measurement result, the position of the tube in relation to the marks is important, see Figure 8.7. From Figures D.7 - D.9 and Figure D.17 it can be seen that the expected results with constant strain were more or less achieved for most of the bars. A small difference between the measured strains at the position of the tube can be explained by the precision of the measurements since the accuracy highly effects the resulting strain and as mentioned in Section 7.4.2, 1 mm elongations corresponds to 20 ‰ strain. Another factor that might influence the results is the friction between the materials which may result in a bond between the materials where it is expected to be no interaction. At the location of some tubes, e.g. beam 7, see Figure D.7 at the third tube (coordinate 1300 and 1350), the strain was not constant. However, the results from the 3D scanning of beam 7, Figure D.17 showed a smaller difference between the measured strains which indicates that the non constant strain from the manually made measurements is caused by an error in the measurement.

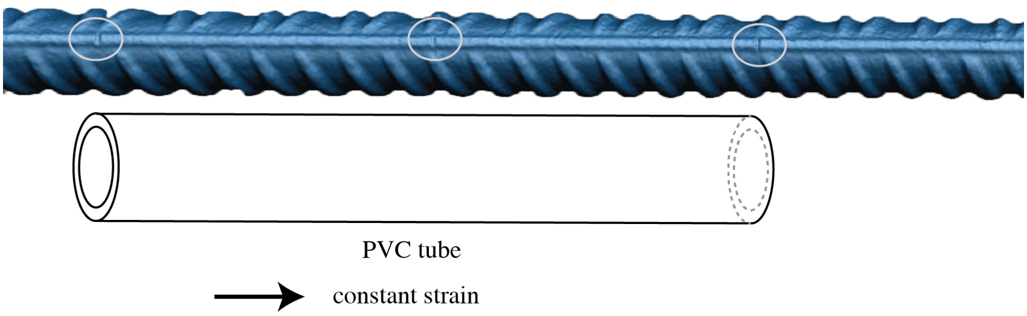

Figure 8.7 Placing of tube in relation to the marks which is expected to result in constant measured strain.

During this master's project, the 3D scanning has been used as an alternative method to measure the elongation and calculate the reinforcement strain rather then estimate the average reinforcement strain and utilization rates since only three beams were scanned. The 3D model was used in a similar way as for manually measurements, by measuring the elongation between the marks. The results from the two different methods were compared and they resulted in similar plastic strain, see Figures 7.16 - 7.18. However, some exceptions with deviating results due to loss of data in the 3D model. As long as there is no data loss in the 3D scanning, the 3D model enables a more accurate measuring tool since the accuracy of the measurements with the measuring tape were limited to approximately 0.5 mm and 1 mm elongation corresponds to 20 ‰ measured plastic strain.

Also, the 3D model of the bars made it possible to study the change in cross-sectional area due to yielding. The results showed that the cross section decreased approximately 8%-13% for the part with largest measured strain. At rupture, the cross-sectional reduction was even higher. Due to missing data from two of the bars, the part that was next into the part with largest strain had to be used in the analysis and the results show a somewhat lower reduction compared to the bars where the part with largest strain was used.

8.3 Test setup

As mentioned in the introduction, the FKR 2011 (Swedish Fortification Agency, 2011) provides design regulations to structures subjected to not only static loading but also to withstand impulse loads such as explosions. An explosion load can be described or simplified by a uniformly distributed load. However, due to difficulties to simulate a uniformly distributed load, a test setup with two point loads was chosen in this master's project as a simplification to analyse the structural behaviour of reinforced concrete structures loaded until failure. The difference in terms of plastic deformation and formation of plastic hinges between a uniformly distributed load and point loads are described in Section 3.2.3. From Figure 3.6, it can be seen that a four-point bending test setup results in similar length of yielding region l_y as for a uniformly distributed load. In case of impulse loaded structures, the application of PVC tubes would have been performed in a similar way as in this project. To get the desired effect of the plastic tubes, the tubes should be placed in the region where the plastic hinge is expected to form. In Figure 8.8 a schematic illustration of the formation of plastic hinges is shown. The location of the plastic hinges in this project is a simplification whereas in reality the hinges is distributed over an area, see Figure 3.1.

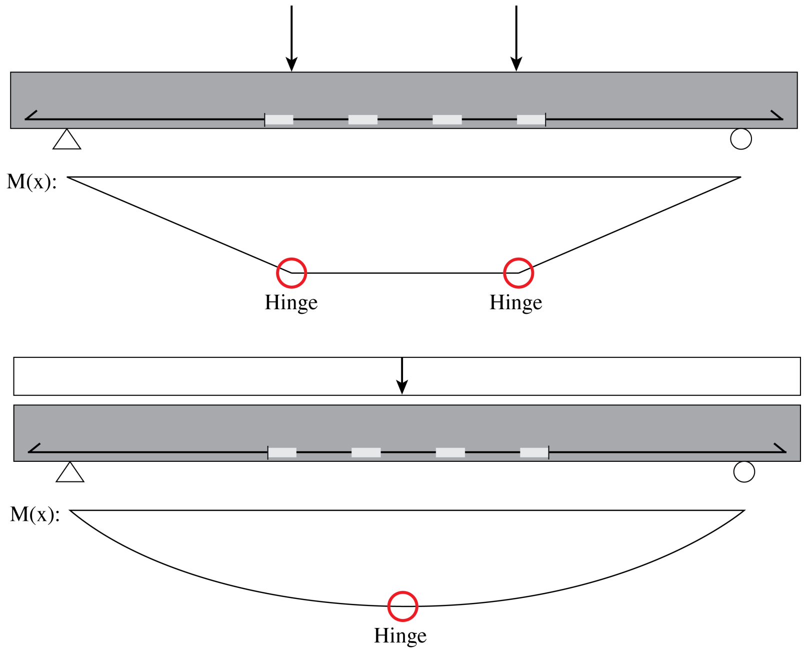

Figure 8.8 The concept of plastic tubes with respect to the formation of plastic hinges and the difference between two point loads and a uniformly distributed load.

Although the loading situations are different from each other, the concept of placing PVC tubes in the region with plastic hinges are formed to increase the deformation capacity can still be applied.

The configuration of the plastic tubes is one parameter that effects the reinforcement strain and the deformation capacity. Test results from Köseoğlu (2020) showed that the PVC configuration with 8x50mm was the arrangement which resulted in the largest deformation capacity. The test also included PVC tubes with configuration 4x100, but with a spacing equal to 100 mm instead of 200 mm which was used in this project. The different spacing, results in different crack development and reinforcement strain. A larger spacing means a longer transmission length which allows the stresses to be transferred from the reinforcement to the concrete. This implies that the configuration used might not be the most optimal one. Therefore, an optimization of the PVC tube configuration might be effective to further increase the reinforcement strain and the deformation capacity.

9 Final remarks

9.1 General description

The aim of the thesis project was to increase the knowledge about the structural response of reinforced concrete beams with focus on the average plastic reinforcement strain at failure to increase the plastic deformation capacity. Experimental studies in terms of static four-point bending tests were preformed in order to investigate how the average plastic strain can be affected by the reinforcement amount and reduced bond between the reinforcing steel and the concrete.

At first, a literature survey was done to deepen the knowledge about the structural behaviour of reinforced concrete structures. Background information about plain concrete, reinforcing steel and reinforced concrete was treated with focus on the structural response and change of behaviour with respect to the bond between the materials, which is an important factor of reinforced concrete's behaviour and the formation of cracks. To describe the structural behaviour at failure, a theory based on plastic deformation capacity is needed since the structure will have considerable plastic deformation. The literature study also includes different methods to determine the plastic deformation capacity.

Ten concrete beams with the same dimensions, different reinforcement amount and bond between the concrete and reinforcement were manufactured. The plain concrete and reinforcement was tested to obtain necessary background information about the material properties. Static four-point bending tests were performed until rupture of reinforcement or crushing of concrete. DIC, measurements and 3D scanning were used to determine load-displacement curves, crack pattern and plastic reinforcement strain.

9.2 Conclusions

In general, the beams with $\phi 12$ reinforcement provided higher capacity with respect to ultimate load and plastic deformation compared with the beams with $\phi 10$ reinforcement and the effect of PVC tubes resulted in larger plastic deformations. During testing, the importance of symmetric loading on the ultimate capacity of the beam was observed. The beams with symmetrical deformation showed an increased plastic deformation compared to the beams with unsymmetrical deformation.

Moreover, two different failure modes were observed, the beams with $\phi 10$ reinforcement were more likely to fail due to rupture of reinforcement and $\phi 12$ beams because of crushing of concrete. The main factors influencing the structural behaviour and location of rupture were asymmetric loading, natural scatter in the material and locally confinement effects in the concrete close to the loading plates.

Comparing the values of plastic rotational capacity from test results with results from BK 25 and Eurocode, it was observed that BK 25 provides a good estimation of θ_{pl} for a simply supported beam under four-point bending test while the results from Eurocode 2 showed a large difference. However, the concept of Eurocode for anticipation of failure mode considering the ratio of x/d showed the same outcome compared to failure modes in tests.

The results from the plastic strain measurements showed similar utilization rates for the $\phi10$ and $\phi12$, equal to 45 ‰. The PVC tubes resulted in positive effects with increased average reinforcement strain and utilization rate equals 56 ‰ . The results from the strain measurements and the 3D scanning were similar with some deviating results due to loss of data in the 3D model. However, in case of no data loss, the 3D model enables a more accurate tool to measure the elongation since the accuracy of the measuring tape is limited to distinguish elongations greater than 0.5 mm.

Overall, the test results show that application of PVC tubes has a positive effect of the average reinforcement strain with an increased utilization rate and plastic deformation capacity. The reduced bond resulted in fewer cracks and larger average crack width which had a positive effect on the average reinforcement strain and thus the plastic rotation and deformation capacity of the beams. Also, DIC method is considered as a powerful tool in this type of experimental study to monitor and record the structural behavior during testing.

9.3 Further research

In this test series, the beams were subjected to two point loads to obtain a zone within the loads with constant moment. However, an improvement of the test setup would have been to increase the number of point loads to simulate a loading situation more similar to an uniformly distributed load; i.e that of an impulse load from an explosion. A load rig with larger space would allow for larger deformations and prevent the session to be interrupted before failure. For some of the beams, the session stopped because the steel loading beam got in contact with the concrete beam due to large deformations. Also the movements of the supports, both the roller supports at the point loads and the supports of the beam were crucial during testing. To increase the capacity, the size of the loading plates were changed and the plate size's effect on the structural response and ultimate capacity was discussed. However, further investigation on the load plate size effect requires non-linear FE analysis.

Furthermore, the PVC volume's effect on the reinforcement strain is also of interest in further research, by testing different PVC tube configurations and volumes and application of PVC tubes on critical regions to find the most optimal configuration and increase the reinforcement strain and the deformation capacity. An addition to the laboratory testing, a FE-analysis can be performed to investigate the interaction between the materials and how the bond effects the reinforcement strain and the deformation capacity. Also, a more complex reinforcement configuration or increased reinforcement ratio with e.g. reinforcement cages, stirrups or reinforcement in multiple layers can result in an increased effect of the reduced bond's influence on the reinforcement strain. The advantage with two reinforcement bar in one layer at the bottom is the simpler manufacturing process but a more complex reinforcement configuration could be of interest in further studies.

In conclusion, more point loads would help the loading situation to be more similar an impulse load and a load rig which allow for larger deformations would ensure the beams to reach failure without stopping the loading session. An optimized or different PVC configurations together with a more complex reinforcement configuration and different reinforcement ratios to display the influence on the average reinforcement strain and plastic deformation capacity might be of interest in further research.

References

Al-Emrani, M., Engström, B., Johansson, M., & Johansson, P. (2011). *Bärande konstruktioner - Del 2*. Chalmers University of Technology.

Al-Emrani, M., Engström, B., Johansson, M., & Johansson, P. (2013). *Bärande konstruktioner - Del 1*. Chalmers University of Technology.

Ansell, A., & Svedbjörk, G. (2000). *Statisk provning av fritt upplagda plattstrimlor av betong med armering av varierande seghet*. Avdelningen för Betongbyggnad, Kungliga Tekniska Högskolan, Teknisk rapport 2000:16, Stockholm.

CEB. (1998). *Ductility of reinforced concrete structures*. CEB bulletin 242.

CEN. (2004). *EN 1992-1-1 Eurocode 2: Design of concrete structures - Part 1-1: General rules and rules for buildings* . European Committee for Standardization.

CEN. (2019). *EN 12309-3: Testing hardening concrete - Part 3: Compressive strength of test specimens*. European Committee for Standardization.

DAfStb. (2010). *Heft_525 Explanations of DIN 1045* (2nd edition). Beuth-Verlag.

Engström, B. (2014). *Restraint cracking of reinforced concrete structures*. Chalmers University of Technology.

Engström, B. (2015). *Design and analysis of continuous beams and columns*. Chalmers University of Technology.

Johansson, M., Hallgren, M., Ansell, A., Magnusson, J., & Leppänen, J. (2021). *Plastisk deformationsförmåga och tvärkraftsrespons hos impulsbelastade betongkonstruktioner*. Chalmers University of Technology, Report ACE 2021:5.

Johansson, M., & Laine, L. (2012). *Bebyggelsens motståndsförmåga mot extrem dynamisk belasting. Del 3: Kapacitet hos byggnader*. Myndigheten för samhällsskydd och beredskap.

Jönsson, J., & Stenseke, A. (2018). *Concrete beams subjected to repeated drop-weight impact and static load* (Master's thesis). Chalmers University of Technology.

Köseoğlu, E. (2020). *Average reinforcement strain in reinforced concrete structures loaded until failure.* (Bachelor's thesis). Chalmers University of Technology.

Latte, S. (1999). *Plastic Rotation Capacity of Reinforced Concrete Beams* (Master's thesis).

Löfgren, I., Forbes Olsen, J., & Flansbjer, M. (2004). *Application of WST-method for fracture testing of fibre-reinforced concrete*. Chalmers University of Technology, Report 04:13.

Lozano, F., & Makdesi, J. (2017). *Concrete Beams Subjected to Drop-weight Impact and Static Load* (Master's thesis). Chalmers University of Technology.

Lundgren, K. (1999). *Three-Dimensional Modelling of Bond in Reinforced Concrete* (Doctoral dissertation). Chalmers University of Technology.

Plos, M., Johansson, M., Zandi, K., & Shu, J. (2021). *Recommendations for Assenssment of Reinforced concrete slabs*. Chalmers University of Technology, Report ACE 2021:3.

Swedish Fortification Agency. (2011). *Fortskydd. Bilaga till Fortifikationsverkets Konstruktionsregler FKR 2011.* Försvarsmakten.

Tammo, K. (2009). *A new approach to crack control for reinforced concrete* (Doctoral dissertation). Lund University, Report TVBK-1037.

Zilch, K., & Zehetmaier, G. (2010). *Bemessung im konstruktiven Betonbau* (2nd edition). Springer Verlag.

A Experiment preparations

The preparation started with cutting the reinforcements in length 2.79 m for beams and six samples from each size of reinforcement for tensile testing. The cut reinforcement bars were marked every 50 mm by using a hammer and an awl to prepare for the plastic strain measurement. Also, each bar was marked with a letter to keep the different reinforcement bars apart and to know which bar that correspond to a certain beam. The middle 1 m of the reinforcement bar was marked using zip ties.

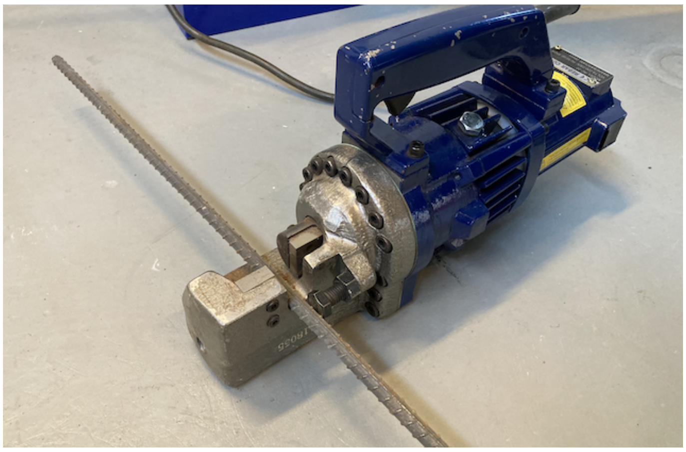

Figure A.1 The reinforcement was cut to fit into the beam.

From each type of beam, (beam 1, 4 and 7) two bars were scanned with 3D scanning tools to be used for comparison with the plastic strain calculations. The reinforcement bar was placed in a frame build for the 3D scanning, see Figure A.2. The software VXelement was used to create the 3D model of the bars, see Figure A.3 and the data was exported as a point cloud mesh to measure the elongation of the bars and the cross-sectional change due to yielding. Further information about the 3D scanning can be found in Appendix D.

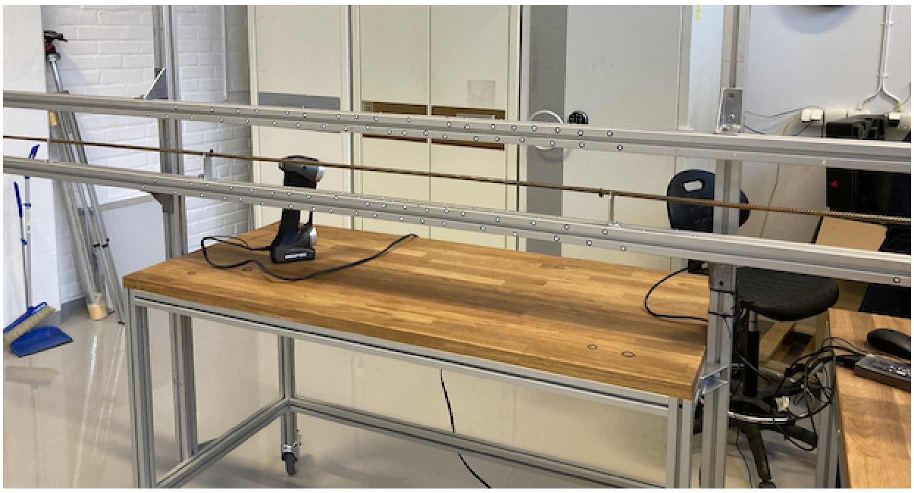

Figure A.2 The setup for the 3D scanning, which shows the frame, 3D scanner and placement of the reinforcement.

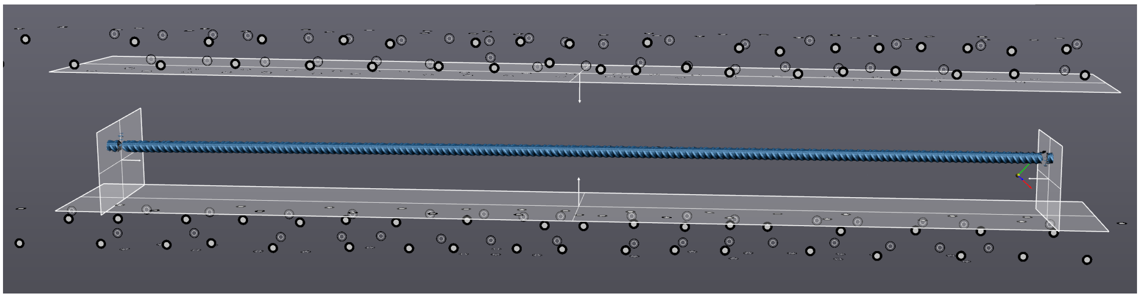

Figure A.3 The 3D scanning model in the software VXelements.

After the 3D scanning, PVC tube segments with length of 100 mm and spacing 200 mm were glued at the middle 1 m of the reinforcement bars used in the three beams with PVC tubes.

The forms were oiled to simplify the cleaning after casting and then the reinforcement bars were placed inside the forms. Spacers were nailed in the from in order to have 35 mm concrete cover. Figure A.4 shows an example of the reinforcement configuration with and without plastic tubes.

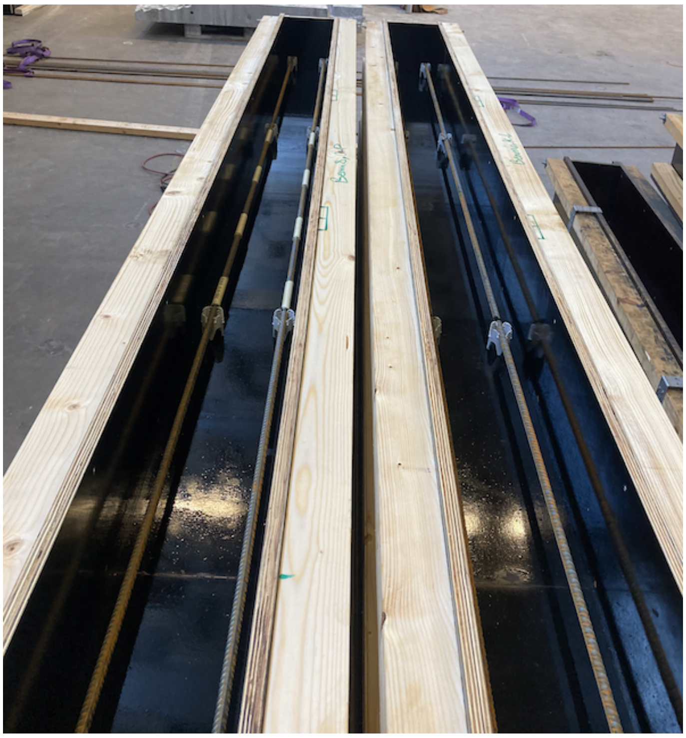

Figure A.4 Example of the two casting forms. The form to the left with plastic tubes and to the right without plastic tubes.

Figure A.5 Preparations of the forms before casting. The ten closest forms were prepared for this thesis.

Figure A.6 Preparations of the forms before casting. The forms to the left were prepared for this thesis.

The concrete was delivered to the site by a concrete mixing truck and the fresh concrete was poured from the truck into the forms, see Figure A.7 and A.8 . Also, concrete cubes for material testing were casted. A vibrator was used to eliminate air in the concrete. The beams were watered before covered by a plastic sheet to harden, see Figure A.9 and the cubes were submerged in water until the material testing.

Figure A.7 *The fresh concrete was poured into the forms from the concrete mixer truck.*

Figure A.8 *Casting of the concrete beams.*

Figure A.9   The beams were stored under plastic sheet to cure.

After hardening of concrete, the moulds were removed and the beams were painted with a white background and black speckle pattern to prepare for the DIC recording. A DIC camera was used during the bending test to document the development of cracks and the deformation of the beam.

Figure A.10   The beams were painted with a white backdrop to prepare for the DIC.

Figure A.11 *The white beams were painted with a black speckle pattern to prepare for the DIC.*

The last part was to prepare the loading rig with two point loads, see Figure A.12 and the DIC camera for recording of crack development and deformation of the beam, see Figure A.13.

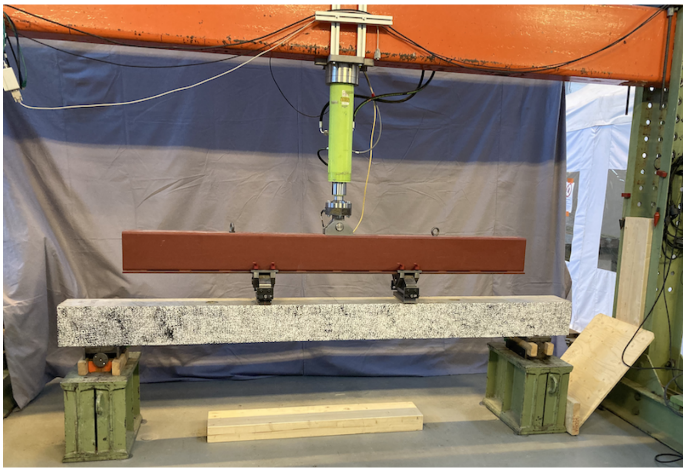

Figure A.12 *The static four-point bending test setup.*

Figure A.13 The static four-point bending test setup with the DIC camera.

B Material testing

In order to obtain necessary background information about the materials, different material tests were performed. A more detailed description of the test setups, performance and results are presented in the following appendix.

B.1 Concrete properties

To study the structural behaviour of the concrete beams, material testing is necessary to gain knowledge about the concrete properties. Two different tests were conducted, one to determine the compressive strength and one to determine the fracture energy.

B.1.1 Compressive test

The concrete compressive strength test was performed at two different occasions. The first one to determine the 28-days strength and the second one after 40 days. The test was performed and the compressive strength was determined according to CEN (2019). The setup of the compressive test is presented in Figure B.1 and examples of failure modes are shown in Figure B.2.

Figure B.1 Test setup for the compressive strength test.

Figure B.2 Example of failure modes.

The applied force and compressive strength for each specimen and the mean strength of the 28 days and 40 day, respectively are presented in Table B.1 and Table B.2. The average density of the cubes was equal to 2370 kg/m^3 at 28 days and 2445 kg/m^3 at 40 days.

Table B.1 28-days compressive strength test results.

Cube no.	Applied force [kN]	Strength [MPa]
1	1472.3	65.4
2	1391.2	61.8
3	1508.7	67.1
Mean strength	1457.4	64.8

Table B.2 40-days compressive strength test results.

Cube no.	Applied force [kN]	Strength [MPa]
1	1621.4	72.1
2	1588.8	70.6
3	1539.5	68.4
Mean strength	1583.2	70.4

The results can be used to calculate the cylindrical strength according to Equation (2.1) and then the modulus of elasticity can be estimate with Equation (2.6). In Table B.3, the estimated cylindrical strength and modulus of elasticity is presented for the days where the compressive tests were performed and the results are used to interpolate the concrete properties at 33 days which correspond to the day in the middle of the week when the beam test were preformed and used as input data for the predictions in Chapter 6.

Table B.3 The estimated cylindrical strength and modulus of elasticity.

Age [days]	Cylindrical strength [MPa]	Modulus of elasticity [GPa]
28	54.0	36.5
33	56.0*	36.9*
40	58.7	37.4

* Values based on interpolation.

B.1.2 Wedge splitting test

A wedge-splitting test was performed according to the recommendations given in (Löfgren et al., 2004) in order to predict the fracture energy G_F. The setup of the testing machine can be seen in Figure B.3.

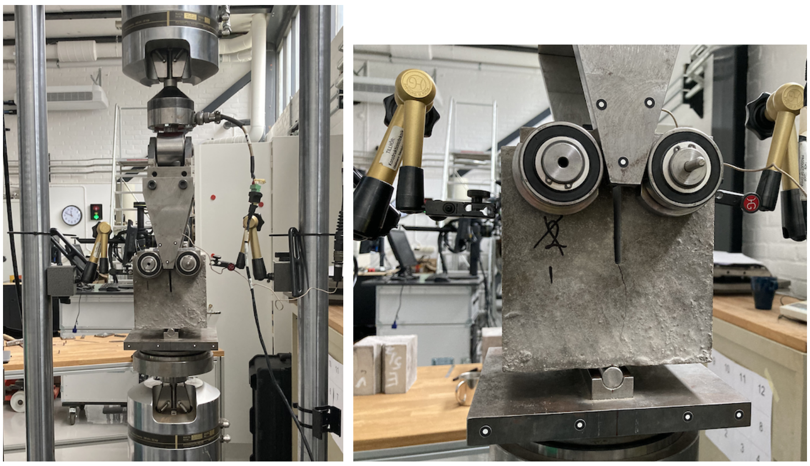

Figure B.3 Test setup for the WST.

A groove in the specimen was made during casting and starter notch was sawed with a thickness of 4 mm, see a_1 and a_2 in Figure B.4. Before the test was conducted, the three cubes were measured according to Figure B.4 and the dimensions are presented in Table B.4.

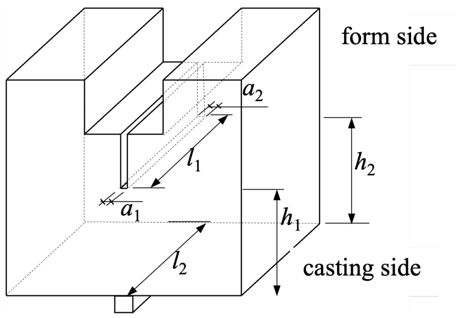

Figure B.4 Dimensions of the testing cube.

Table B.4 Dimensions of the different cubes with notations indicated in B.4.

Cube no.	weight [kg]	h_1 [mm]	h_2 [mm]	l_1 [mm]	l_2 [mm]	A [mm^2]
1	7.823	71.5	73.5	149.0	150.0	10839
2	7.852	72.5	74.5	148.0	150.0	10952
3	7.779	73.0	74.5	148.5	149.0	10970

The fracture energy is calculated as the area under the splitting load-CMOD diagram, see Table B.5. A summery of the fracture energy, maximum splitting force and the maximum CMOD for each of the three specimens are presented in Table B.5.

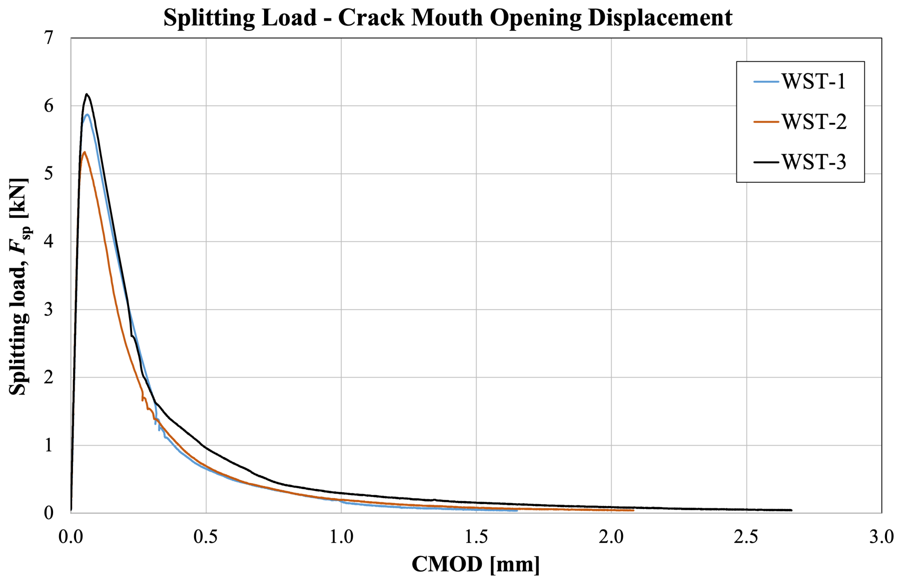

Figure B.5 Splitting load-CMOD diagram.

Table B.5 Summary of the WST results.

Cube no.	Accumulated G_F [Nm/m^2]	Maximum splitting load F_{sp} [kN]	Maximum CMOD [mm]
1	145	5.87	1.65
2	134	5.32	2.08
3	173	6.17	2.67

B.2 Steel reinforcement properties

The reinforcement had the quality class C and the steel reinforcement properties were determined by a tensile test. Six bars of each type of reinforcement were tested to determine the tensile strength. However, since the reinforcement was removed from the beams after the four-point bending test a second tensile test was performed by cutting one specimen from each reinforcement bar. Also, the reinforcement type in beam number 10 was unknown and needed to be determined.

- The length of the specimens were 410 mm
- The distance between the clamps on the tensile machine was set to 298 mm
- The loading speed was 5 mm/min up to 3 mm of elongation, followed by 120 mm/min until failure

An extensometer was connected to the specimens in order to get a detailed measurement of the elongation, see Figure B.6. The loading was stopped to remove the extensometer prior to failure which resulted in a drop in the stress-strain curve.

Figure B.6 Steel reinforcement test setup with the extensometer.

Figure B.7 Example of steel reinforcement necking under tensile strength test.

B.2.1 ϕ10 reinforcement

The results from the first reinforcement test are presented in a stress-strain curve, see Figure B.8. The modulus of elasticity, strain at ultimate stress, yielding strength, ultimate strength and the f_u/f_y ratio are presented in Table B.6.

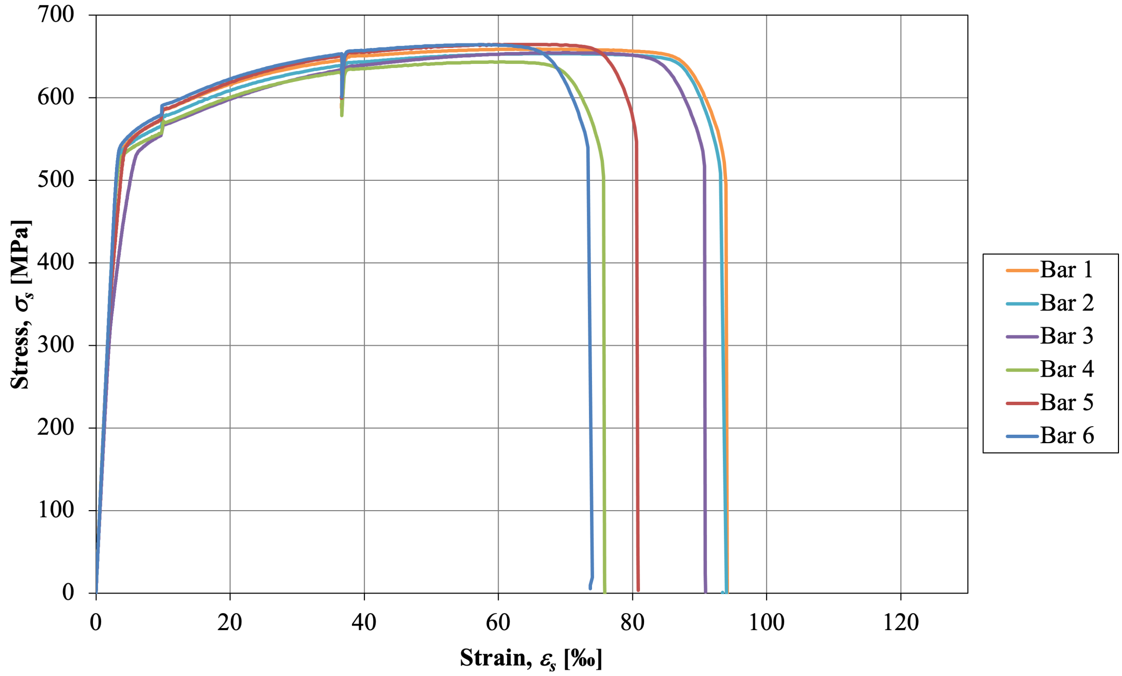

Figure B.8 Stress-strain curve for six ϕ10 steel reinforcement bars.

Table B.6 Modulus of elasticity, strain at ultimate stress, yielding strength, ultimate strength and f_u/f_y ratio for six ϕ10 together with average values.

Bar sample	E_s [GPa]	ε_{su} [‰]	f_y [MPa]	f_u [MPa]	f_u/f_y [-]
1	205	63	570	659	1.16
2	220	67	563	653	1.16
3	189	70	551	654	1.19
4	203	60	555	643	1.16
5	187	65	571	664	1.16
6	188	57	576	664	1.15
Average	198	64	564	656	1.16

B.2.2 ϕ12 reinforcement

The results from the first reinforcement test are presented in a stress-strain curve, see Figure B.9. The modulus of elasticity, strain at ultimate strength, yielding strength, ultimate strength and the f_u/f_y ratio are presented in Table B.7.

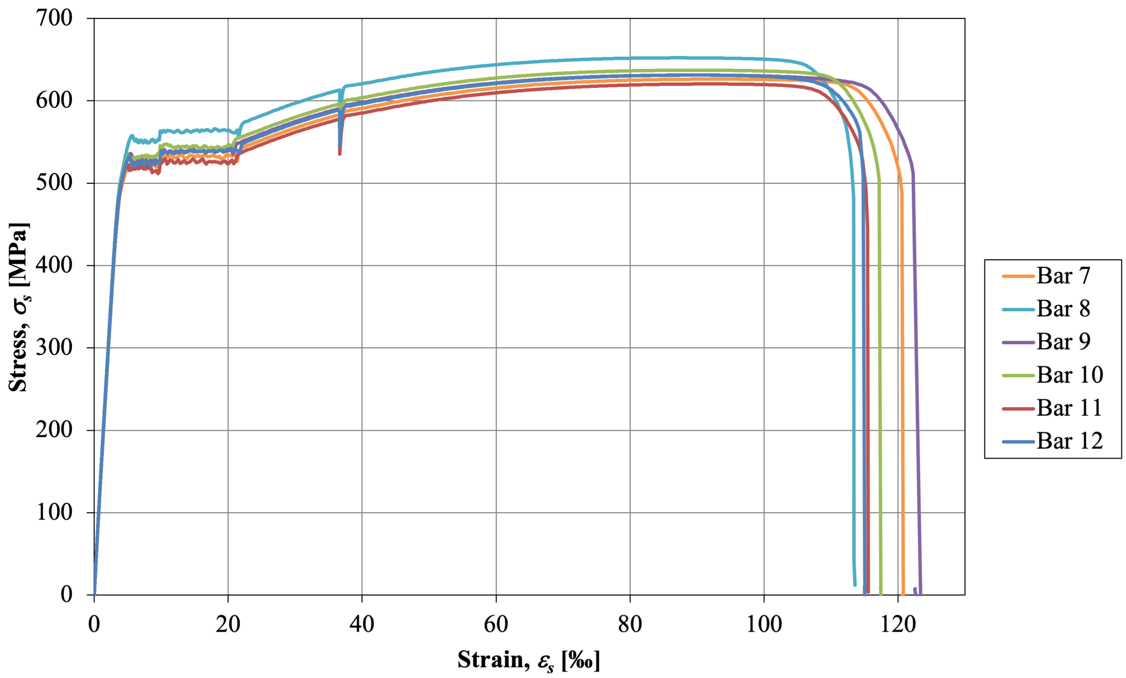

Figure B.9 Stress-strain curve for six ϕ12 steel reinforcement bars.

Table B.7 Modulus of elasticity, strain at ultimate stress, yielding strength, ultimate strength and f_u/f_y ratio for six ϕ12 together with average values.

Bar sample	E_s [GPa]	ε_{su} [‰]	f_y [MPa]	f_u [MPa]	f_u/f_y [-]
1	188	93	523	626	1.20
2	194	87	558	652	1.17
3	189	89	536	631	1.18
4	197	90	534	637	1.19
5	192	92	523	620	1.19
6	187	90	533	631	1.18
Average	191	90	535	633	1.18

B.3 Second reinforcement testing

The removal of reinforcement from the concrete beams after the four-point bending test made a second reinforcement test possible. Since the plastic strain close to the ends was expected to be equal to zero, specimens were cut from the end of the reinforcement bars. One specimen from each reinforcement bar was tested with the same procedure as the first tensile strength test. For beam number 10, the test beam, the reinforcement type was unknown and therefore in total four test was performed with specimens from each side of the reinforcement bars. The specimens for the second testing were cut to the same length as the ones from the first testing and the samples were taken from the end of the reinforcement bars. In total, six $\phi 10$ bars, four $\phi 10$ bars from the test beam and twelve $\phi 12$ bars were tested and the results are presented in Tables B.8 - B.10.

Table B.8 *Modulus of elasticity, strain at ultimate stress, yielding strength, ultimate strength and f_u/f_y ratio for six $\phi 10$ together with average values.*

Beam no	Bar sample	E_s [GPa]	ε_{su} [‰]	f_y [MPa]	f_u [MPa]	f_u/f_y [-]
1	A	195	72	567	660	1.16
	B	201	71	570	660	1.16
2	A	206	72	567	659	1.16
	B	205	68	573	664	1.16
3	A	187	65	584	673	1.15
	B	189	70	566	657	1.16
Average		197	70	571	662	1.16

Table B.9 *Modulus of elasticity, strain at ultimate stress, yielding strength, ultimate strength and f_u/f_y ratio for four $\phi 10$ bars from beam 10 together with average values.*

Bar sample	E_s [GPa]	ε_{su} [‰]	f_y [MPa]	f_u [MPa]	f_u/f_y [-]
A-1	203	70	544	643	1.18
A-2	202	73	561	660	1.18
B-1	195	69	553	651	1.18
B-2	191	74	556	655	1.18
Average	198	72	553	652	1.18

Table B.10 Modulus of elasticity, strain at ultimate stress, yielding strength, ultimate strength and f_u/f_y ratio for twelve $\phi 12$ together with average values.

Beam no	Bar sample	E_s [GPa]	ε_{su} [‰]	f_y [MPa]	f_u [MPa]	f_u/f_y [-]
4	A	165	86	527	631	1.20
	B	199	90	540	635	1.17
5	A	205	93	530	625	1.18
	B	198	93	520	619	1.19
6	A	193	93	526	625	1.19
	B	195	92	524	620	1.18
7	A	202	90	523	622	1.19
	B	192	93	517	616	1.19
8	A	194	89	526	621	1.18
	B	203	87	544	630	1.16
9	A	198	90	536	627	1.17
	B	196	93	524	619	1.18
Average		195	91	528	624	1.18

The results from the second testing indicates that the reinforcement bars in beam 10 were of a different type compared to the $\phi 10$ bars in the other beams. Therefore, the results from beam number 10 were treated separately from the other $\phi 10$ beams.

C Beam results, structural response

C.1 Load-Displacement curves

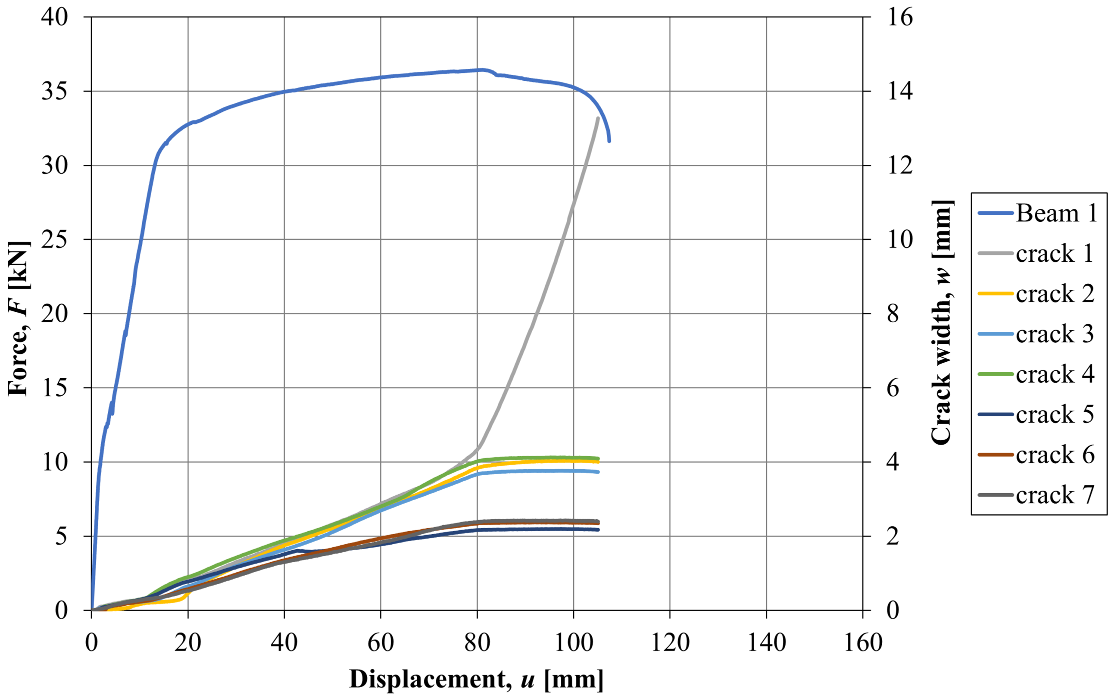

Figure C.1 Load-displacement curve for beam 1 ($\phi10$, without PVC tubes) and displacement-width curves for cracks. The values of crack width are measured at the level of reinforcements.

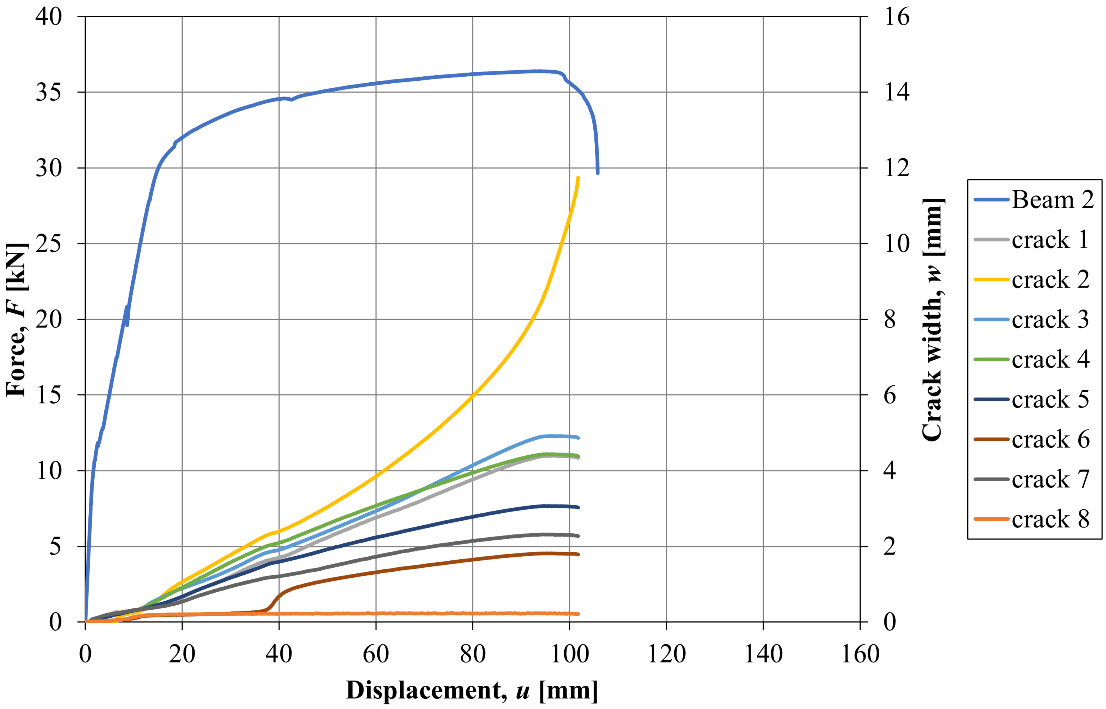

Figure C.2 Load-displacement curve for beam 2 ($\phi 10$, without PVC tubes) and displacement-width curves for cracks. The values of crack width are measured at the level of reinforcements.

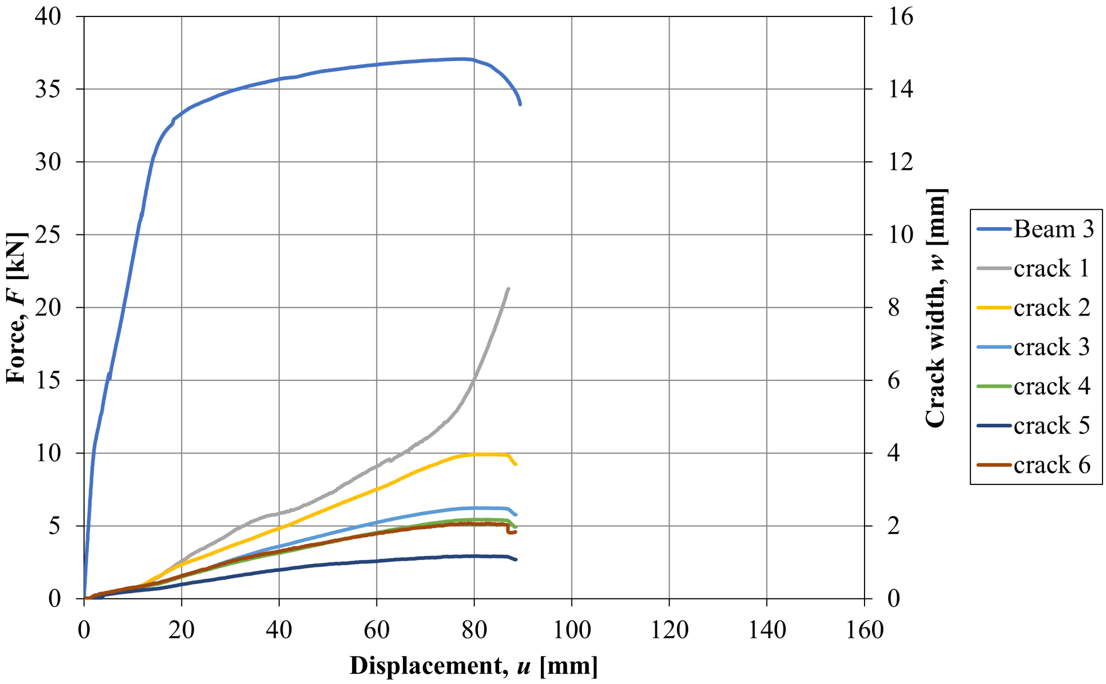

Figure C.3 Load-displacement curve for beam 3 ($\phi 10$, without PVC tubes) and displacement-width curves for cracks. The values of crack width are measured at the level of reinforcements.

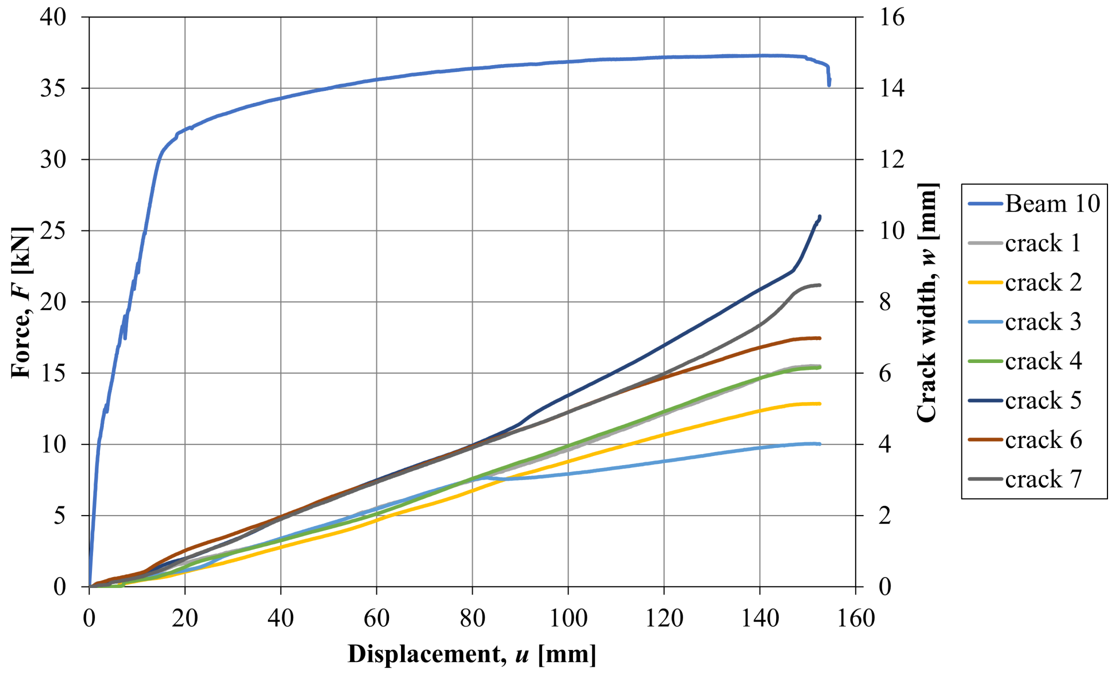

Figure C.4 *Load-displacement curve for beam 10 (ϕ10, without PVC tubes) and displacement-width curves for cracks. The values of crack width are measured at the level of reinforcements.*

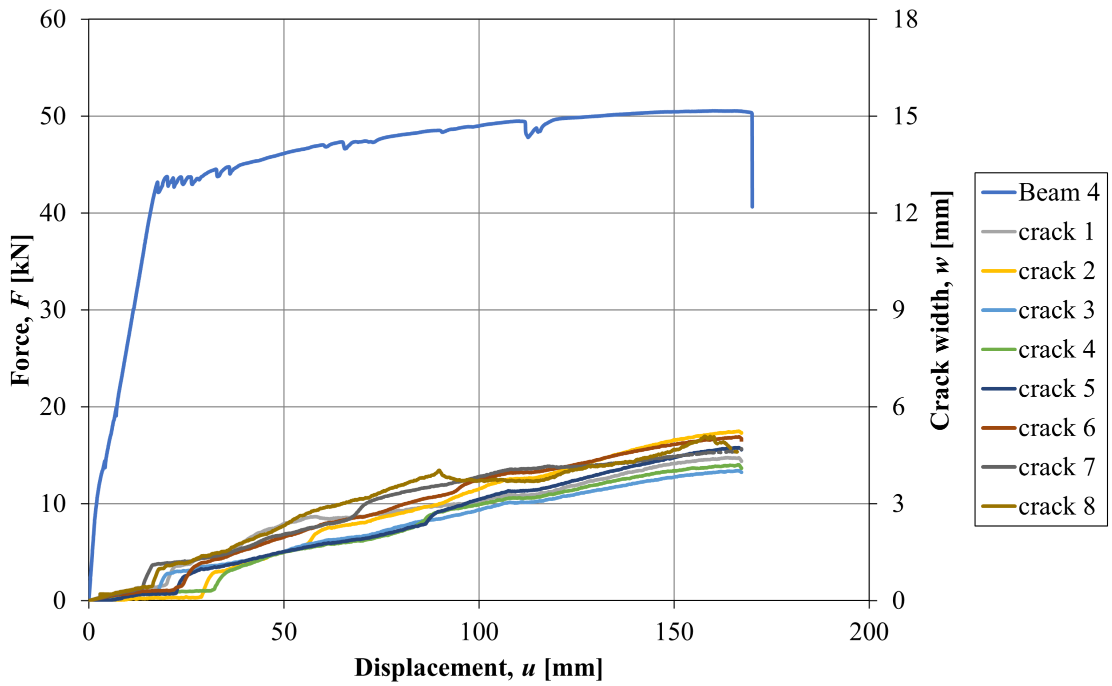

Figure C.5 *Load-displacement curve for beam 4 (ϕ12, without PVC tubes) and displacement-width curves for cracks. The values of crack width are measured at the level of reinforcements.*

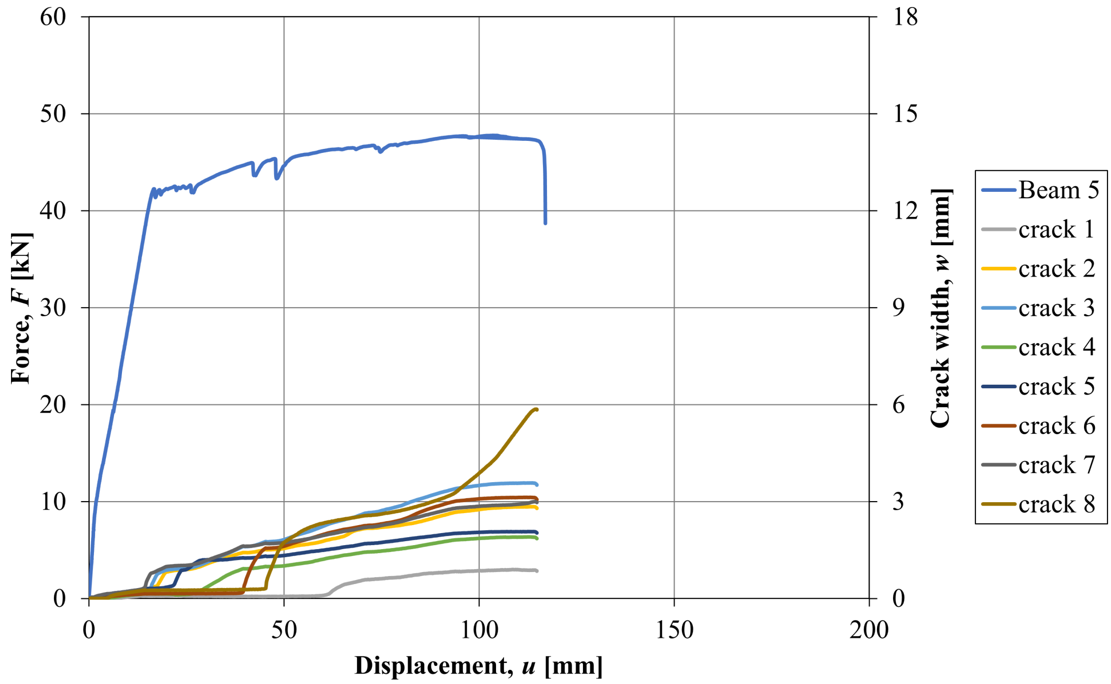

Figure C.6 *Load-displacement curve for beam 5 (ϕ12, without PVC tubes) and displacement-width curves for cracks. The values of crack width are measured at the level of reinforcements.*

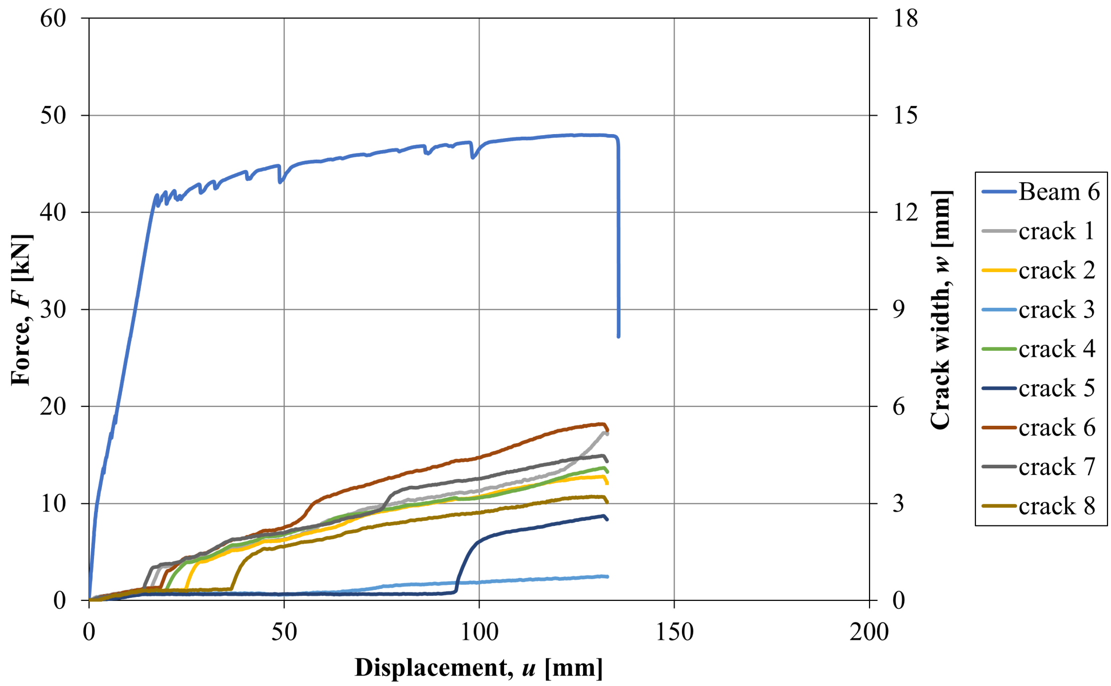

Figure C.7 *Load-displacement curve for beam 6 (ϕ12, without PVC tubes) and displacement-width curves for cracks. The values of crack width are measured at the level of reinforcements.*

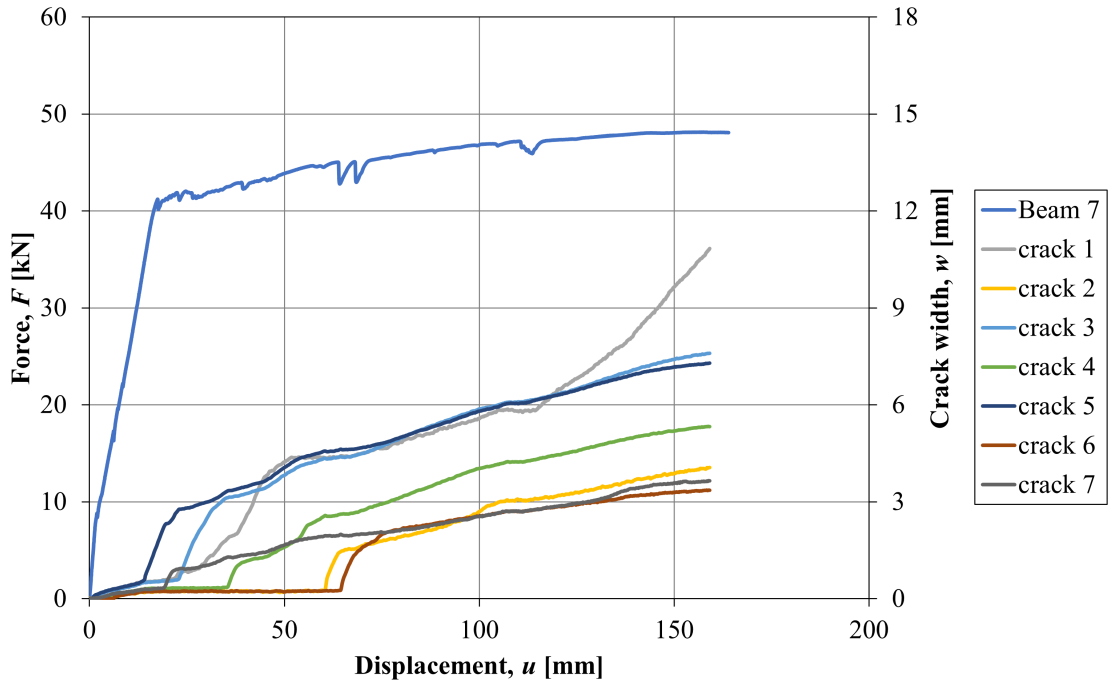

Figure C.8 *Load-displacement curve for beam 7 (ϕ12, with PVC tubes) and displacement-width curves for cracks. The values of crack width are measured at the level of reinforcements.*

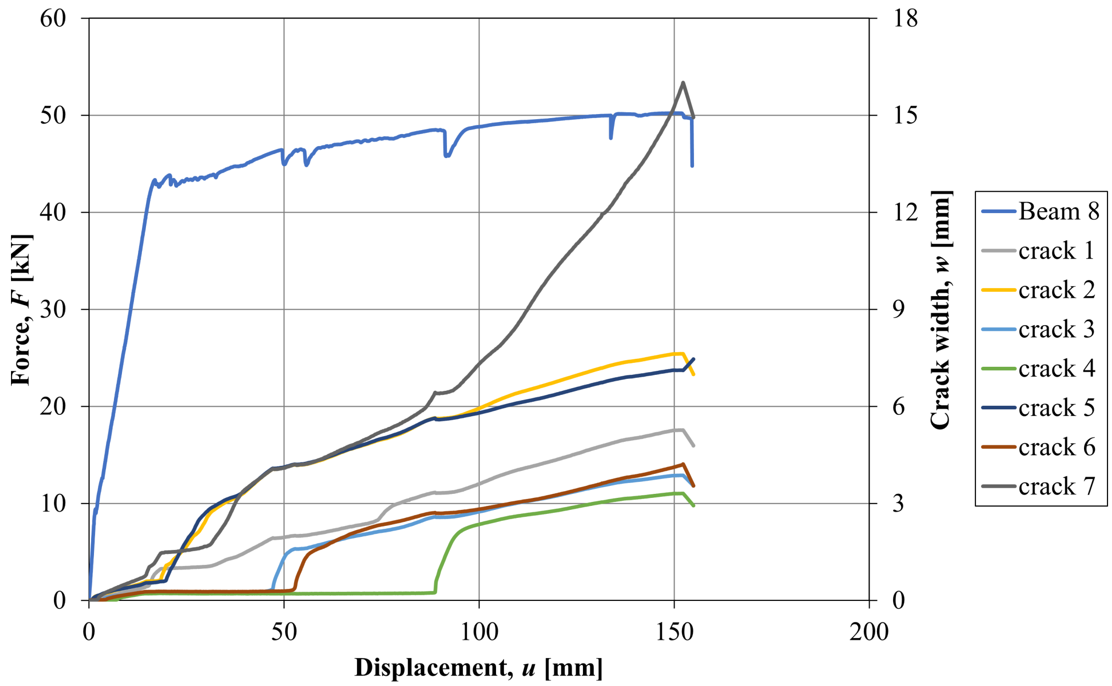

Figure C.9 *Load-displacement curve for beam 8 (ϕ12, with PVC tubes) and displacement-width curves for cracks. The values of crack width are measured at the level of reinforcements.*

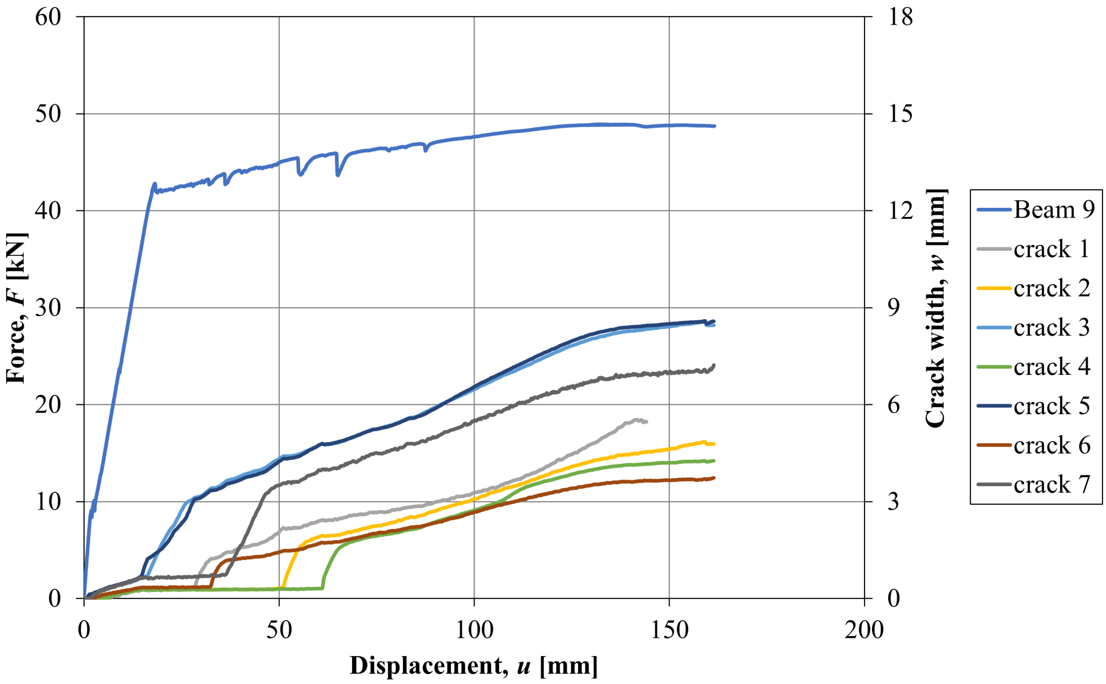

Figure C.10 *Load-displacement curve for beam 9 (ϕ12, with PVC tubes) and displacement-width curves for cracks. The values of crack width are measured at the level of reinforcements.*

C.2 Symmetrical behavior

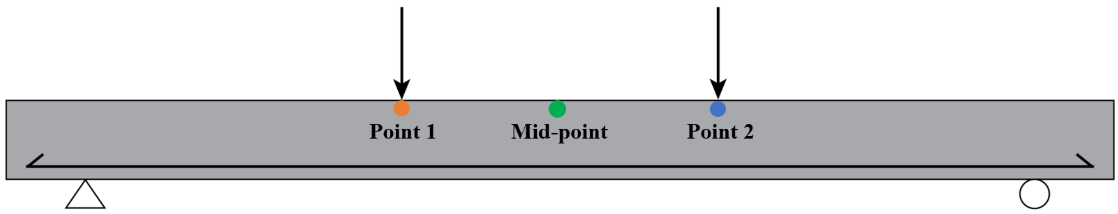

Figure C.11 *Illustration of mid-point, point 1, and point 2 for which displacement-time curves are provided.*

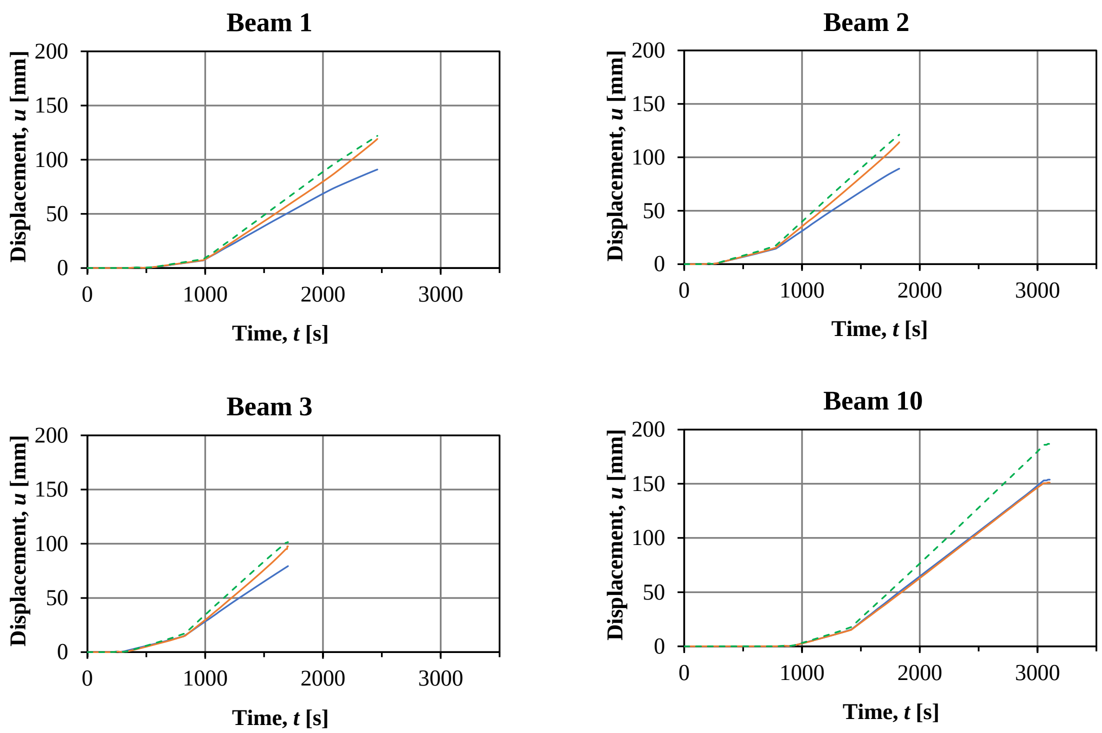

Figure C.12 *Displacement-time curve under loading points and mid-point for beams with ϕ10 reinforcement. The data for mid-point, point 1, and point 2 is shown by green dash-line, blue, and orange line, respectively.*

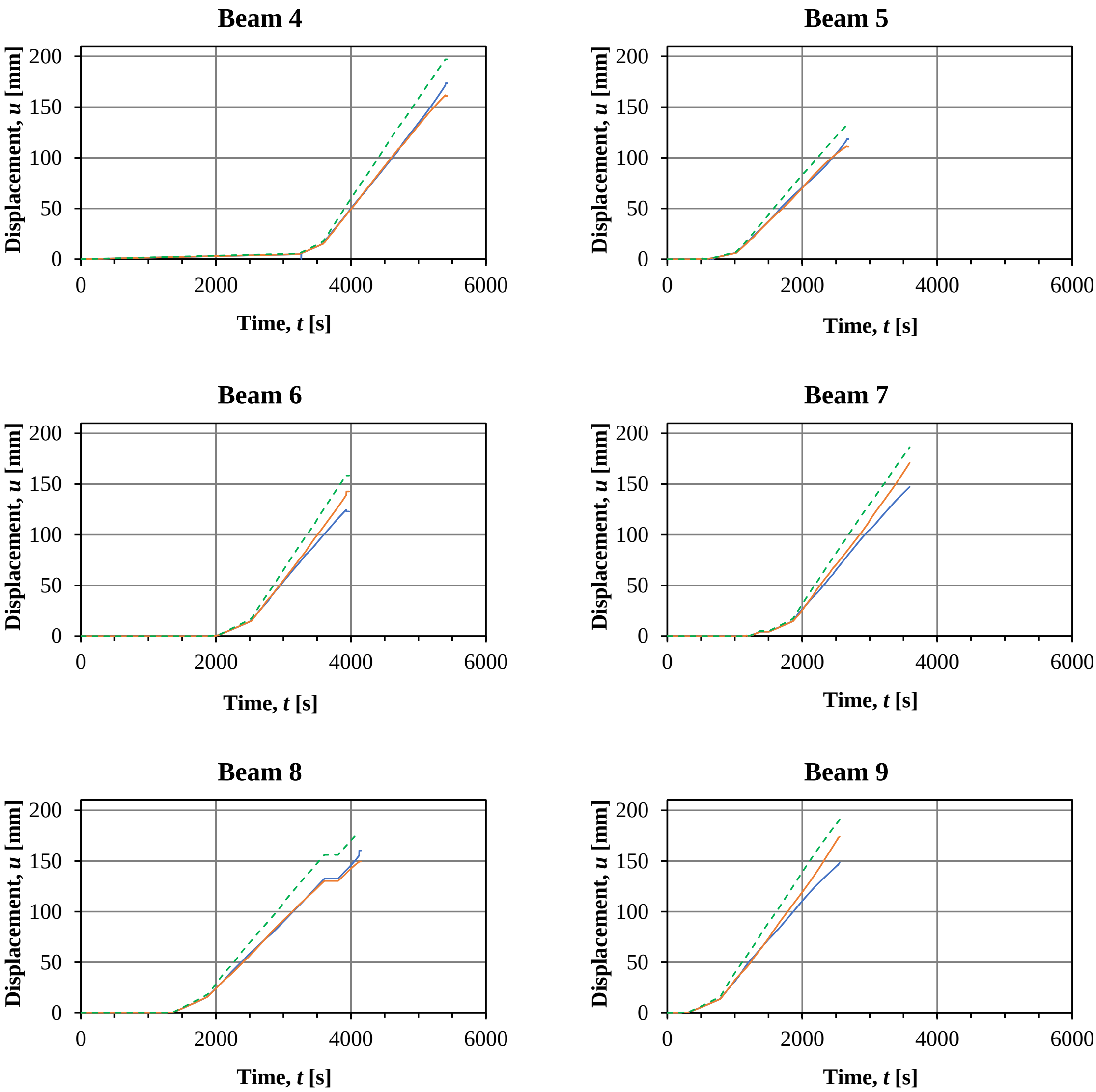

Figure C.13 *Displacement-time curve under loading points and mid-point for beams with ϕ12 reinforcement. The data for mid-point, point 1, and point 2 is shown by green dash-line, blue, and orange line, respectively.*

C.3 Crack pattern

Beam 1

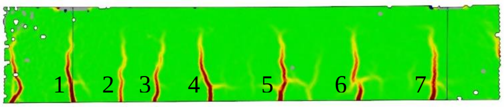

Yielding of reinforcement

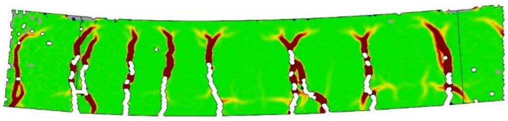

Maximum load

Beam 2

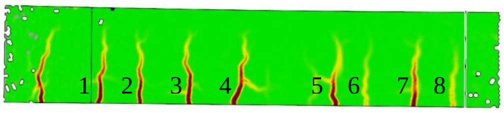

Yielding of reinforcement

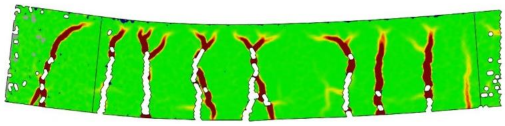

Maximum load

Beam 3

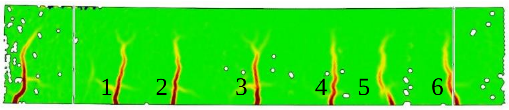

Yielding of reinforcement

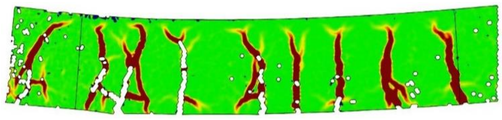

Maximum load

Beam 10

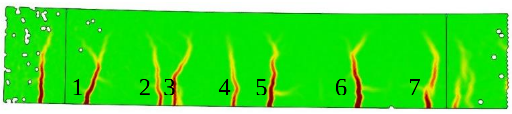

Yielding of reinforcement

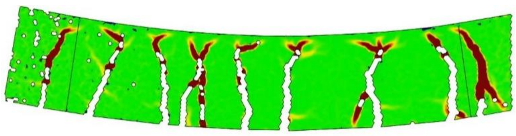

Maximum load

Figure C.14 Crack pattern of beams with ϕ10 reinforcement.

Beam 4

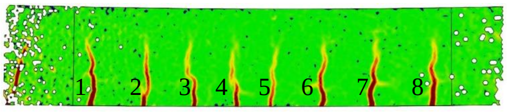

Yielding of reinforcement

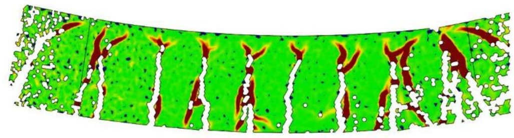

Maximum load

Beam 5

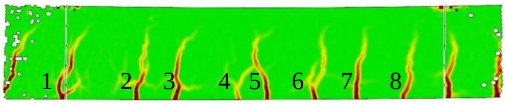

Yielding of reinforcement

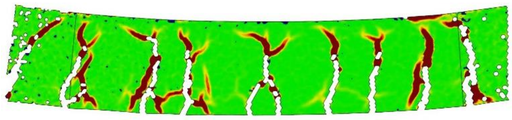

Maximum load

Beam 6

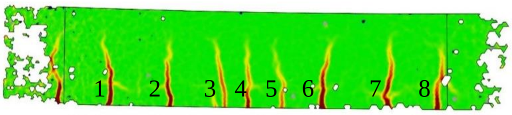

Yielding of reinforcement

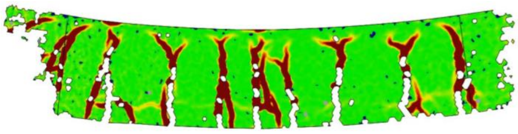

Maximum load

Figure C.15 Crack pattern of beams with ϕ12 reinforcement.

Beam 7

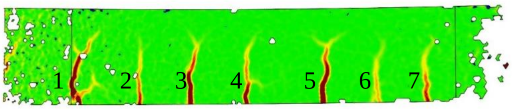

Yielding of reinforcement

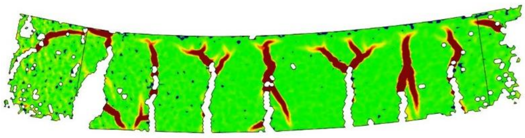

Maximum load

Beam 8

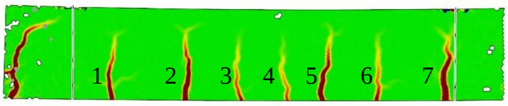

Yielding of reinforcement

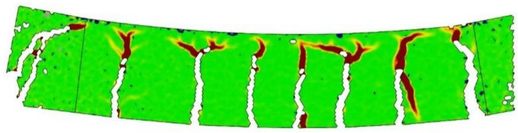

Maximum load

Beam 9

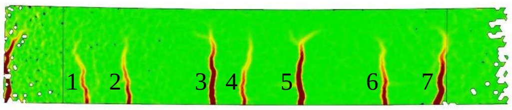

Yielding of reinforcement

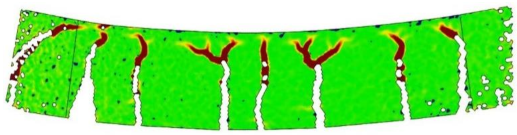

Maximum load

Figure C.16   Crack pattern of beams with $\phi 12$ reinforcement and PVC tubes.

C.4 Final image of beam at end of test

Figure C.17 Image of beam 1 at end of test.

Figure C.18 Image of beam 2 at end of test.

Figure C.19 Image of beam 3 at end of test.

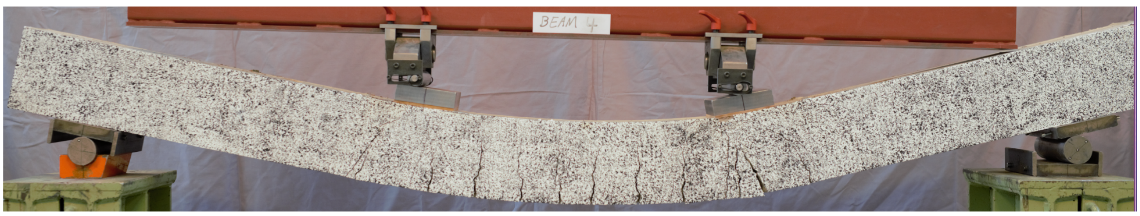

Figure C.20 Image of beam 4 at end of test.

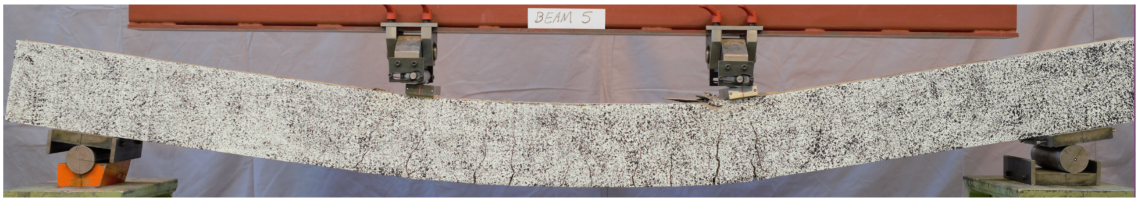

Figure C.21 Image of beam 5 at end of test.

Figure C.22 Image of beam 6 at end of test.

Figure C.23 Image of beam 7 at end of test.

Figure C.24 Image of beam 8 at end of test.

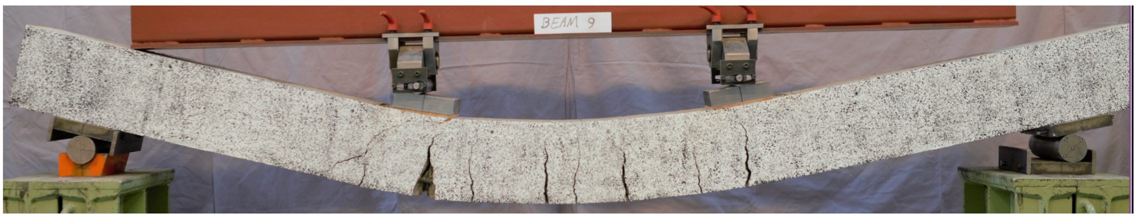

Figure C.25 Image of beam 9 at end of test.

Figure C.26   Image of beam 10 at end of test.

C.5 Determination of plastic rotation capacity

Table C.1 contains plastic rotational capacity and its relevant values for all tested beams. Parameters u_{el}, u_u, and u_{pl} are estimated from load-displacement graph of each beam as shown in schematic Figure 7.20. The parameter l_0 is equal to 800 mm for all beams. Plastic rotational capacity is calculated based on equations in Section 3.3.1.

Table C.1 Estimated parameter of plastic rotation capacity for all tested beams corresponding to F_{max} and $95\%F_{max}$. Displacement values are in [mm] and rotation values are in [mrad].

Beam no.	$u_{el,95\%}$	$u_{u,95\%}$	$u_{pl,95\%}$	$\theta_{pl,95\%}$	$u_{el,100\%}$	$u_{u,100\%}$	$u_{pl,100\%}$	$\theta_{pl,100\%}$
1	16.3	103.4	87.1	109	15.5	81.1	65.6	82
2	17.9	103.4	85.5	107	18.7	93.0	74.3	93
3	16.8	87.7	70.9	89	17.5	78.0	60.5	76
10	18.0	154.5	136.5	171	19.3	140.6	121.3	152
4	19.5	170.0	150.5	188	20.5	160.5	140.0	175
5	17.5	116.7	99.2	124	18.8	103.4	84.6	106
6	19.0	135.5	116.5	146	20.0	126.3	106.3	133
7	19.0	164.6	145.6	182	20.6	164.6	144.0	180
8	18.5	154.5	136.0	170	19.4	149.2	129.8	162
9	20.0	161.5	141.5	177	21.0	131.8	110.8	139

C.6 Calculation of plastic rotation capacity based on BK 25 and German method

C.6.1 BK 25

$b := 0.2\ m$ $\quad h := b = 0.2\ m$ $\quad c := 40\ mm$ $\quad d := h - c = 0.16\ m$

$l := 2.4\ m$ $\quad \varepsilon_{cu} := 0.35\%$ $\quad f_c := 56\ MPa$

For beams with ϕ10 reinforcement:

$f_y := 564\ MPa$ $\quad f_u := 656\ MPa$ $\quad \varphi := 10\ mm$ $\quad \varepsilon_{su} := 2.29\%$

$$A_s := 2 \cdot \frac{\pi \cdot \varphi^2}{4} = \left(1.571 \cdot 10^{-4}\right)\ m^2 \qquad \rho_s := \frac{A_s}{b \cdot d} = 0.005$$

$$\omega_s := \rho_s \cdot \frac{f_u}{f_c} = 0.058 \qquad \theta_{pl} := \frac{0.4 \cdot \varepsilon_{su}}{0.8 - \omega_s} \cdot \left(1 + 0.3 \cdot \frac{l}{d}\right) = 0.068\ rad$$

For beams with ϕ10 reinforcement:

$f_y := 535\ MPa$ $\quad f_u := 622\ MPa$ $\quad \varphi := 12\ mm$ $\quad \varepsilon_{su} := 3.73\%$

$$A_s := 2 \cdot \frac{\pi \cdot \varphi^2}{4} = \left(2.262 \cdot 10^{-4}\right)\ m^2 \qquad \rho_s := \frac{A_s}{b \cdot d} = 0.007$$

$$\omega_s := \rho_s \cdot \frac{f_y}{f_c} = 0.068 \qquad \theta_{pl} := \frac{0.4 \cdot \varepsilon_{cu}}{0.8\ \omega_s} \cdot \left(1 + 0.3 \cdot \frac{l}{d}\right) = 0.143\ rad$$

C.6.2 German Method

$\beta_n := 22.5$ $\beta_{cd} := \left(\frac{0.0035}{\varepsilon_{cu}}\right)^3 = 1$ $l_0 := 0.8\ \boldsymbol{m}$ $\lambda := \frac{l_0}{d} = 5$ $\alpha_R := 0.81$

For beams with ϕ10 reinforcement:

$f_y := 564\ \boldsymbol{MPa}$ $f_u := 656\ \boldsymbol{MPa}$ $\varphi := 10\ \boldsymbol{mm}$ $E_s := 198\ \boldsymbol{GPa}$ $\varepsilon_{su} := 6.4\%$

$A_s := 2 \cdot \frac{\pi \cdot \varphi^2}{4} = \left(1.571 \cdot 10^{-4}\right)\ \boldsymbol{m}^2$ $\varepsilon_{sy} := \frac{f_y}{E_s} = 0.003$ $\beta_s := 1 - \frac{f_y}{f_u} = 0.14$

$x := \frac{f_y \cdot A_s}{b \cdot \alpha_R \cdot f_c} = 0.01\ \boldsymbol{m}$ $\frac{x}{d} = 0.061$

$\varepsilon_{su.s} := 0.28 \cdot \left(\beta_{cd} \cdot \frac{x}{d}\right)^{0.2} \cdot \varepsilon_{su} = 0.01$ $\varepsilon_{su.c} := -1.75 \cdot \left(\frac{x}{d}\right)^{\frac{2}{3}} \cdot \left(1 - \left(\frac{x}{d}\right)^{-1}\right) \cdot \varepsilon_{cu} = 0.015$

$\varepsilon_{su.star} := min\left(\varepsilon_{su.s}, \varepsilon_{su.c}\right) = 0.01$

$\theta_{pl.EC} := \beta_n \cdot \beta_s \cdot \frac{\varepsilon_{su.star} - \varepsilon_{sy}}{1 - \frac{x}{d}} \cdot \sqrt{\frac{\lambda}{3}} = 0.032\ \boldsymbol{rad}$ $\theta_{pl} := \frac{\theta_{pl.EC}}{2} = 0.016\ \boldsymbol{rad}$

For beams with ϕ 12 reinforcement:

$f_y := 535\ MPa$ $\quad f_u := 622\ MPa$ $\quad \varphi := 12\ mm$ $\quad E_s := 191\ GPa$ $\quad \varepsilon_{su} := 9.0\%$

$$A_s := 2 \cdot \frac{\pi \cdot \varphi^2}{4} = \left(2.262 \cdot 10^{-4}\right)\ m^2 \qquad \varepsilon_{sy} := \frac{f_y}{E_s} = 0.003 \qquad \beta_s := 1 - \frac{f_y}{f_u} = 0.14$$

$$x := \frac{f_y \cdot A_s}{b \cdot \alpha_R \cdot f_c} = 0.013\ m \qquad \frac{x}{d} = 0.083$$

$$\varepsilon_{su.s} := 0.28 \cdot \left(\beta_{cd} \cdot \frac{x}{d}\right)^{0.2} \cdot \varepsilon_{su} = 0.015 \qquad \varepsilon_{su.c} := -1.75 \cdot \left(\frac{x}{d}\right)^{\frac{2}{3}} \cdot \left(1 - \left(\frac{x}{d}\right)^{-1}\right) \cdot \varepsilon_{cu} = 0.013$$

$$\varepsilon_{su.star} := min\left(\varepsilon_{su.s}, \varepsilon_{su.c}\right) = 0.013$$

$$\theta_{pl.EC} := \beta_n \cdot \beta_s \cdot \frac{\varepsilon_{su.star} - \varepsilon_{sy}}{1 - \frac{x}{d}} \cdot \sqrt{\frac{\lambda}{3}} = 0.045\ rad \qquad \theta_{pl} := \frac{\theta_{pl.EC}}{2} = 0.022\ rad$$

D Plastic reinforcement strain

D.1 Plastic strain measurements

The results from the strain measurements are presented in Figures D.1- D.9. An explanation of the notations in the following bar charts is presented in Section 7.4 together with a summary of the average plastic strain results. For the beams with PVC tubes, Figures D.7- D.9, the position of the tubes is marked with a shaded area.

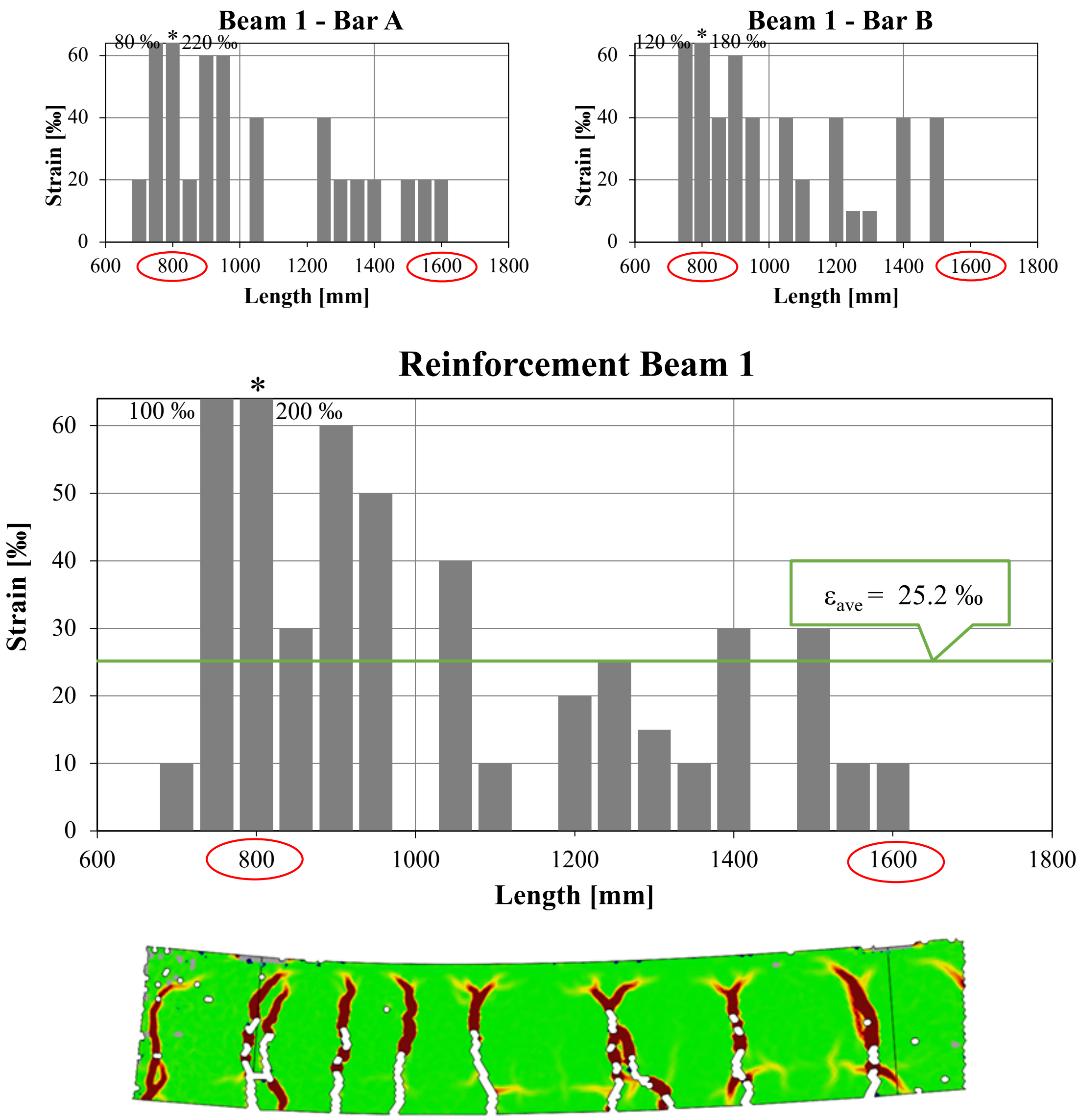

Figure D.1 Plastic reinforcement strain measurements for each reinforcement bar (upper charts), the average strain of the two bars (middle chart) and the crack pattern figure from DIC for beam 1.

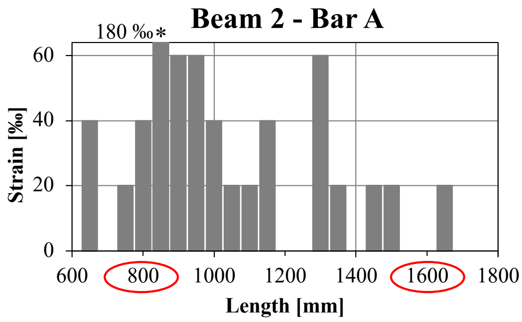

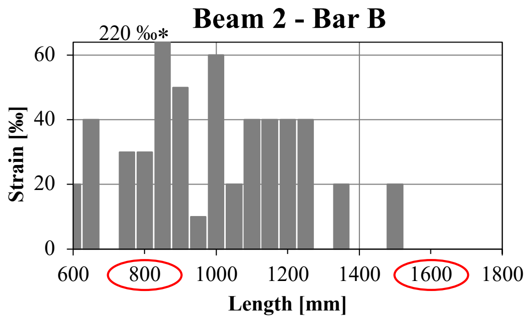

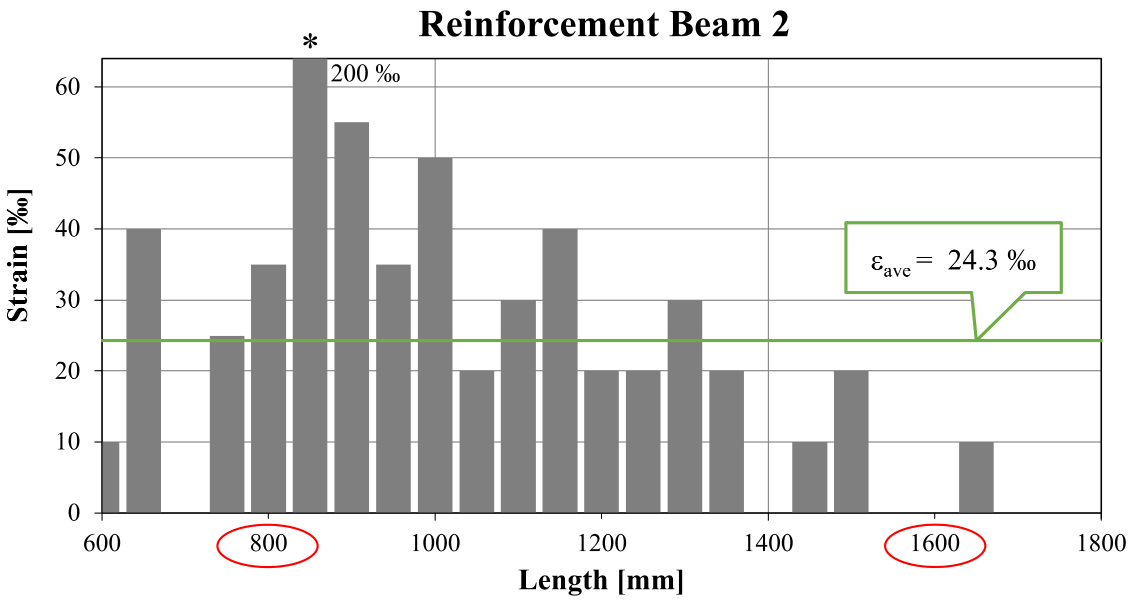

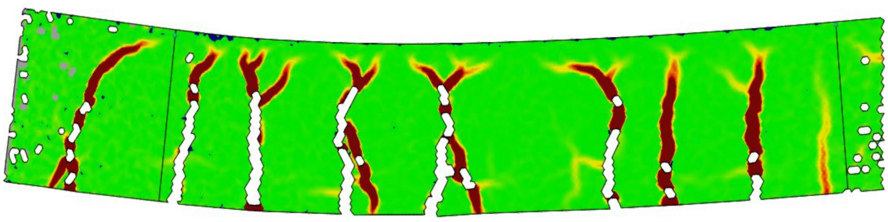

Figure D.2 *Plastic reinforcement strain measurements for each reinforcement bar (upper charts), the average strain of the two bars (middle chart) and the crack pattern figure from DIC for beam 2.*

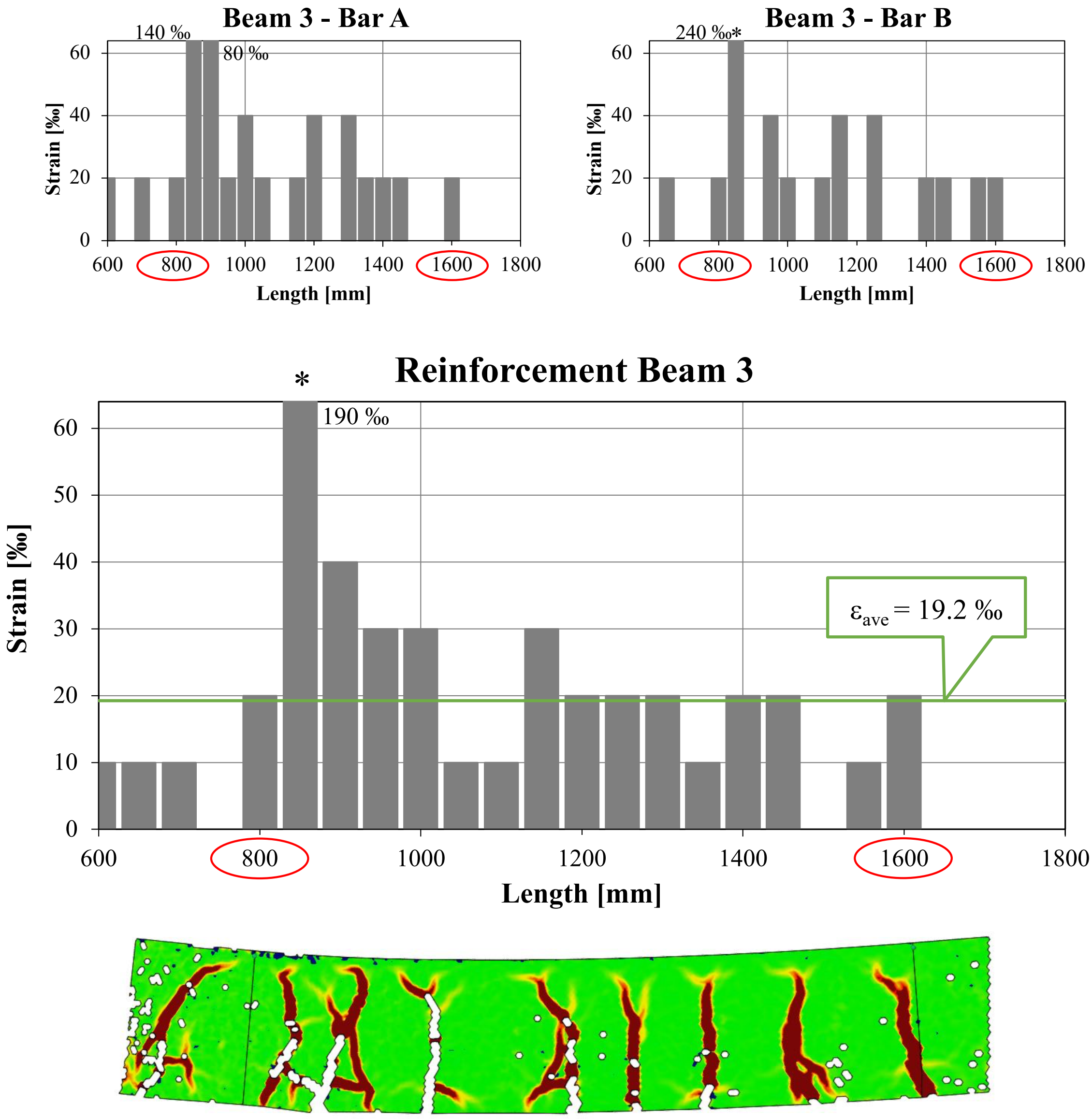

Figure D.3 *Plastic reinforcement strain measurements for each reinforcement bar (upper charts), the average strain of the two bars (middle chart) and the crack pattern figure from DIC for beam 3.*

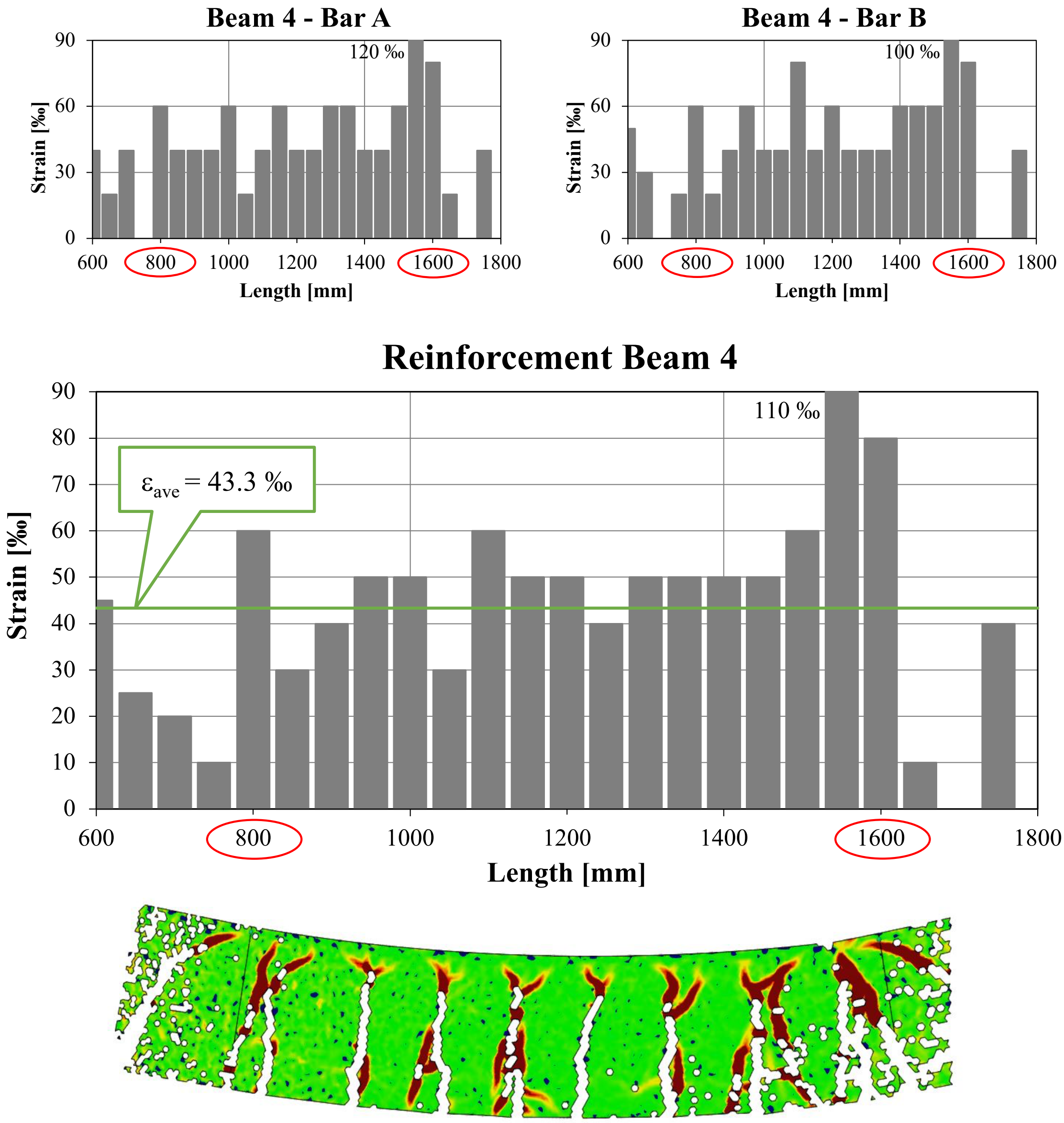

Figure D.4 *Plastic reinforcement strain measurements for each reinforcement bar (upper charts), the average strain of the two bars (middle chart) and the crack pattern figure from DIC for beam 4.*

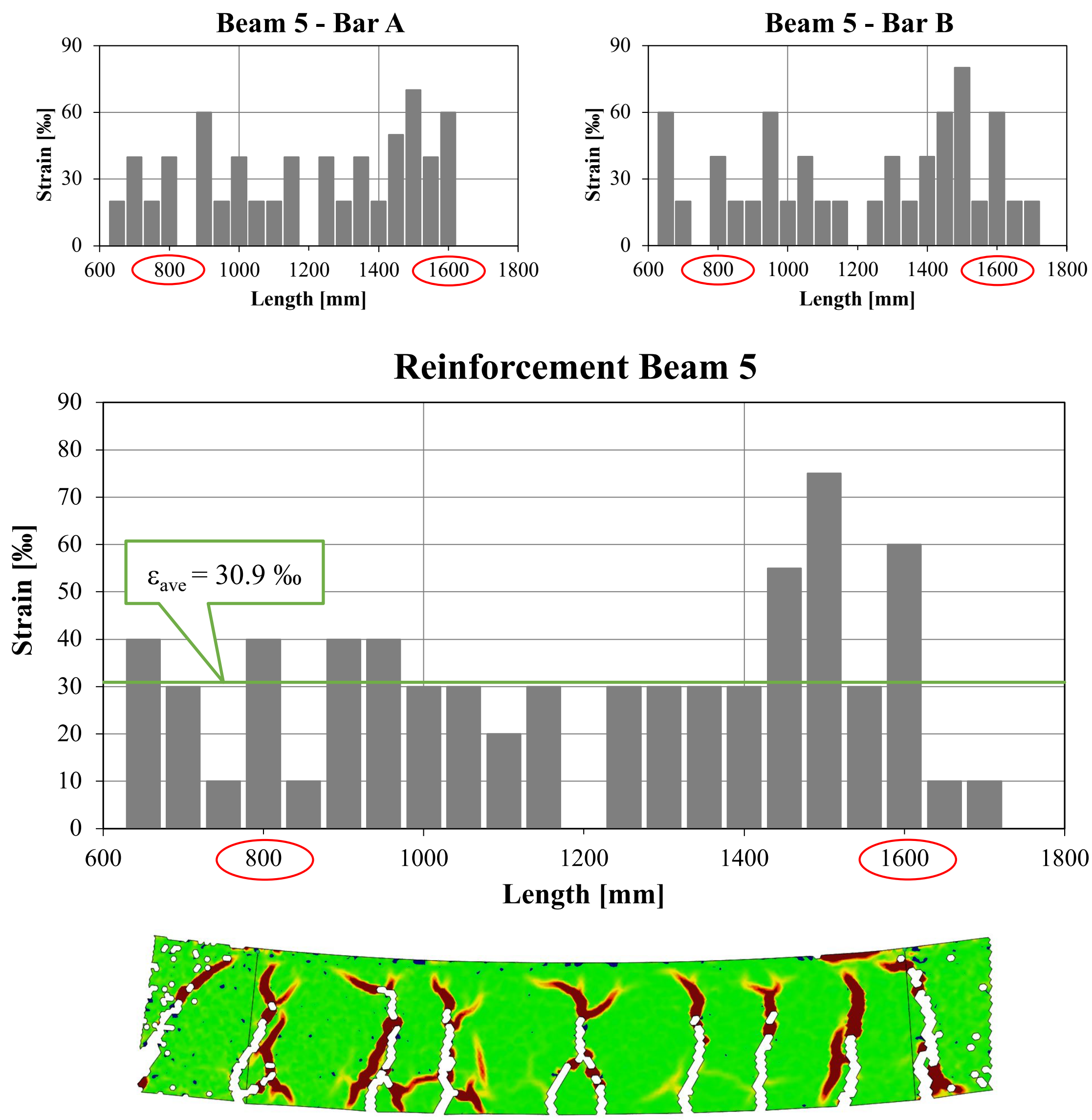

Figure D.5 *Plastic reinforcement strain measurements for each reinforcement bar (upper charts), the average strain of the two bars (middle chart) and the crack pattern figure from DIC for beam 5.*

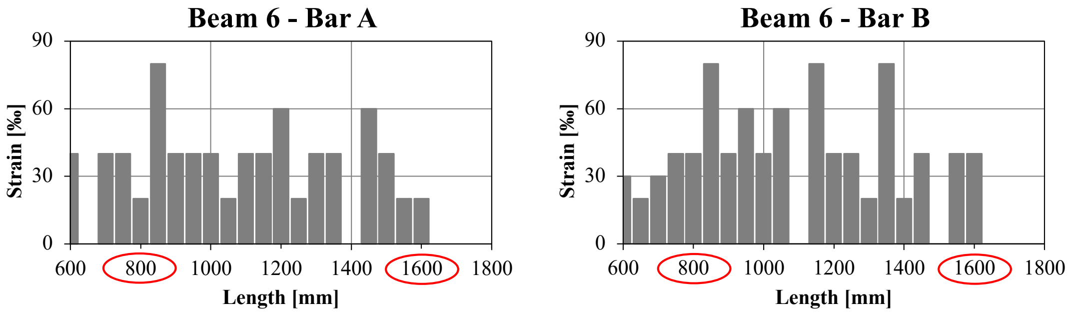

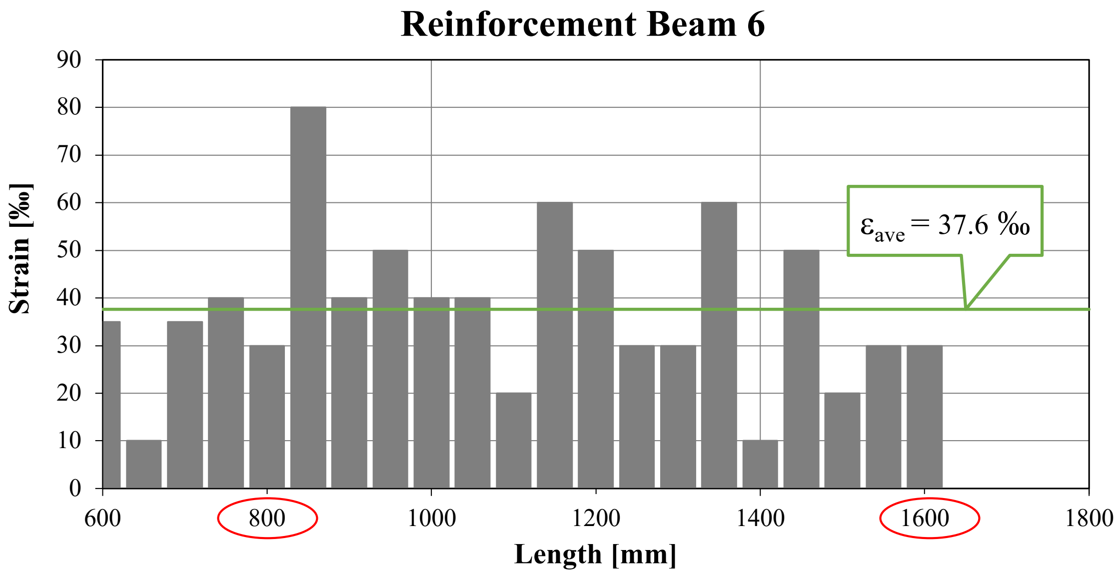

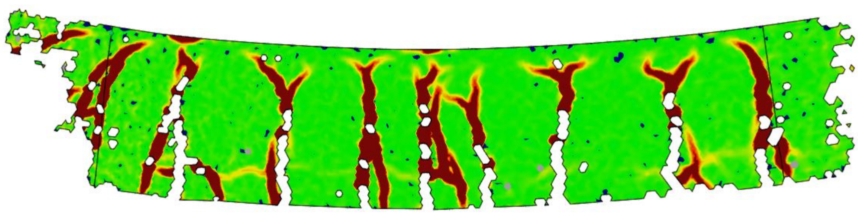

Figure D.6   Plastic reinforcement strain measurements for each reinforcement bar (upper charts), the average strain of the two bars (middle chart) and the crack pattern figure from DIC for beam 6.

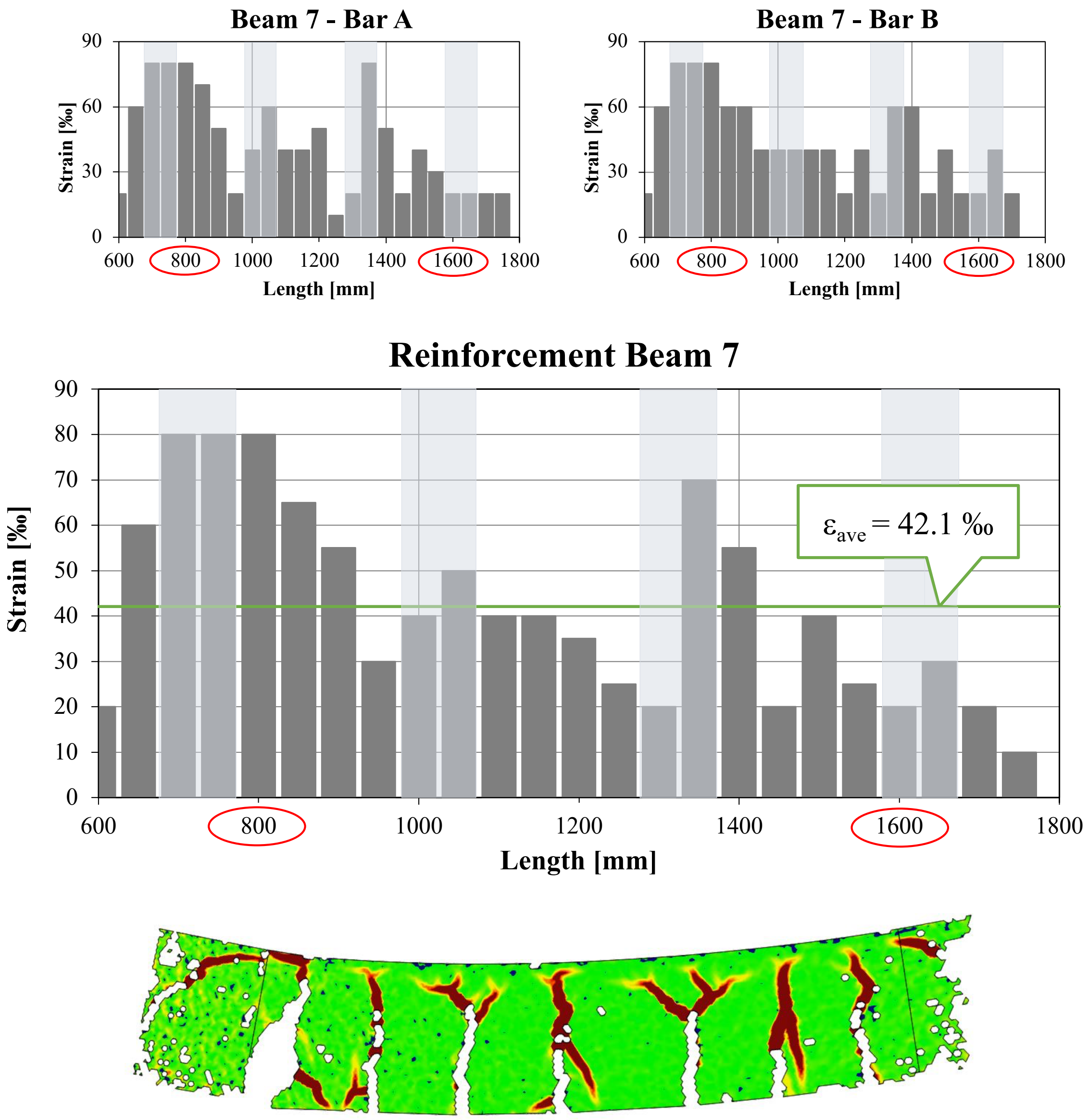

Figure D.7 *Plastic reinforcement strain measurements for each reinforcement bar (upper charts), the average strain of the two bars (middle chart) and the crack pattern figure from DIC for beam 7.*

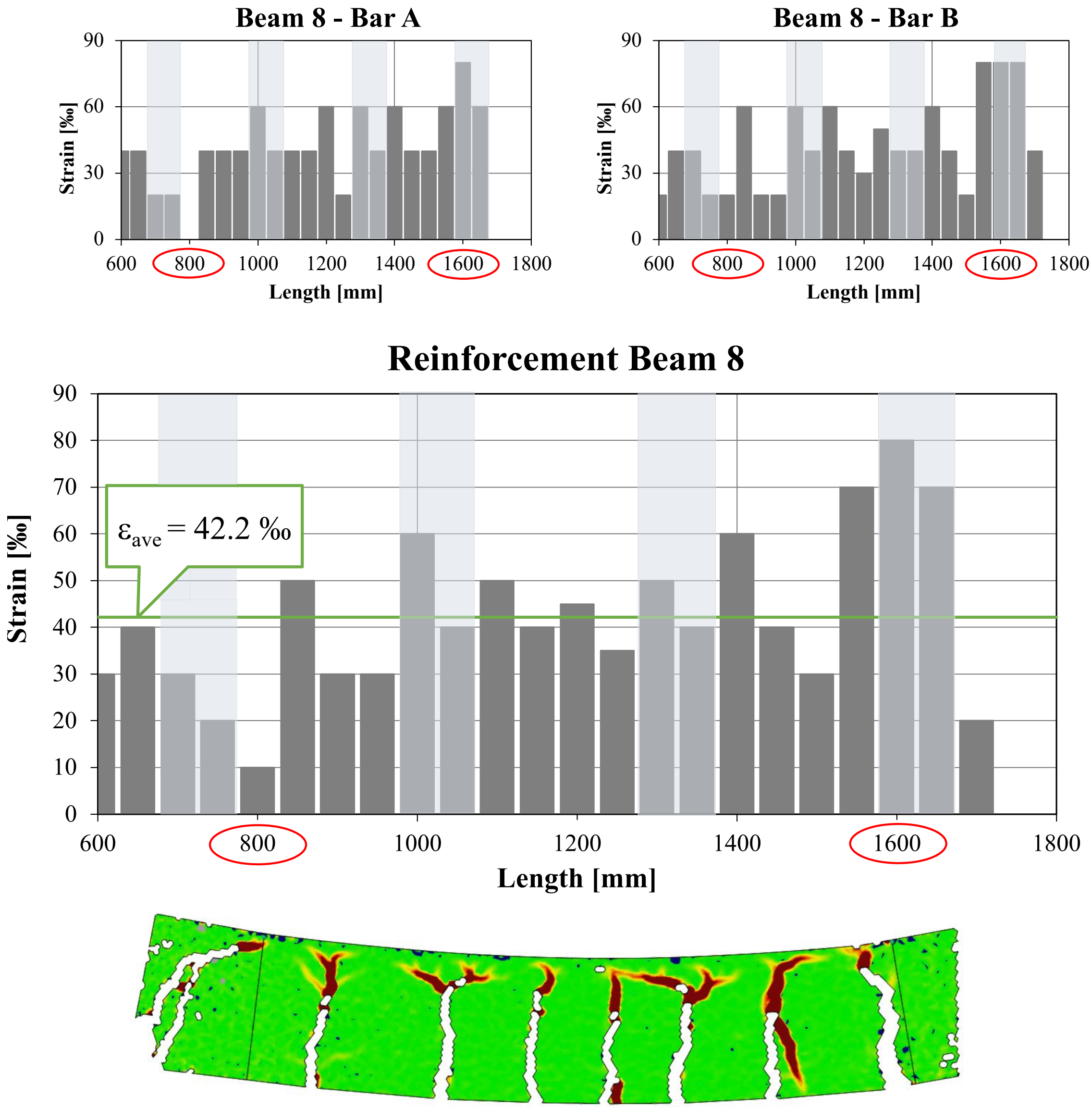

Figure D.8 *Plastic reinforcement strain measurements for each reinforcement bar (upper charts), the average strain of the two bars (middle chart) and the crack pattern figure from DIC for beam 8.*

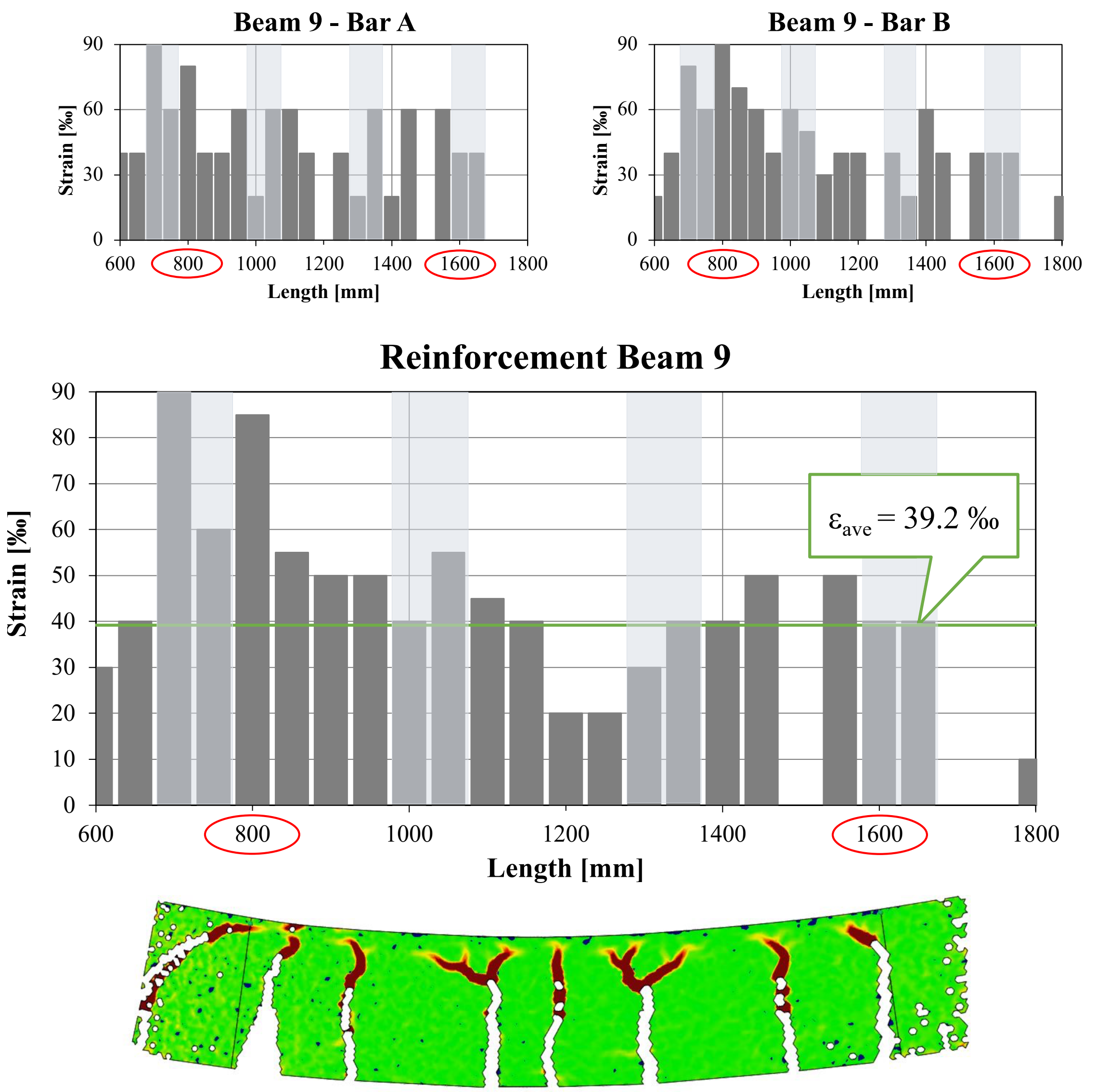

Figure D.9 *Plastic reinforcement strain measurements for each reinforcement bar (upper charts), the average strain of the two bars (middle chart) and the crack pattern figure from DIC for beam 9.*

Table D.1 Calculated strains for each reinforcement bar from elongation measurements. The x-coordinates are presented in mm and the strains in ‰.

	Beam 1		Beam 2		Beam 3		Beam 4		Beam 5		Beam 6		Beam 7		Beam 8		Beam 9	
x	A	B	A	B	A	B	A	B	A	B	A	B	A	B	A	B	A	B
600	0	0	0	20	20	0	40	50	0	0	40	30	20	20	40	20	40	20
650	0	0	40	40	0	20	20	30	20	60	0	20	60	60	40	40	40	40
700	20	0	0	0	20	0	40	0	40	20	40	30	80	80	20	40	100	80
750	80	120	20	30	0	0	0	20	20	0	40	40	80	80	20	20	60	60
800	220	180	40	30	20	20	60	60	40	40	20	40	80	80	0	20	80	90
850	20	40	180	220	140	240	40	20	0	20	80	80	70	60	40	60	40	70
900	60	60	60	50	80	0	40	40	60	20	40	40	50	60	40	20	40	60
950	60	40	60	10	20	40	40	60	20	60	40	60	20	40	40	20	60	40
1000	0	0	40	60	40	20	60	40	40	20	40	40	40	40	60	60	20	60
1050	40	40	20	20	20	0	20	40	20	40	20	60	60	40	40	40	60	50
1100	0	20	20	40	0	20	40	80	20	20	40	0	40	40	40	60	60	30
1150	0	0	40	40	20	40	60	40	40	20	40	80	40	40	40	40	40	40
1200	0	40	0	40	40	0	40	60	0	0	60	40	50	20	60	30	0	40
1250	40	10	0	40	0	40	40	40	40	20	20	40	10	40	20	50	40	0
1300	20	10	60	0	40	0	60	40	20	40	40	20	20	20	60	40	20	40
1350	20	0	20	20	20	0	60	40	40	20	40	80	80	60	40	40	60	20
1400	20	40	0	0	20	20	40	60	20	40	0	20	50	60	60	60	20	60
1450	0	0	20	0	20	20	40	60	50	60	60	40	20	20	40	40	60	40
1500	20	40	20	20	0	0	60	60	70	80	40	0	40	40	40	20	0	0
1550	20	0	0	0	0	20	120	100	40	20	20	40	30	20	60	80	60	40
1600	20	0	0	0	20	20	80	80	60	60	20	40	20	20	80	80	40	40
1650	0	0	20	0	0	0	20	0	0	20	0	0	20	40	60	80	40	40
1700	0	0	0	0	0	0	0	0	0	20	0	0	20	20	0	40	0	0
1750	0	0	0	0	0	0	40	40	0	0	0	0	20	0	0	0	0	0
1800	0	0	0	0	0	0	0	0	0	0	0	0	0	0	0	0	0	20

D.2 3D scanning

The middle one meter of in total six bars were 3D scanned before the casting and after testing removed from the concrete and scanned again to measure the elongation. Data was extracted for every 50 mm segment as a point cloud mesh to evaluate the length of each bar segment. The procedure was done both for the first and second scanning. The first part of the appendix treats the 3D model and the second part the results from the scanning.

D.2.1 3D model

Before the second scanning, the bars were sandblasted to remove concrete residuals. However, the sandblasting made the surface more shiny which effected the resolution of the scanning since shiny surfaces are more difficult to scan and the marks were less visible, see Figure D.10 and Figure D.11. Those effects were more severe for the ϕ10 bars where some of the marks were not visible at all.

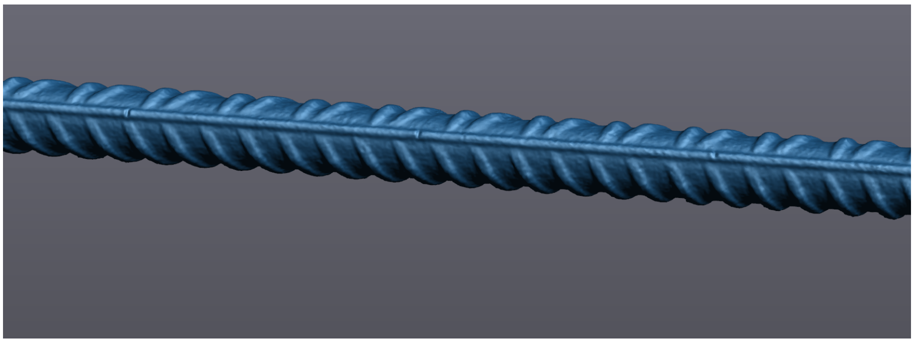

Figure D.10 Example of marks in the 3D model before casting for a ϕ12 bar.

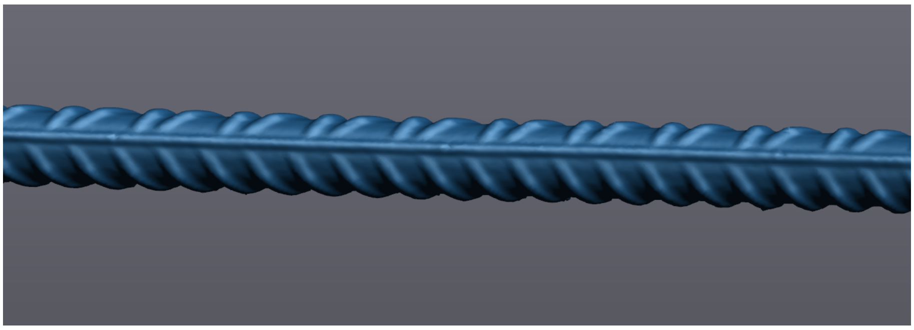

Figure D.11 Example of marks in the 3D model after casting and sandblasting for a ϕ12 bar.

Figure D.13 and Figure D.12 show examples of the 3D models for a ϕ10 bar and a ϕ12 bar, respectively, at the first and second scanning. Both ϕ10 bars were ruptured and steel plates were used as supports, and to capture the fractured area the scanning was made twice with two different configurations of the steel plates, see Figure D.14.

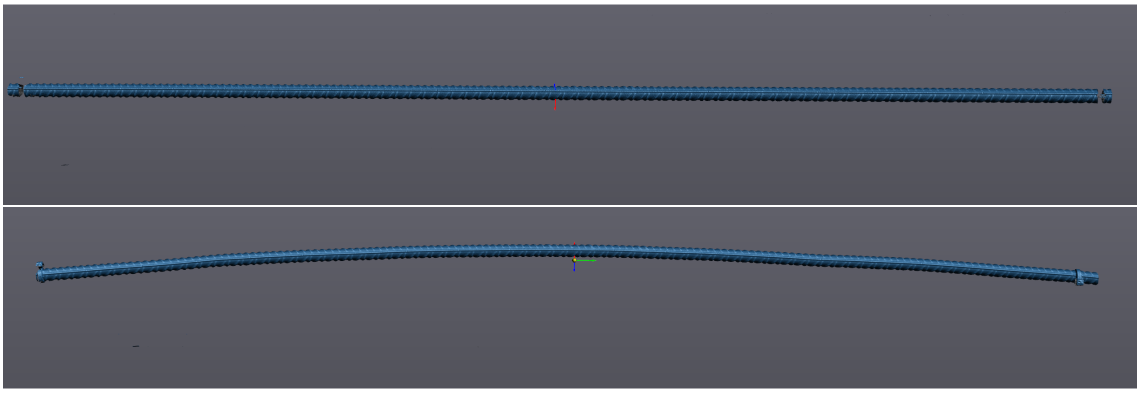

Figure D.12 Example of a ϕ12 bar 3D model before and after casting.

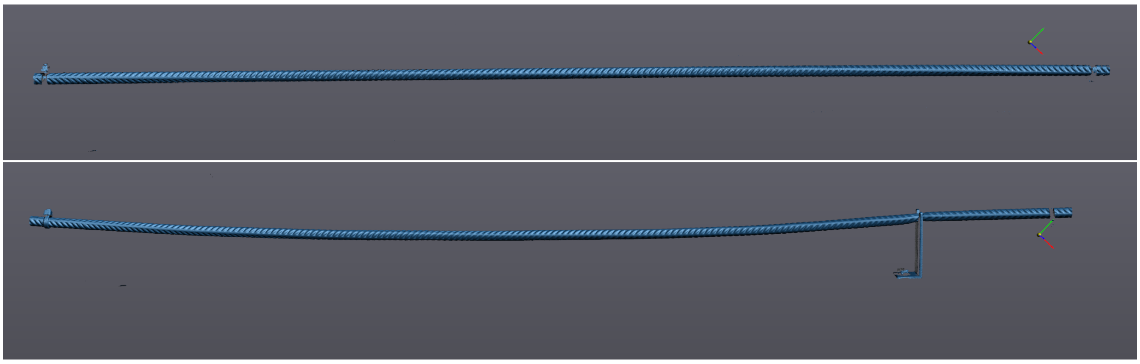

Figure D.13 Example of a ϕ10 bar 3D model before and after casting.

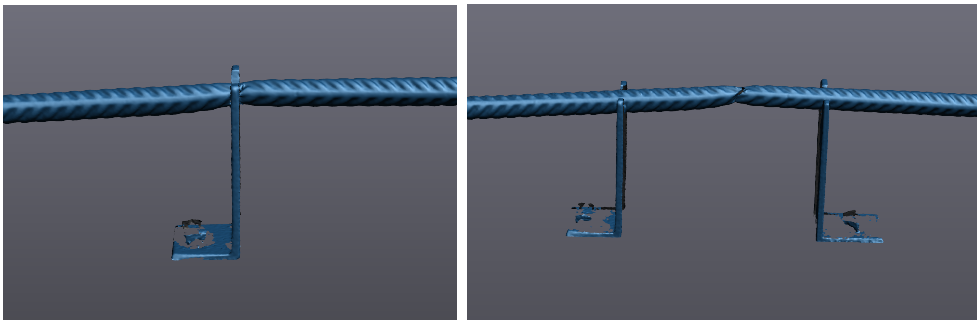

Figure D.14 The scanning of the rupture bars was made twice with two different configurations of supporting steel plates to scan the fractured area.

D.2.2 3D scanning results

The plastic strain results from the 3D scanning are presented in Figures D.15 - D.17. The results are presented as bar charts in the same way as the plastic strain measurements. An explanation of the notations in the following bar charts is presented in Section 7.4 together with a summary of the average plastic strain results from the 3D scanned bars.

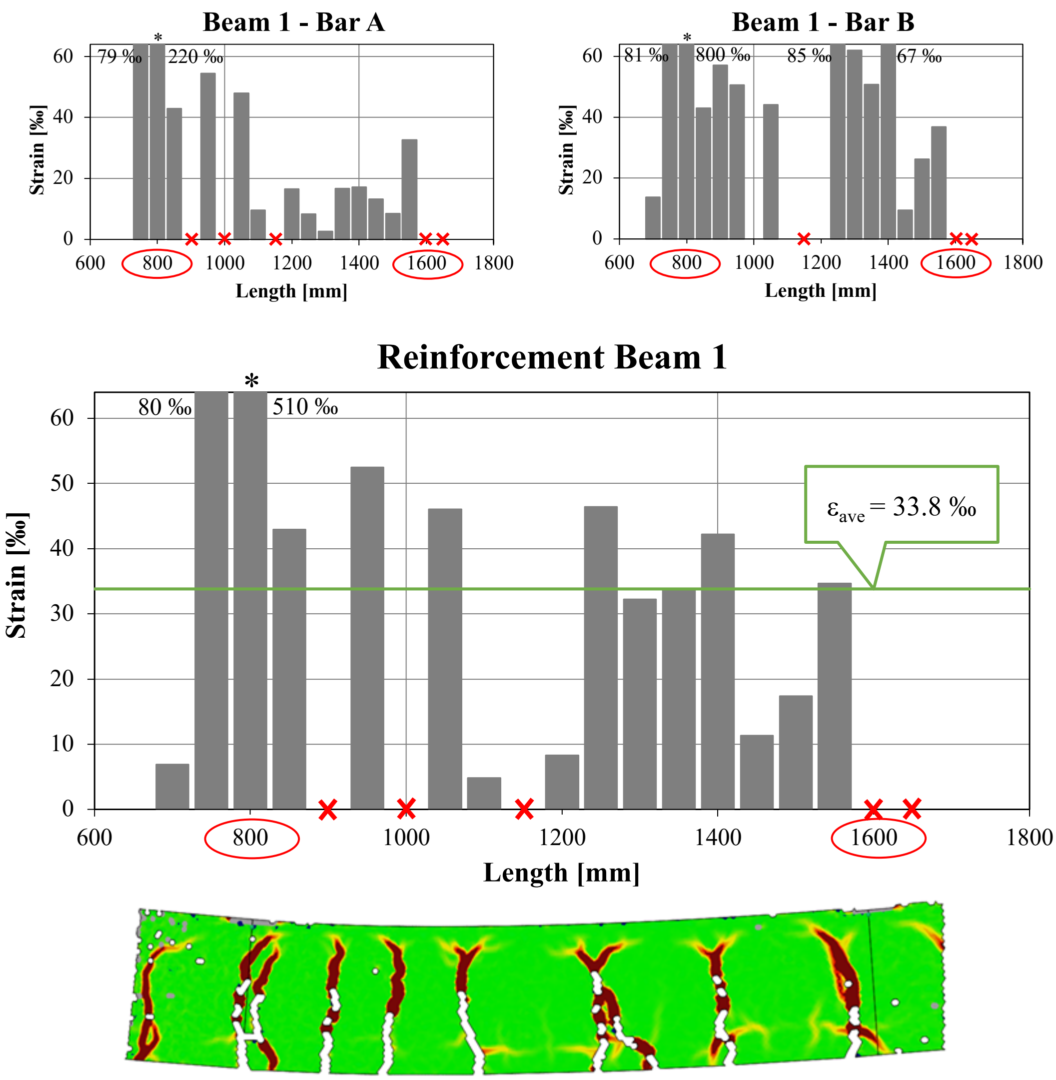

Figure D.15 *Plastic reinforcement strain measurements for each reinforcement bar (upper charts), the average strain of the two bars (middle chart) and the crack pattern figure from DIC for beam 1.*

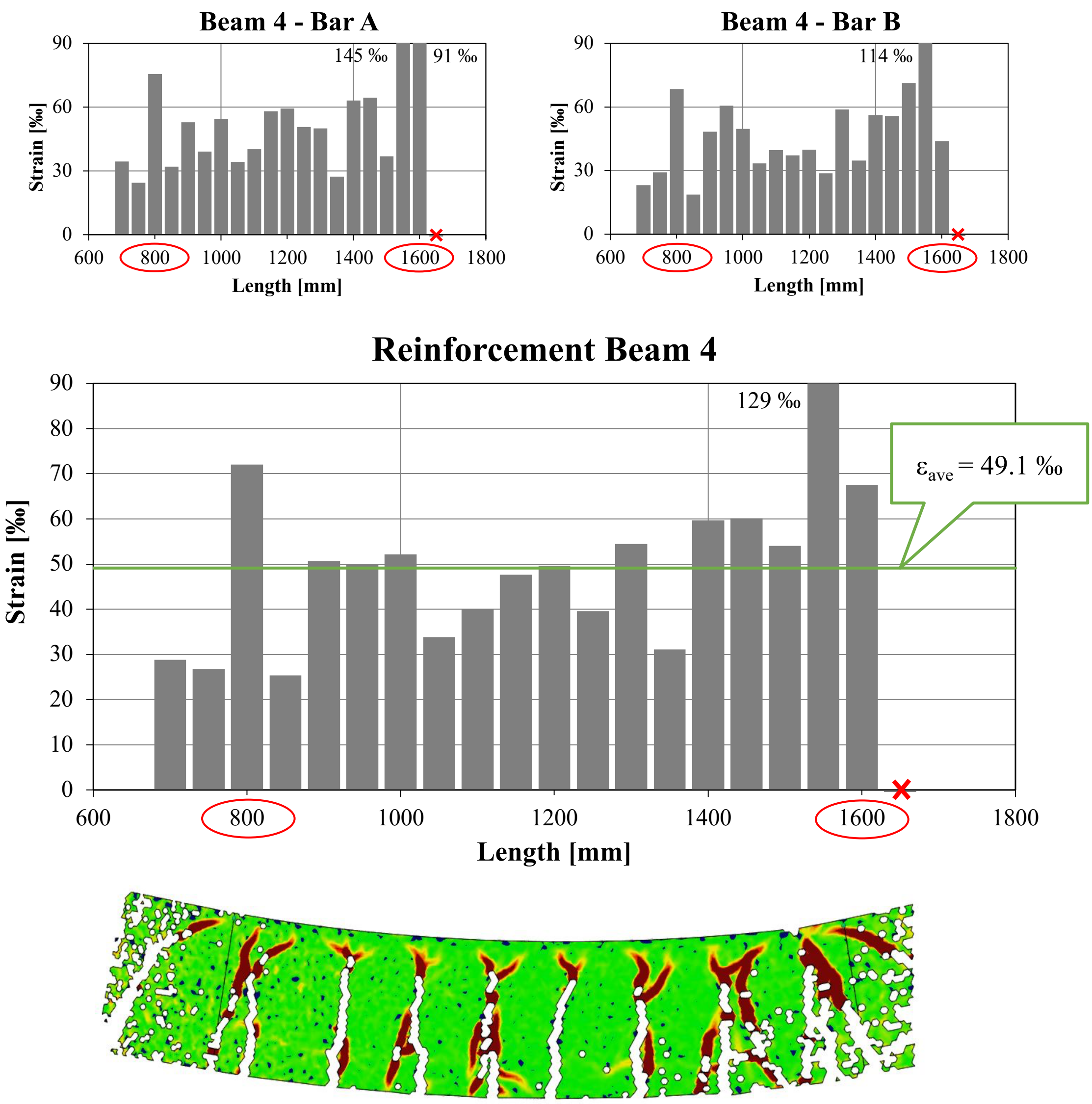

Figure D.16 *Plastic reinforcement strain measurements for each reinforcement bar (upper charts), the average strain of the two bars (middle chart) and the crack pattern figure from DIC for beam 4.*

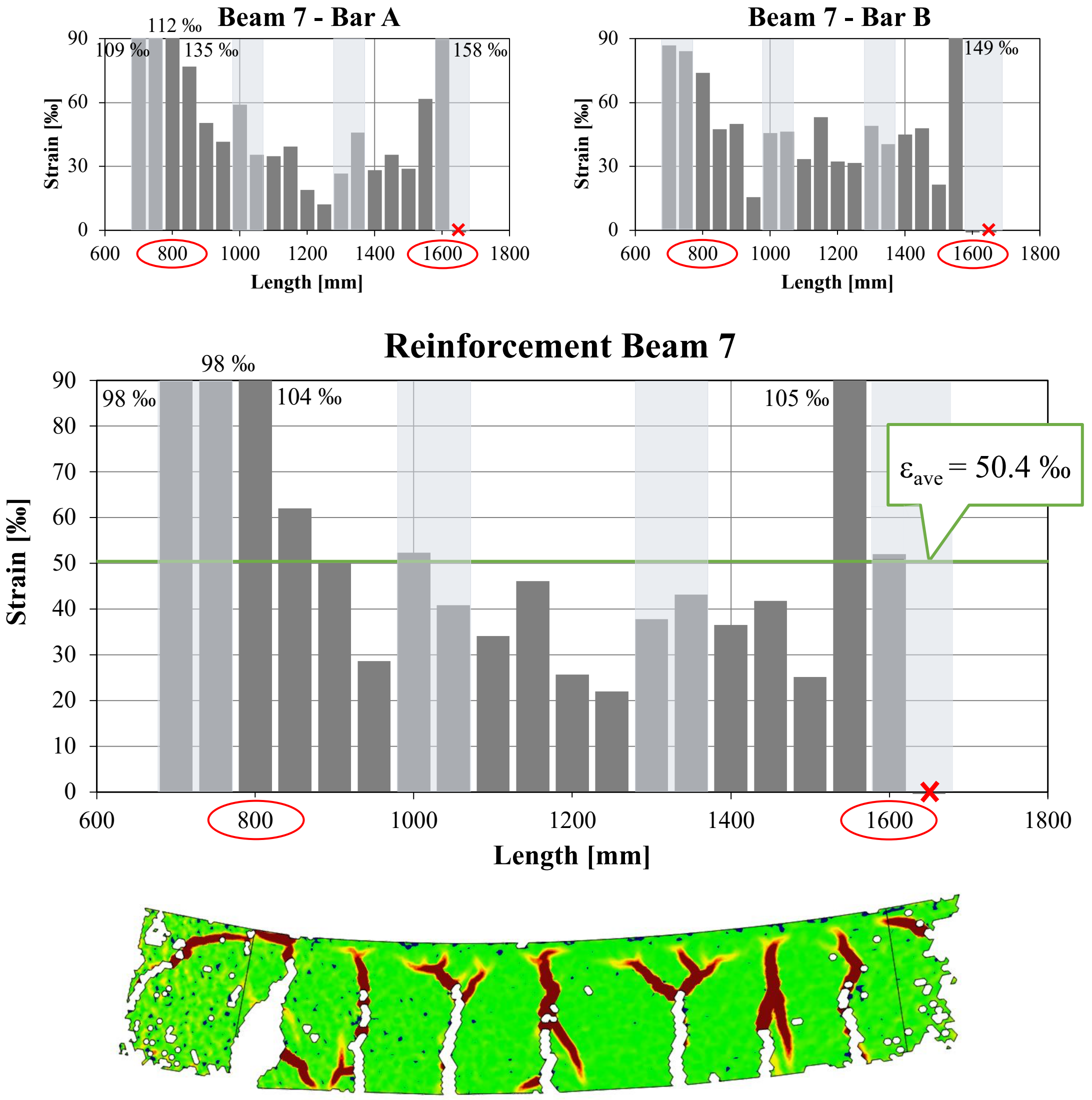

Figure D.17 *Plastic reinforcement strain measurements for each reinforcement bar (upper charts), the average strain of the two bars (middle chart) and the crack pattern figure from DIC for beam 7.*

D.3 Comparison of plastic strain results

A more detailed comparison of the plastic strain results are presented in Tables D.2-D.4. The results are presented without the 64 ‰ and 90 ‰-limit. See Section 7.4 for comparison of results as bar charts. For beam 1, due to difficulties in fitting the ruptured parts together between the coordinates 800 mm and 850 mm, the elongation and plastic strain value from the 3D scanning are greater.

Table D.2 Comparison of the plastic strain values from 3D scanning and measuring and the difference in measured elongation between the methods for beam 1.

Starting coordinate	3D scanning [‰]	Measurements [‰]	Difference [mm]
700	7	10	3
750	80	120	40
800	510	180	330
850	43	30	13
900	-	60	-
950	52	50	2
1000	0	0	0
1050	46	40	6
1100	5	10	5
1150	-	0	-
1200	8	20	12
1250	46	25	21
1300	32	15	17
1350	34	10	24
1400	42	30	12
1450	11	0	11
1500	17	30	13
1550	35	10	25
1600	-	10	-
1650	-	0	-

Table D.3 Comparison of the plastic strain values from 3D scanning and measuring and the difference in measured elongation between the methods for beam 4.

Starting coordinate	3D scanning [‰]	Measurements [‰]	Difference [mm]
700	29	20	9
750	27	10	17
800	72	60	12
850	25	30	5
900	51	40	11
950	50	50	0
1000	52	50	2
1050	34	30	4
1100	40	60	20
1150	48	50	2
1200	50	50	0
1250	40	40	0
1300	54	50	4
1350	31	50	19
1400	60	50	10
1450	60	50	10
1500	54	60	10
1550	90	90	0
1600	68	80	12
1650	-	10	-

Table D.4 Comparison of the plastic strain values from 3D scanning and measuring and the difference in measured elongation between the methods for beam 7.

Starting coordinate	3D scanning [‰]	Measurements [‰]	Difference [mm]
700	90	80	10
750	90	80	10
800	90	80	10
850	62	65	3
900	50	55	5
950	29	30	1
1000	52	40	12
1050	41	50	9
1100	34	40	6
1150	46	40	6
1200	26	35	9
1250	22	25	3
1300	38	20	18
1350	43	70	27
1400	37	55	18
1450	42	20	22
1500	25	40	15
1550	90	25	65
1600	52	20	32
1650	-	30	-

D.4 Cross-sectional area from 3D scanning

The cross section analysis was performed according to a provided MATLAB-file. The blue curve in Figure D.18 represent the cross section of the reinforcement before testing and the orange after testing. The part with the largest strain value was used in the analysis except from bar B in beam 1 and and bar B in beam 4 due loss of data. The reinforcement part of beam 1, bar A was ruptured which can be seen in the results as a drastic decrease of the cross-sectional area.

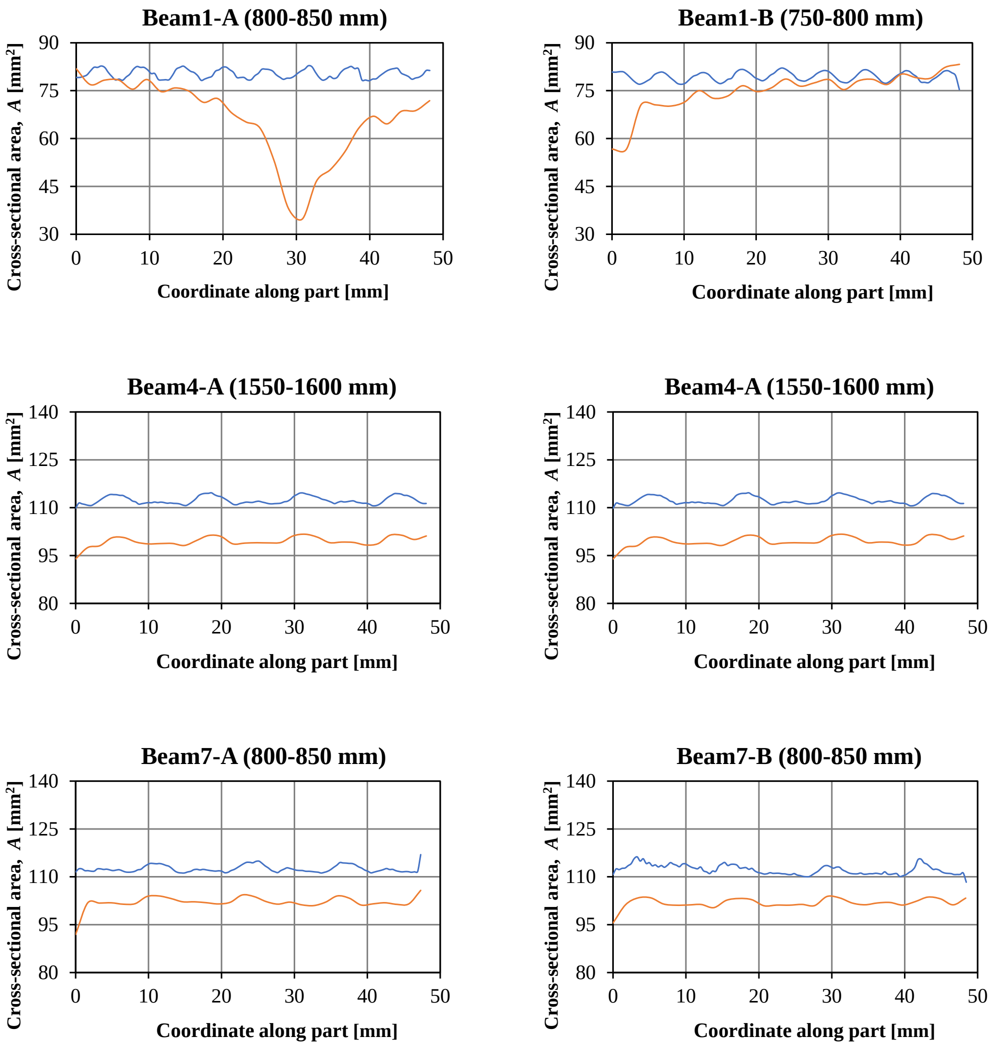

Figure D.18 *Cross-sectional area before and after testing of a part with largest strain value for each bar of beams 1, 4, and 7. The values before and after testing is shown by blue (top) and orange (bottom) line, respectively.*

DEPARTMENT OF ARCHITECTURE AND CIVIL ENGINEERING
CHALMERS UNIVERSITY OF TECHNOLOGY
Gothenburg, Sweden
www.chalmers.se

CHALMERS
UNIVERSITY OF TECHNOLOGY